Master's thesis

NTNU
Norwegian University of Science and Technology
Faculty of Social and Educational Sciences
Department of Geography

Ghazal Moghaddam

Life cycles of glacial lakes in Norway:

Insights from machine learning algorithms on Landsat series and Sentinel-2

Master's thesis in Natural Resource Management - Geography
Supervisor: Irina Rogozhina
Co-supervisor: Liss Marie Andreassen
May 2021

NTNU
Norwegian University of
Science and Technology

Ghazal Moghaddam

Life cycles of glacial lakes in Norway:

Insights from machine learning algorithms on Landsat series and Sentinel-2

Master's thesis in Natural Resource Management - Geography
Supervisor: Irina Rogozhina
Co-supervisor: Liss Marie Andreassen
May 2021

Norwegian University of Science and Technology
Faculty of Social and Educational Sciences
Department of Geography

NTNU
Norwegian University of
Science and Technology

Abstract

The observed retreat of mountain glaciers on a global scale promotes the formation and growth of glacial lakes across newly exposed ice-free areas. In mainland Norway, this process drives the rise in glacial lake outburst floods (GLOFs), posing a considerable threat to people and infrastructure downstream. Moreover, many glacial lakes are used as reservoirs for hydropower production and thus represent an important energy source, emphasizing the need for continuous monitoring of glacial lake life cycles.

Remote sensing is currently the most efficient technique for tracking changes in glacial lakes, understanding their responses to climate change and observing lakes prone to GLOFs. Recent advances in machine learning techniques have presented new opportunities to automatize glacial lake mapping over large areas. For the first time, this study presents a Norway-wide reconstruction of glacial lake changes through the last three decades using machine learning algorithms and long-term satellite observations. It contrasts the performance of two classification methods - maximum likelihood classification (MLC) and support vector machine (SVM) - to outline glacial lakes and study their evolution using the Landsat series and Sentinel-2 images.

This study zooms into the pros and cons of each classification method and satellite product through the prism of glacial lake processes occurring over disparate temporal and spatial scales - from lake formation, growth and dissociation from the proximal glaciers to the aftermath of rapid GLOF events. Based on this analysis, I conclude that the recognition skills of supervised classification methods largely depend on the quality of satellite images and careful selection of training samples. Some of the factors that adversely affect the classification results are unfavourable weather conditions such as cloud, snow and ice cover, image disturbances through atmospheric corrections and shadows on slopes that lead to misclassifications. Regardless of higher spatial and temporal resolution, Sentinel imagery has not revealed significant advantages over Landsat but has shown a potential for their complementary use to continue glacial lake observations in the future. The performance of SVM is clearly superior to MLC, but it is difficult to use over large spatial scales, at least in the form it is currently implemented in ENVI.

Sammendrag

Den observerte tilbaketrekningen av isbreer i global skala fremmer dannelsen og veksten av bresjøer i nylig isfrie områder. På Fastlands-Norge fører denne prosessen til økningen i Glacial Lake Outburst Floods (GLOFs), som utgjør en betydelig trussel mot mennesker og infrastruktur nedstrøms. Videre blir mange bresjøer brukt som reservoarer for vannkraftproduksjon og representerer dermed en viktig energikilde. Dette understreker behovet for kontinuerlig overvåking av livssyklusene til bresjøene.

Fjernmåling er for tiden den mest effektive teknikken for å spore endringer i bresjøer, forstå hvordan de påvirkes av klimaendringer og observere innsjøer som er utsatt for GLOF. Nylige fremskritt innen maskinlæringsteknikker har gitt nye muligheter for å automatisere kartlegging av bresjøer over store områder. Denne studien presenterer for første gang over hele Norge rekonstruksjon av endringer i bresjøer gjennom de siste tre tiårene ved hjelp av maskinlæringsalgoritmer og langsiktige satellittobservasjoner. Den sammenligner ytelsen til to klassifiseringsmetoder – maksimal sannsynlighetsklassifisering (MLC) og støttevektormaskin (SVM) - for å skissere bresjøer og studere deres utvikling ved hjelp av Landsat-serien og Sentinel-2-bilder.

Denne studien tydeliggjør fordelene og ulempene ved hver klassifiseringsmetode og satellittprodukt gjennom prismen til bresjøprosesser som foregår over forskjellige tidsmessige og romlige skalaer - fra dannelse av innsjø, vekst og dissosiasjon fra de proksimale breene til ettervirkningen av raske GLOF-hendelser. Basert på denne analysen konkluderer jeg med at deteksjonsferdighetene til overvåkede klassifiseringsmetoder i stor grad avhenger av kvaliteten på satellittbilder og nøye utvalg av treningsprøver. Noen av faktorene som påvirker klassifiseringsresultatene negativt og kan føre til feilklassifisering er ugunstige værforhold som sky, snø og isdekke, bildeforstyrrelser gjennom atmosfæriske korreksjoner og skygger i skråninger. Uavhengig av høyere romlig og tidsmessig oppløsning har Sentinel-bilder ikke avdekket betydelige fordeler i forhold til Landsat, men har vist et potensial for deres komplementære bruk i videre observasjoner av bresjøer i fremtiden. SVM har helt klart bedre

ytelse enn MLC, men SVM er vanskelig å bruke over store romlige skalaer, i det minste i den formen det for øyeblikket er implementert på i ENVI.

Acknowledgements

Through the past few years, I have started to appreciate the presence of some people in my life even more than before. People who I have loved and admired, people without whom I would not have made it this far. So, I take this opportunity to express a little of it.

Here, I would like to express my sincere gratitude to my astoundingly supportive supervisor at NTNU, Dr Irina Rogozhina, whose enthusiasm in science was my initial motivation to start working with her. Her continuous encouragement, valuable suggestions and priceless friendship composed a unique combination to persuade me when I needed it the most, and her constant guidance helped me throughout the research and writing of this thesis, and for that, I am forever thankful.

I also owe a deep sense of gratitude to Dr Liss Marie Andreassen, my supervisor at NVE, who has been the most reliable help in every stage of my research. Her prompt inspirations and technical suggestions with kindness have enabled me to complete my work in the best way I had hoped.

A very special thank you to Dr Miriam Jackson for all the time she invested in giving advice and suggestions at the beginning of my research. Although the topic changed, her valuable help in different aspects of the new topic was always great support.

I am thankful for having had the chance to experience an international circle of friends in Norway, for all the great memories with my classmates of Natural Resource Management 2018, and the lifetime friendships I have made.

I cannot begin to express my appreciation for my family, whose unconditional support, love and care, even from afar, have enriched my everyday life through the past few years with all the difficulties on the way. Without them, nothing would have been possible, and I would like to send my most special thanks to my sister, who is my relief, my most important mental support and role model.

Table of Contents

List of Figures

List of Tables

List of Abbreviations

ACI	Atmospherically Corrected Imagery
AWLHM	Adaptive Window Local Histogram Matching
DEM	Digital Elevation Model
DN	Digital Number
DOS	Dark Object Subtraction
EROS	Earth Resources Observation and Science
ESA	European Space Agency
FCC	Flase Colour Composite
FLAASH	Fast Line-of-sight Atmospheric Analysis of Hypercubes
GHM	Global Histogram Matching
GLIMS	Global Land Ice Measurements from Space
GLO	Glacial Lake Outline
GLOF	Glacial Lake Outburst Flood
IDH	International Hydrological Decade
ISAC	In-Scene Atmospheric Compensation
LLHM	Local Linear Histogram Matching
MLC	Maximum Likelihood Classification
MODTRAN	MODerate resolution atmospheric TRANsmission

NASA	National Aeronautics and Space Administration
NDVI	Normalized Difference Vegetation Index
NDWI	Normalized Difference Water Index
NIR	Near Infrared
Non-ACI	Original imagery without application of atmospheric correction
NVE	Norwegian Water Resources and Energy Directorate
OLI	Operational Land Imager
QUAC	QUick Atmospheric Correction
RBF	Radial Basis Function
RGB	Red-Green-Blue (colour composite)
ROI	Region Of Interest
SLC	Scan Line Corrector
SNAP	Sentinel Application Platform
SVM	Support Vector Machine
SWIR	Short Wave Infrared
TIRS	Thermal Infrared Sensor
TOA	Top Of Atmosphere
UNESCO	United Nations Educational, Scientific and Cultural Organization
USGS	United States Geological Survey

1 Background

Due to the globally rapid melting of glaciers, glacial lakes formation and extension is increasing in many regions (S. R. Bajracharya & Mool, 2017). Glacial lakes, as water bodies fed by modern glacier meltwater, play an important role in not only the Earth's hydrosphere but also cryosphere studies related to glaciers (Yao *et al.*, 2018). Their existence also affects human activities and lives in the downstream areas as they are significant water reservoirs for the drinking water supply, irrigation, and hydropower plants feed. On the other hand, glaciers and glacial lakes can pose a threat to the downstream communities and infrastructure through often unpredictable natural hazards, such as glacier surges, ice avalanches and Glacial Lake Outburst Floods (GLOFs) (Allen *et al.*, 2018; S. R. Bajracharya & Mool, 2017; Gagliardini *et al.*, 2011; Hans *et al.*, 1984).

The rapid deglaciation is expected to continue globally, bringing the topic into focus from the aspects mentioned above. Several studies are conducted on the effect of deglaciation on the number and extent of glacial lakes worldwide, and researchers declared a rising trend in the past few decades (Carrivick & Quincey, 2014; Carrivick & Tweed, 2016; Paul *et al.*, 2007). Consequently, glacial lakes present several issues and opportunities in different societies. Although current glacial lakes are too small to cause climate feedback globally, their presence in an area can cause local effect in conditions by making a more positive surface energy balance (Tweed & Carrivick, 2015). Amplifying ice loss from glacier terminus by mechanical calving and subaqueous melt is also confirmed as a regional impact of glacial lakes (Benn *et al.*, 2007; Truffer & Motyka, 2016).

As glaciers retreat, sediment from the valleys and slopes is transported by hydrological systems, and some of it may deposit in the glacial lakes downstream. This deposited sediment can be used as means to study climate and regional hydrologic changes as they are evidence of different periods of deglaciation and sediment fluxes (Denton *et al.*, 1999; Pu *et al.*, 2013; Tweed & Carrivick, 2015). However, by sudden drainage of glacial lakes due to dam failure, a tremendous amount of water can be carried downstream and shape various landforms by erosion,

transportation, and deposition of sediments (Cenderelli & Wohl, 2003). The erosional and depositional features that shape as a result of such floods create landforms that represent proglacial environments.

Mapping and monitoring glaciers and glacial lakes through in-situ work is time-consuming and can be challenging. That is why remote sensing has become a more valuable method for several decades since satellite imagery has been available. Each satellite has its characterization based on its spatial, spectral, and temporal resolution. The spatial resolution of the satellite imagery is defined as the pixel size that covers an area on the Earth's surface, while the temporal resolution is the revisiting frequency of every satellite on a specific location. The spectral resolution is the number of the spectral bands in which the sensor collects reflected radiance. The choice of satellite to use is dependent on the aim of the study and the resolution necessary. For instance, combining different sensors in satellites provides the opportunity for researchers to study and measure physical and biogeochemical parameters to have an overview of the Earth's system (Loyola & Coldewey-Egbers, 2012). Several sensors onboard satellites bring about the opportunity to check the surface with spectral that the human eye cannot detect. These narrow spectral bands include near infrared and mid infrared wavelengths. The Earth Resources Technology Satellite, Landsat 1 was launched in 1972 with medium spectral (7 bands), low temporal (18 days) and low spatial (80 m) resolution (USGS). Other Landsat missions have continued with improvements of resolutions ever since, and Landsat 8 that carries the Operational Land Imager (OLI) and the Thermal Infrared Sensor (TIRS) instruments is the most recent of the Landsat mission series launched in 2013, which makes Landsat imagery unique in terms of the period they keep a record of surface observations from space.

Landsat-1 was the first Earth-observing satellite that launched in 1972. Landsat images cover the longest time, and since 2008 the missions provide researchers with free of charge imagery. The launch of Sentinel-2 in 2015 by the European Commission's Copernicus program presented the better spatial and temporal resolution and significantly advanced users' capabilities for diverse usage. Sentinel 2A-B has similar spectral bands to Landsat 8, which is the latest of the Landsat series. While Sentinel has a better spatial resolution (visible and near-infrared bands have a spatial resolution of 10 meters, two shortwave infrared bands 20 meters), it misses the thermal

band from Landsat. USGS scientists from both projects worked on cross-calibration of Landsat 8 and Sentinel-2A sensors to enable scientists and researchers to use data from both collectively.

Systematic use of remote sensing to assess glacier and glacial lake changes in the local extent is an essential step in linking these datasets. One of the most controversial concepts in glacier studies is the definition of glacial lakes. Some researchers emphasize the history of the formation of lakes and take lakes formed by glaciation and supplied by meltwater from modern glaciers as glacial lakes (S. Bajracharya *et al.*, 2020; Cao *et al.*, 2016; Yao *et al.*, 2018). Not having the source of water and the precise time the lakes formed are why glacial lakes are hard to distinguish from other natural lakes and why these studies are hardly comparable. One of the most common criteria for glacial lake recognition is the relation of the lake with the glacier, as Emmer *et al.*, 2015 explain in their paper.

Meanwhile, some other studies consider the distance to the glacier as a defining factor for separating glacial lakes from other natural lakes. For instance, some meters or, in some cases, a few kilometres like X. Wang *et al.*, 2013 and G. Zhang *et al.*, 2015. What makes these studies debatable is whether the main water source of these lakes is from glacier meltwater or not.

Several different remote sensing methods are used to delineate glacial lakes. Classification-based methods (Aggarwal *et al.*, 2016; Barbieux *et al.*, 2018) and using different indexes (S. Bajracharya *et al.*, 2020; Huggel *et al.*, 2002; Jha *et al.*, 2017; McFeeters, 1996), manual mapping (G. Zhang *et al.*, 2019) or combined methods are common. Limitations of every method drive scientists to explore different methods or take advantage of complementary methods (M.-m. Zhang *et al.*, 2018). Variability of glacial lakes and their physical change through years not only is another factor that increases the difficulty of their identification but also requires frequent assessment (S. Bajracharya *et al.*, 2020; Li & Sheng, 2012). Therefore, it is necessary to have a reliable scheme to enable convenient (concerning time and financial aspects) assessment of glacial lake changes over time.

Glaciers in Norway are important and follow the global recession trend after the Little Ice Age (LIA) since about 1750 (Liss M. Andreassen *et al.*, 2014; Viani *et al.*, 2020). As well as other countries with a large number of glaciers, in Norway, runoff for hydropower production and

hazard management are the initial reasons to investigate changes in glaciated areas. Many hydro powerplants have been constructed or were considered for construction near the glaciers or close to the glacial lakes (Liss M. Andreassen *et al.*, 2014; Jackson & Ragulina, 2014).

Glacier Lake Outburst Floods (GLOFs) or jøkulhlaup (the Icelandic term) is defined as a sudden burst of meltwater from a glacier leading to small or megafloods impacting the landscape. They may originate from marginal or subglacial sources of meltwater that are discharged due to failure of glacial lake dams, including glacier ice or moraine dams (H. Bjornsson, 2003; H Bjornsson, 2009; Björnsson, 1974). Liestøl, 1956 described historical glacier dammed lakes in Norway with GLOF events and discussed the explanations that existed at the time. Engeset *et al.*, 2005 focused on the GLOFs from Blåmannsisen in northern Norway and studied the possibility of future discharges. Although studies of GLOFs as explained by Jackson and Ragulina, 2014 are mostly focused on their hazardous aspect, Jackson, 2018 states that considering GLOF mitigation strategies as complementary to hydropower schemes can be beneficial. For instance, in a 2015 event in Harbardsbreen in southern Norway, the hydropower reservoir was drained before the jøkulhlaup event and even though the volume of the flood was larger than the volume of the reservoir, the reservoir or downstream areas were not confronted with any risk.

1.1 Glacial lake inventories in Norway

During recent decades, glaciers in Norway have received substantial attention for risk assessment due to jøkulhlaups and the availability of water resources for hydropower developments. Several glacier lake outline datasets have been made available by the Norwegian Water Resources and Energy Directorate (NVE) for download and viewing for the public through https://www.nve.no/. The first complete inventory used semi-automatic mapping method by NDWI from Landsat 5 and Landsat 7 imagery in 1999-2006. In NVE's report on the glacial lakes published in 2013 and 2014, glacial lakes are defined "as water bodies that either intersected, were within a distance of <50m or were completely within the glacier boundary/glacier area outline"(Liss M. Andreassen *et al.*, 2014; Liss M Andreassen & Winsvold, 2013). After omitting lakes smaller than 0.001 km^2, 398 lakes were outlined in total.

The next outline was done using manual digitization of Landsat 5 within the period of 1988-1997 by using the other inventory as a basis. The inventory includes 217 glacial lakes and remains incomplete due to cloud coverage in some regions (Liss M Andreassen & Winsvold, 2013).

A new inventory of glacial lakes, GLO2014, as part of the Copernicus Glacier Service project, is based on manual digitization of Landsat-8 imagery from 2014 (L. Andreassen *et al.*, 2021). This is the first inventory not matching the glacier outlines, so glacier lakes were mapped using glacier outlines 1999-2006 as the basis, mapping lakes in the images that were within <50m of the glacier outlines 1999-2006. In total, 636 lakes were mapped, but due to glacier retreat between 2006 and 2014, some of the lakes may be farther away from the glacier lake outlines of 2014 (Liss M. Andreassen *et al.*, 2012; T. Nagy & L. Andreassen, 2019).

In the inventory of 2018, Sentinel-2 imagery was used to apply semi-automated method by using NDWI and manual digitization of lakes in whole Norway. Lakes larger than 0.001 km^2 in a buffer of <100m were chosen so that recently decoupled lakes from glaciers can also be included in the inventory. Only glaciers larger than 0.25 km^2 were considered. Thus, some of the lakes of smaller glaciers were not mapped. The 414 lakes are divided into different categories based on their connection to the glacier or nature of damming (T. Nagy & L. Andreassen, 2019).

The most recent inventory of glacial lake outlines, GLO2018-2019, mapped glacial lakes from Sentinel-2 images and new glacier outlines of 2018-2019. Glaciers of 0.05 km^2 size were set to include more glacial lakes in this inventory. The mapping method varied from manually digitizing a split line at the glacier outline and automatically mapping to partially manually digitizing the lakes (L. Andreassen *et al.*, 2021). The final product was not prepared at the time of production of maps in this study. Therefore, they were not included in the comparisons.

1.2 Glacier inventories in Norway

By the beginning of the International Hydrological Decade (IHD) in the 1960s, following a resolution by United Nations Educational, Scientific and Cultural Organization (UNESCO), in order to consolidate hydrologic information, national committees were coordinated at an international level to acquire correct basic data, concepts and terminology. As a result,

glaciological studies underwent significant changes as well, and glaciers were divided based on hydrological systems in their surrounding areas. Glacier units were introduced as subdivided glaciers that drain into different rivers (UNESCO, 1971).

Glaciers in mainland Norway cover a much larger area compared to other countries on the European mainland (Beniston *et al.*, 2018). According to the latest reports of the water resource and energy directorate of Norway (NVE), the total area of glaciers is 2692 km^2, from which 1523 and 1169 km^2 are located in southern and northern Norway, respectively (Andreassen et al, 2012). The distribution of Norwegian glaciers and their regional concentration is presented in figure 1.1.

Atlas of glaciers in South Norway by Østrem and Ziegler in 1969 and glacier atlas of Northern Scandinavia by Østrem et al. (1973) are the first glacier inventories of Norway which were manually marked (Østrem *et al.*, 1973; Østrem & Ziegler, 1969). An updated Atlas of Glaciers in south Norway was published in 1988 (Østrem et al. 1988)

NVE assembled a glacier inventory for mainland Norway using Landsat imagery from the period of 1999-2006. Until inventory of 2018-2019, this was the most recent complete inventory of glaciers that also contributed to the Global Land Ice Measurements from Space (GLIMS) initiative. Glacier outlines were mapped by a semi-automatic band ratio method which was followed by manual correction of glacier polygons. 2534 glaciers were delineated in total, of which 1252 glaciers were located in the south, and 1282 were in northern Norway. Compared to the older inventories from 1988 and 1973, the number of glaciers in this inventory showed significant growth of 57%. The reason might be due to the inclusion of smaller entities that were omitted from the older inventories or the change in the method used from manual to semi-automatic (Liss M. Andreassen *et al.*, 2012; Winsvold *et al.*, 2014).

The most updated glacier inventory for mainland Norway and Svalbard was based on Sentinel-2 images from 2018-2019. Band ratio thresholding was used to produce the initial glacier outlines, and they were then checked and edited manually based on high-resolution orthophotos (L. Andreassen *et al.*, 2021). The glacier outlines from southern Norway were used for the production of glacial lake outlines in this study.

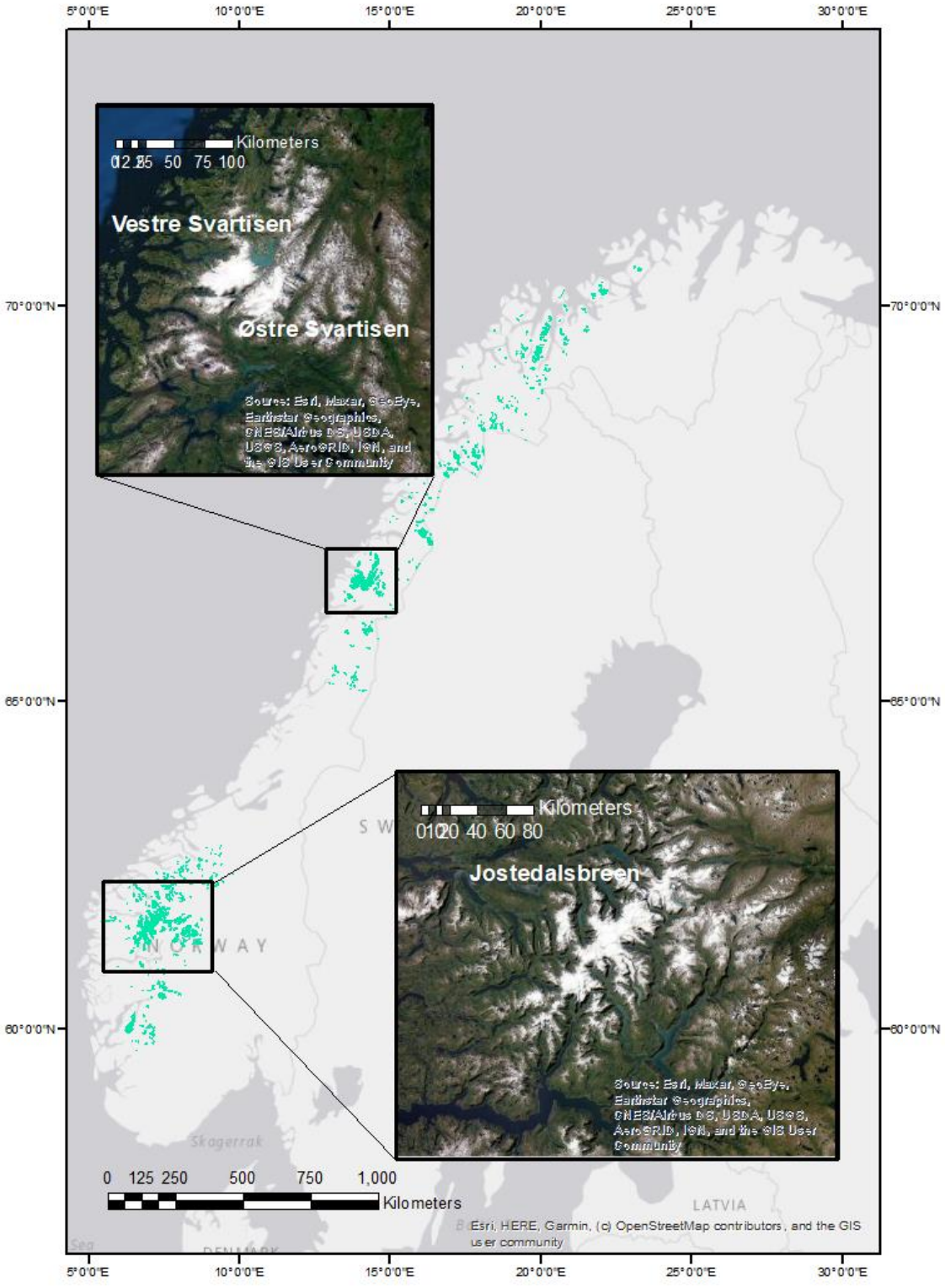

Figure 1.1 Areas covered by glaciers in Norway. The boxes indicate regions with glacier concentration.

1.3 Objective and research questions

With the continuous rise of the Earth's mean temperature, melting of glaciers and icecaps accelerates, new glacial lakes form, and some vanish or disconnect from the glacier. On the other hand, due to diverse classification, categorization methods and definitions, some glacial lakes fall out of a category. As a result, studies of glacial lake outlines are incomparable; hence following their formation, decline, and in general, their life cycle consecutively is strongly affected. In Norway, several glacier and glacial lake inventories exist and have been produced using different methods and data sources based on available data and methodology at the time.

The main objective of this study is to assess the potential use of machine learning algorithms with Landsat and Sentinel imagery for the recognition of glacial lakes and tracing their life cycle in Norway following a consistent method. One of the advantages is that testing different methods could improve the outlining and help hazard management and climate adaptation plans for future applications.

Some other research questions that I try to answer through this study are as follows:

- How accurately can machine learning algorithms recognize water bodies from other surface types in the context of alpine environments?
- Is it possible to complement previous glacial lake inventories and recognize glacial lakes in the first stages of their formation through the use of machine learning methods?
- Is it possible to continue studying glacial lake life cycle by substituting Landsat with Sentinel images?
- Is Support Vector Machine (SVM) as another machine learning algorithm capable of identifying glacial lakes in comparison with Maximum Likelihood Classification (MLC)?
- What are the challenges of application of such methods for recognition of water bodies in proglacial environments?

2 Methods

In order to outline glacial lakes and detect their changes in this study, supervised classifications from machine learning methods were used on multi temporal satellite images. As the oldest Earth observing satellite, Landsat series have continuous images from 1972 to the present. On the other hand, Sentinel-2 imagery with higher spatial and temporal resolution than Landsat has gained significant attention from researchers in various disciplines since the launch of the satellite in 2015.

Before applying maximum likelihood classification (MLC) and Support Vector Machine (SVM) as two of the most common machine learning algorithms in this study, the images needed to go through pre-processing steps, some of these steps were specific to particular sets of images, and some were general procedures prior to application of methods. In this chapter, I introduce the datasets and machine learning methods used in this study and describe the pre-processing steps necessary for preparing the images for use in the application of methods.

2.1 Datasets

2.1.1 Landsat imagery

This study uses different sets of imagery from the Landsat series in different years, including imagery from Landsat-8 OLI, Landsat-7 ETM and Landsat 4-5 TM. Improved signal-to-noise radiometric performance in Landsat-8 OLI, launched in 2013, enables a better characterization of land cover conditions (USGS, 2013), which provides researchers using Landsat 8 with significantly more detailed data.

The multi-temporal Landsat imagery was obtained as Level-1 products from the U.S. geological survey portal (https://earthexplorer.usgs.gov/). Landsat collection 1 has the highest quality of Landsat level 1 products and is one of the best choices for time series analyses considering its

continuous data retrieval since the 1970s. For the analyses presented in this study, imageries with less than 15% cloud cover from the summer and early autumn were selected when the lakes are covered with no or little ice.

To investigate the glacial lake changes through time, three subsets of imagery were used. The information about all the scenes that were used in this study is given in table 2.1. Cloud and snow coverage are determining factors when selecting satellite imagery scenes to use in remote sensing. Even by implementing cloud masks to remove clouds from the imagery, usage of satellite image can be limited once the study objects are covered by it. Therefore, using satellite imagery with no or little cloud cover is more common.

Glacial lakes, by definition, are lakes intersected with or located in the vicinity of a glacier (see section 2.2). Snow coverage is a limiting factor for recognition of glacial lakes that are adjacent to glacier ice in remote sensing. Due to limitations of satellite imagery, such as mentioned above in some areas, selection of satellite imagery needs to be done thoroughly. So, in this study, I assessed the images for each year through Landsatlook viewer, which is an online tool to pre-qualify the USGS archives rapidly and control the image properties based on the viewers' perspective. In the years of interest in this study, it was not possible to achieve the least cloud and snow coverage in all scenes in one year. Hence it was necessary to extend the analysis to the data from the adjacent years.

Seasonal snow coverage can make conditions adverse for mapping, which may lead to overestimation of glacier extents or/and overestimation of glacial lake extents. This issue is particularly more problematic in some scenes from northern Norway used for 1999-2006, as mentioned by Liss M Andreassen *et al.*, 2012. For the same reasons, the existing glacier and glacial lake inventories in Norway belong to different time spans, which were followed by this study to keep the consistency in order to enable the possibility of further comparisons. The maximum time span used for collecting all the scenes relevant to the study is nine years for the inventory of 1988-1997. The imageries were selected from the time span of June, July, and September 2018 and 2019, July, August, and September 1999, 2001, 2002, 2003, 2006, and 1988-1997.

Table 2.1 Landsat images used for detection of glacial lakes in this study.

Image set	Acquisition date	Satellite/Sensor	Landsat WRS Path/Row Sentinel tile number
1988-1997	1988.08.06	Landsat 5 (TM)	200/018
	1997.08.15	Landsat 5 (TM)	200/017
	1997.08.15	Landsat 5 (TM)	200/016
	1988.08.31	Landsat 5 (TM)	199/015
	1988.08.31	Landsat 5 (TM)	199/014
	1988.08.31	Landsat 5 (TM)	199/013
	1988.08.31	Landsat 5 (TM)	199/012
	1994.09.03	Landsat 5 (TM)	197/012
	1991.08.03	Landsat 5 (TM)	196/012
	1991.08.26	Landsat 5 (TM)	197/011
	1990.09.08	Landsat 5 (TM)	197/010
1999-2006	1999.09.07	Landsat 7 (ETM+)	199/014
	1999.09.07	Landsat 7 (ETM+)	199/013
	2001.08.20	Landsat 7 (ETM+)	198/012
	2001.08.20	Landsat 7 (ETM+)	198/011
	2004.08.05	Landsat 7 (ETM+)	197/011
	2004.07.22	Landsat 7 (ETM+)	195/011
	2004.07.31	Landsat 7 (ETM+)	194/011
	1999.09.07	Landsat 7 (ETM+)	199/015
	2004.08.10	Landsat 7 (ETM+)	200/018
	2006.07.22	Landsat 7 (ETM+)	201/016
	2004.08.10	Landsat 7 (ETM+)	200/016
	2004.08.10	Landsat 7 (ETM+)	200/017
	2004.08.08	Landsat 7 (ETM+)	202/017
2018-2019	2018.06.29	Landsat 8 (OLI)	201/017
	2018.06.06	Landsat 8 (OLI)	200/017

	2018.06.29	Landsat 8 (OLI)	201/018
	2018.07.01	Landsat 8 (OLI)	199/016
	2019.09.22	Landsat 8 (OLI)	199/017
	2019.09.22	Landsat 8 (OLI)	199/018
	2018.07.03	Sentinel-2	T32VLM
	2018.09.03	Sentinel-2	T32VLM
	2018.07.26	Sentinel-2	T32VLM
	2018.07.26	Sentinel-2	T32VLN
	2018.07.03	Sentinel-2	T32VMN
	2018.07.26	Sentinel-2	T32VMN
	2018.07.26	Sentinel-2	T32VLP
	2018.07.03	Sentinel-2	T32VMP
	2018.07.26	Sentinel-2	T32VMP
	2018.07.10	Sentinel-2	T32VMQ
	2018.07.26	Sentinel-2	T32VMQ
	2018.07.05	Sentinel-2	T32VNQ
	2019.08.27	Sentinel-2	T32VMN
	2019.09.26	Sentinel-2	T32VLQ

2.1.2 Sentinel-2 Imagery

Sentinel-2 mission is an ongoing mission that started through the collaboration of the European Space Agency (ESA), the European commission, industry, and service providers in 2015. The multispectral instrument onboard of Sentinel-2 satellite is designed to record 13 spectral bands of which four have a 10m spatial resolution while six have 20m and three 60m spatial resolutions. The remote sensing data is mainly aimed at the European Commission's Copernicus program to achieve a global Earth observation, including monitoring of vegetation, soil and water cover (ESA, 2015; Q. Wang *et al.*, 2016) and is freely accessible for researchers through ESA and USGS and in Norway through satellittdata.no. Sentinel-2 satellite has a 5-day revisit time that in addition to the higher spatial resolution compared to Landsat missions, can be used to monitor

land cover changes, map disasters, and provide pollution information, etc. in all disciplines. Images from Sentinel-2 satellite have been in use for several glaciological studies, from deriving glacier outlines and calculating glacier area to glacier surface velocity mapping (T. Nagy & L. M. Andreassen, 2019; Paul *et al.*, 2020; Paul *et al.*, 2016) to glacial lake mapping.

The aim of using Sentinel-2 images in this study is to evaluate the possibility of applying supervised classification methods on Sentinel-2 images as a complement to the previous Landsat images. This process allows more complete time-series analyses. Accordingly, Level-1C images from 2018 and 2019 have been downloaded from the USGS website. Level-1C image processing includes top-of-atmosphere (TOA) reflectance, radiometric and geometric corrections as well as orthorectification. The pre-requisite for selection of images has been to limit the cloud coverage to 15% for summer and early Autumn months selecting images with little snow. Table 2.1 includes information of Sentinel-2 images used in this study.

2.1.3 Digital Elevation Model (DEM) and slope maps

Digital Elevation Models (DEMs) are 3D visualizations of the terrain by representation of elevation data with each pixel value in a DEM corresponding to elevation data. Therefore, DEMs are essential for applications that involve surface characteristics such as slope (Florinsky, 2011; Mallet & David, 2016). Currently, the most common technique for production of DEMs is remote sensing by using data from airborne or satellite platforms, while they can also be generated based on conventional topographic surveys and digitizing topographic contours (Smith & Clark, 2005).

The 50 and 10-meter DEMs for entire Norway by the Norwegian mapping authorities were downloaded from Geonorge.no, where they are freely accessible. In this study, DEMs have been used to generate slope maps and calculate the average elevation of every satellite scene. The average elevation data is an essential input in the process of atmospheric correction of satellite imagery (for more information, see section 2.4.2).

On the other hand, in the northern hemisphere, north-facing slopes in the proximity of mountains are prone to be shaded. Due to their similar spectral characteristics, glacial lakes can be confused with mountain or cloud shadows. DEMs are commonly used to remove the shading effect of mountains in studies dealing with glacial lake outlining and hazards (Huggel *et al.*, 2002; Li & Sheng, 2012).

2.2 Glacial lake definition

Definitions of glacier lakes vary in previous studies. Considering different criteria for selecting glacial lakes discussed in previous studies here a glacial lake is defined as a water body that either intersects or is within a distance of less than 100 meters of the nearest concurrent glacier margin outline. Due to the limits of the methods in practice, other types of glacial lakes such as supraglacial, englacial and subglacial lakes have not been included in the definition and therefore neglected in this study. Considering glacier retreat in the past few decades, the glacier outlines related to the time periods of this study were used to outline glacial lakes.

2.3 Glacier outlines

Several digital glacier outline datasets exist for glaciers in mainland Norway and are freely available for download on the NVE website (https://www.nve.no/hydrology/glaciers/glacier-data/). Based on the available glacier inventories (see section 1.2), glacier area outlines used in this study belong to 1988-1997, 1999-2006 and 2018-2019, although the outlines from 1988-1997 and 2018-2019 were not complete (at the time of map production in this study for 2018-2019) they enabled us to have comparable datasets for different periods.

2.4 Image pre-processing

The operations satellite that the images go through before their application for land cover classification is called pre-processing. The goal of pre-processing is achieving an improved image in terms of correction for sensor and platform radiometric and geometric distortions of data for classification purposes. Mosaicking multiple images from a sensor to maintain uniform

conditions in every scene in use, correcting the irregularities or errors in the sensor, including striping and dropped lines, are other pre-processing steps to be taken for different use of the images. The pre-processing steps in this study are as follows in this section.

2.4.1 Gaps in Landsat 7 imagery

Since June 2003, the Scan Line Corrector (SLC) sensor onboard Landsat 7 failed to perform permanently. The application of the electromechanical sensor was to compensate for the forward motion of the satellite while scanning. One the recovery efforts were not successful, the sensor failure was announced permanent, and as a result, there are data gaps in the delivered data from Landsat 7 until the end of its operation (Boloorani *et al.*, 2008; Landsat 7; Pringle *et al.*, 2009).

The satellite ground track follows a zigzag trace line after SLC failure. This causes duplication of the image area, and the unscanned areas show as diagonal striations, which are narrow near the centre of the image and increase in width (about 10 pixels wide) at the edges of the scene (Asmaa Sadiq *et al.*, 2014; Pringle *et al.*, 2009). Landsat 7, level-1 data removes the duplicated areas and leaves the gaps (Landsat 7) (figure 2.1). In spite of the failure of SLC, since the radiometric and geometric quality of images in Landsat 7 remained unaffected, the satellite scanning continued, and Landsat was successful in keeping the long term, spatially consistent record of landscape change globally (Landsat 7; Yin *et al.*, 2017).

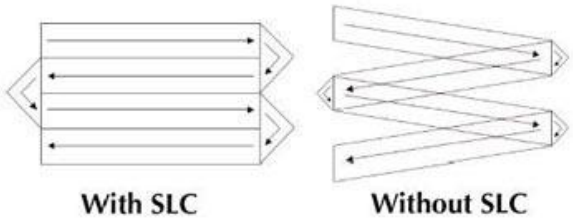

Figure 2.1 Illustration of the Landsat 7 Scan Line Corrector (SLC) failure from USGS website (L. USGS; USGS.gov).

After the failure of SLC, the Landsat team in USGS and National Aeronautics and Space Administration (NASA) suggested different methods to fill the gaps. The first suggestion was to estimate the reflectance of the unscanned areas by compositing the SLC-off image with a

corresponding band of laterally overlapping Landsat 7 images acquired on other dates for the same area (Andrefouet *et al.*, 2003). In the first phase provided by USGS/NASA Landsat team to recover the gaps in imagery, a simple radiometric adjustment technique was used. Global Histogram Matching (GHM) and Local Linear Histogram Matching (LLHM) algorithms were performed in this phase. This method estimates the linear transformation of the Digital Number (DN) values of the SLC-on image between the SLC-off image (image with gaps) and the SLC-on image (filled scene) by calculating the corrective gain and bias adjustment from all the pixels in the SLC-on image. The corrective gain and bias adjustment were calculated in order to estimate the pixel values in SLC-off images.

In the second phase, as an improvement, Adaptive Window Local Histogram Matching (AWLHM) algorithm was used instead of the LLHM algorithm in phase one. The improvement of this algorithm was that until there were unscanned pixels, the recovering algorithm repeated as many times it was necessary by taking the last recover image as an SLC-off image and other filling images (Asmaa Sadiq *et al.*, 2014; Chen *et al.*, 2012).

The overall anomaly in these products does not seem to significantly affect analyses of the processes over larger spatial scales such as land use and land cover changes. In contrast, possible impacts of the anomaly on more detailed analyses of small-scale processes should be thoroughly considered (Yin *et al.*, 2017).

The imagery for Landsat 7 Level-1 for 2003 onward is provided together with a gap mask folder to guide the gap-filling process. In this study, the gap-filling extension of ENVI 5.8 was used to perform this step of processing. The post-analysis showed that final results have not suffered from any significant defects in the classification due to anomalies in the imagery.

Individual bands need to be gap-filled before making any further progress, such as making RGB images and processing. Figure 2.2 presents a scene before and after gap-filling through ENVI5.8.

a) b)

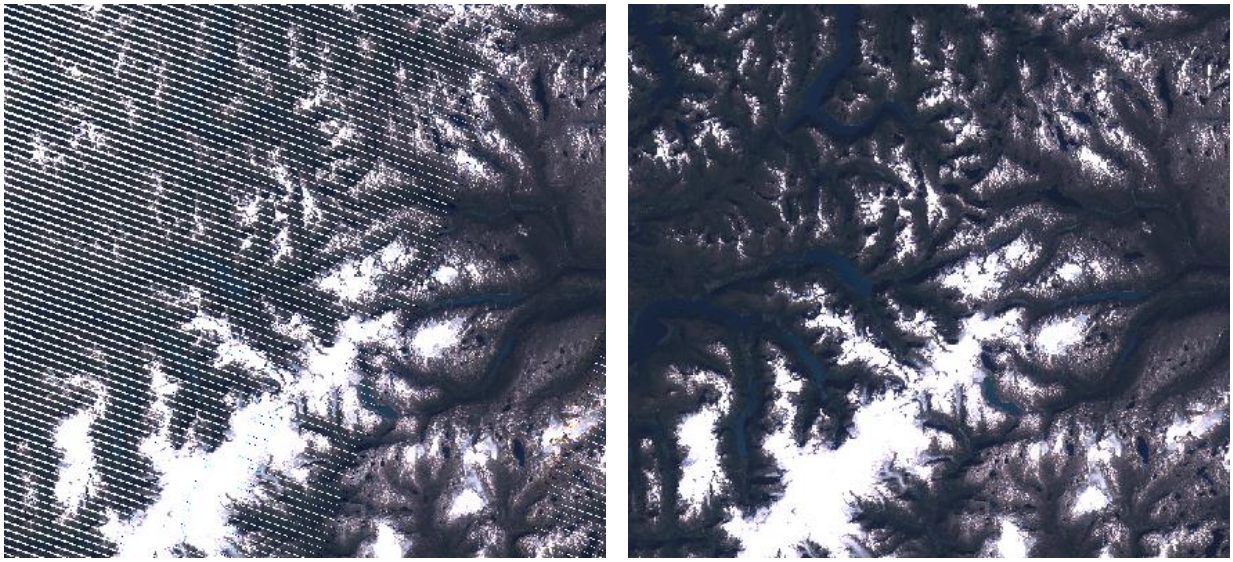

Figure 2.2 Part of Landsat 7 image from 2004.08.10 in the tile covering Jostedalsbreen in southern Norway a) before and b) after application of gap-filling.

2.4.2 Atmospheric correction

The images acquired from satellites are affected by atmospheric conditions, solar illumination, solar angle, and the different sensors the satellites use for reception. The true ground-leaving radiance at one point in a remotely sensed image is the reflectance of the target minus the brightness of the atmosphere itself, which is because of atmospheric particles that can absorb or scatter radiation from the Earth surface. In simple words, remotely sensed images include information about the atmosphere and the Earth's surface. Atmospheric correction aims to remove the atmospheric effects and restore the surface reflectance in remotely sensed imagery. To correct the atmospheric effects, properties such as the amount of water vapour and distribution of aerosols should be known, but since these measurements are rarely available, there are indirect techniques to retrieve and use them from their effect on the radiance data (Chavez, 1996; USGS.gov).

To better understand the concept of atmospheric correction in satellite imagery pre-processing and its normalization, it is necessary to be familiar with some definitions as follows (figure 2.3).

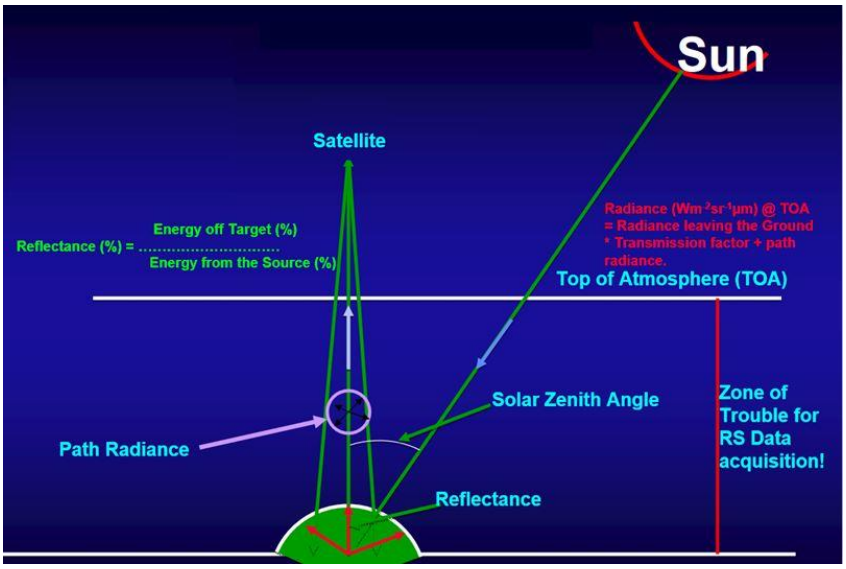

Figure 2.3 Illustration of radiance, reflectance, TOA (USGS.gov).

- **Digital Number (DN)**

Every pixel in satellite imagery has a numerical value called digital number or DN, which is representative of the energy a sensor receives from the ground (Rasmussen, 1987). DN is affected by the sensor, sun elevation, atmosphere, topography and surface cover.

- **Radiance**

Radiance is defined as the total amount of energy received by the sensor from the object being observed, and it is directly measured by the remote sensing instrument (Chavez, 1996; Rasmussen, 1987; Ray, 1994). Due to absorption or scattering, the atmosphere affects radiance. The atmosphere scatters some light (energy) that will be observed at the sensor while its particles also absorb some, which will decrease the observed radiance at the sensor.

- **Reflectance**

Reflectance is the ratio of the amount of energy reflected from a target to the amount of energy it receives. Reflectance is a property of the observed material and is achieved once atmospheric

effects, solar illumination and other disrupting factors are eliminated (Chavez, 1996; Rasmussen, 1987; Ray, 1994).

- **Top Of Atmosphere radiance (TOA)**

The radiance observable just outside the Earth's atmosphere is known as the TOA, which is calculated after DNs are converted to radiance.

- **Top Of Atmosphere reflectance**

Top of Atmosphere reflectance is also defined as the reflectance just outside the Earth's atmosphere and is calculated as the proportion of the amount of radiation received by an object to the amount reflected from it, so it is a ratio value.

- **Surface reflection**

Surface reflection is the final product needed in atmospheric correction. It is the reflectance above the Earth's surface or, for example, the vegetation in vegetation studies. For that, information on atmospheric conditions in the date and time of image acquisition is needed, which comes in the metadata of downloaded satellite images.

- **Metadata**

Metadata is the data that describes the satellite imagery. It comes in the form of text when the satellite image is downloaded and includes all the information of the scene downloaded, e.g. date and time of acquisition, sun elevation, sun angle, Earth-sun distance. Metadata is referred to for finding information on the satellite image; for instance, to apply atmospheric corrections.

In this study, since consistent results were required in all the utilized Landsat scenes, it was decided to download level-1 images and apply corrections. In addition to that, users are cautioned against processing data over high latitudes (>65°) to surface reflectance by USGS

Earth Resources Observation and Science (EROS) centre (Masek *et al.*, 2006; USGS.gov; Vermote *et al.*, 2016). Considering that northern parts of Norway are located in areas with latitude higher than 65°, it was preferred to apply the correction methods and monitor the changes.

There are different methods and models in applying atmospheric corrections on satellite images. One of the most commonly used models is Fast Line-of-sight Atmospheric Analysis of Hypercubes (FLAASH), as several researchers have made atmospheric correction studies based on comparing different methods. For instance, M.W. Matthew et al. (2002) and S. M. Adler-Golden et al. (1998) applied FLAASH atmospheric correction and confirmed that it was capable of achieving favourable results in generating accurate surface reflectance (S. Adler-Golden *et al.*, 1998; Matthew *et al.*, 2002). Meanwhile, Y. Guo and F. Zeng (2012) made a comparison of remote sensing imagery by using FLAASH and QUick Atmospheric Correction (QUAC) models. Their results showed that although both models were capable of eliminating atmospheric effects, FLAASH had higher accuracy when assessing the characteristics of different surface features (Guo & Zeng, 2012). Y. Ke, et al (2015) compared application of three different atmospheric corrections, including 6SV, Dark Object Subtraction (DOS) and FLAASH, in assessing the Normalized Difference Vegetation Index (NDVI). Their results indicated atmospheric correction as a necessary step before NDVI calculation and recognized FLAASH and 6SV as superior methods for atmospheric correction (Ke *et al.*, 2015).

In this study, as of the studies mentioned above, FLAASH model was used to perform the corrections via ENVI 5.8. ENVI image analysis software uses scientifically proven algorithms to produce reliable and meaningful information from all types of geospatial imagery through its comprehensive data analysis tools.

As it was discussed before, two steps are necessary to achieve the desired result. First, DNs are converted to radiance, which is done through ENVI's toolbox, Radiometric Calibration. The toolbox uses the image metadata from different sensors, including Landsat TM, ETM+ and 8 OLI/TIRS. By choosing the radiance as the calibration type, it uses equation 1 to calculate the radiance in units of W/(m2* m).

$$L\lambda = M\rho * Qcal + A\rho \quad (1)$$

Where,

Lλ = Top of atmosphere planetary reflectance without correction for solar angle.

Mρ = represents the band specific multiplicative rescaling factor from the metadata

Qcal= Quantized and calibrated standard product pixel value (DN)

Aρ = additive rescaling factor from metadata

The next step is to achieve the reflectance image. The software tool which results in reflectance image is an ENVI module named FLAASH (Fast Line-of-sight Atmospheric Analysis of Spectral Hypercubes). It is based on radiation transport modelling using MODTRAN (MODerate resolution atmospheric TRANsmission) code, which is the most accurate and commonly used code worldwide to predict and analyse optical measurements through the atmosphere (S. M. Adler-Golden *et al.*, 1999).

"FLAASH uses equation 2 for spectral radiance at a sensor pixel (L) that applies to the solar wavelength range (thermal emission is neglected) and flat, Lambertian materials or their equivalents. The equation is as follows" (FLAASH, 2009):

$$L = \left(\frac{A\rho}{1 - \rho eS}\right) + \left(\frac{B\rho e}{1 - \rho eS}\right) + La \quad (2)$$

Where,

ρ= the pixel surface reflectance

ρ_e= an average surface reflectance for the pixel and a surrounding region

S= the spherical albedo of the atmosphere

A and B= coefficients that depend on the spectral channel

The two variables of ρ and ρ_e correspond to the radiance reflected from the surface and radiance reflected from the surface, including atmospheric scattering. Values of A, B and S, are calculated by MODTRAN4. MODTRAN4 uses viewing and solar angles, mean surface elevation, certain atmosphere model, aerosol type and visible range to calculate the values. These values are dependent on the water vapour column amount, which might vary across one scene. In Landsat, water retrieval is not supported because the data in appropriate wavelength positions are not available. Therefore, the user chooses the relevant atmospheric model (S. M. Adler-Golden *et al.*, 1999; FLAASH, 2009). The standard MODTRAN atmospheric models are given in table 2.2. For the best result, the standard column water vapour amount must match or be somewhat greater than that of the expected for each scene. It is possible to select an atmospheric model based on the surface air temperature if the water vapour information is not available. In case none of the above is known, the atmospheric model is selected according to the seasonal latitude surface temperature mode (table 2.3).

Table 2.2 MODTRAN Atmospheric Models based on water vapour amount and surface air temperature (Flaash, 2009).

Atmospheric Model	Water Vapor (std atm-cm)	Water Vapor (g/cm^2)	Surface Air Temperature
Sub-Arctic Winter (SAW)	518	0.42	-16 °C or 3 °F
Mid-Latitude Winter (MLW)	1060	0.85	-1 °C or 30 °F
U.S. Standard (US)	1762	1.42	15 °C or 59 °F
Sub-Arctic Summer (SAS)	2589	2.08	14 °C or 57 °F
Mid-Latitude Summer (MLS)	3636	2.92	21 °C or 70 °F
Tropical (T)	5119	4.11	27 °C or 80 °F

Table 2.3 Selection of MODTRAN Atmospheric Model based on latitudinal/ seasonal dependence of surface temperature (Flaash, 2009).

Latitude (°N)	Jan.	March	May	July	Sept.	Nov.
80	SAW	SAW	SAW	MLW	MLW	SAW
70	SAW	SAW	MLW	MLW	MLW	SAW
60	MLW	MLW	MLW	SAS	SAS	MLW
50	MLW	MLW	SAS	SAS	SAS	SAS
40	SAS	SAS	SAS	MLS	MLS	SAS
30	MLS	MLS	MLS	T	T	MLS
20	T	T	T	T	T	T
10	T	T	T	T	T	T
0	T	T	T	T	T	T
-10	T	T	T	T	T	T
-20	T	T	T	MLS	MLS	T
-30	MLS	MLS	MLS	MLS	MLS	MLS

-40	SAS	SAS	SAS	SAS	SAS	SAS
-50	SAS	SAS	SAS	MLW	MLW	SAS
-60	MLW	MLW	MLW	MLW	MLW	MLW
-70	MLW	MLW	MLW	MLW	MLW	MLW
-80	MLW	MLW	MLW	SAW	MLW	MLW

Solution of equation (1) involves calculating spatially averaged radiance image L_e, from which $\rho_{e,}$ the spatially averaged reflectance is estimated through the following equation:

$$Le \approx \left(\frac{(A+B)\rho e}{1-\ \rho e\ S}\right) + La \qquad (3)$$

(FLAASH, 2009).

Spatial averaging uses "a point-spread function that describes the relative contributions to the pixel radiance from points on the ground at different distances from direct line of sight" (S. M. Adler-Golden *et al.*, 1999).

Application of average surface elevation for MODTRAN4 is essential, and the input data has to be calculated from elevation information, for which DEMs for Norway were downloaded. The following steps to calculate the average scene elevation were taken in QGIS.

Considering the DEMs in several tiles, the first step is to merge them to achieve a consistent raster file. The elevation for every satellite imagery will be calculated using the zonal statistics toolbox for which every scene has to be selected separately on the DEM raster. The selection of scenes from the DEM in QGIS is shown in figure 2.4. The zonal statistics provides several statistics properties from which we use mean.

a) b)

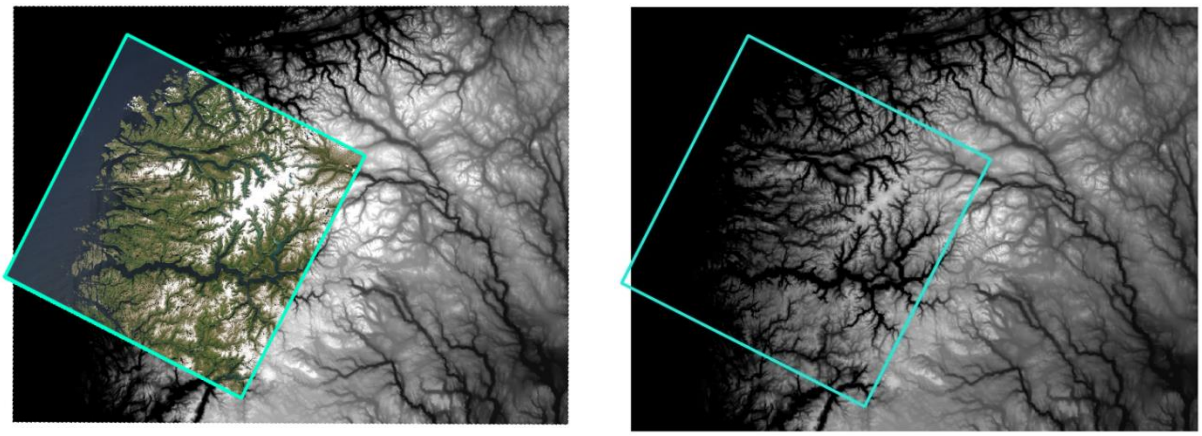

Figure 2.4 The background is a 50-meter DEM of southern Norway. Landsat-8 OLI image from 2018.06.29 is used as a sample area for calculating elevation mean. a) An example of scene area selection in QGIS, b) The average elevation will be calculated based on the selected scene's DEM shown in cyan box.

Atmospheric aerosol affects the image backscatter, surface radiance and adjacency effect. Thus, it is necessary to include that in the process of correction. In addition to the atmospheric model, FLAASH includes an aerosol model. The method is based on the work of Kaufman et al. (1997) that have shown the reflectance values of selected dark land pixels in the scene can be calculated by empirical ratios from reflectance at the 0.66 µm and 2.1 µm (Kaufman *et al.*, 1997). FLAASH calculates the aerosol amount by repeating the two equations above over a series of visible ranges. Kaufman et al. (1997) estimated an average ratio of about 0.45. This average ratio is used in order to achieve the visible range, which enables FLAASH to perform a MODTRAN4 calculation loop over water (FLAASH, 2009; Kaufman *et al.*, 1997).

With the knowledge of how atmospheric corrections are done through ENVI- FLAASH, here is a description of the required inputs to run it in each scene. These parameters include:

- *Sensor Type* that would automatically set the sensor altitude (km),
- *Ground Elevation (km)* for which the average scene elevation calculated based on the Digital Elevation Models (DEMs) in kilometres above sea level is entered,

- *Flight Date* and *Time GMT* fields, in which the date and time of the acquired image will be set automatically after choosing the image as input; otherwise, they have to be retrieved based on the metadata file downloaded with imagery,

- The *atmospheric model* has to be chosen based on what was explained previously, and in this study, it was Sub Arctic Summer for all of the imagery in use,

- The *aerosol Model* is also selected based on the standards of MODTRAN aerosol types. If the visibility is high enough (over 40 km), it is not necessary to choose the aerosol model. MODTRAN aerosol types include Rural (aerosol model in areas that are not strongly affected by urban or industrial sources), Urban (aerosol model choice for high-density urban and industrial areas), Maritime (represents areas affected by prevalent winds from the ocean with the largest aerosol particles being omitted) and Tropospheric (choice of aerosol model in calm conditions with greater visibility than 40 km).

  Aerosol retrieval in FLAASH is based on Kaufman et al. (1997) research and includes a method for estimating the scene visibility. Kaufman et al. (1997) proved the use of sensor channels around 660 nm and 2100 nm for dark land pixel retrieval. The 2-Band (K-T) option allows FLAASH to use the aerosol retrieval method. In this case, by using the multispectral sensor, assigning bands to be used for water vapour and aerosol retrieval is needed. By choosing the Kaufman-Tanre Aerosol Retrieval tab, the recommended values for upper and lower channels will be set automatically based on the retrieval conditions (over land or over water).

FLAASH atmospheric correction is ready to be applied by choosing all the parameters. Figure 2.5 presents the original Landsat 8 OLI image in comparison with the image after applying FLAASH. In images retrieved after June 2003 from Landsat 7, atmospheric correction in ENVI is used after filling the gaps in every scene.

a) b)

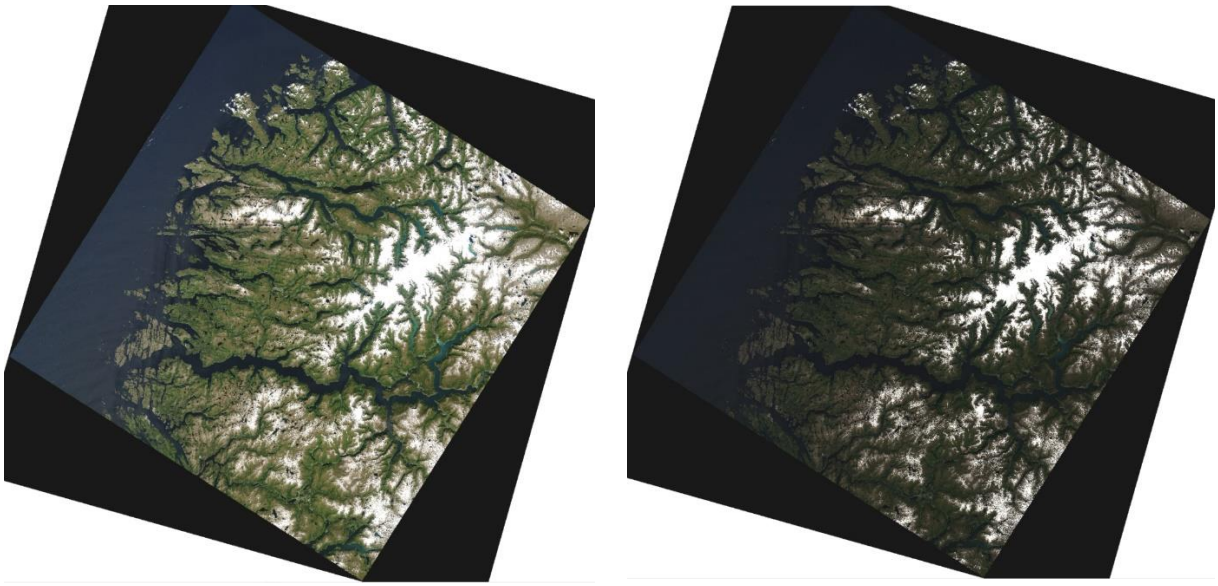

Figure 2.5 a) Original Landsat 8 OLI retrieved in Jostedalsbreen area in 2018.06.29, path/row: 201/017, b) The scene after applying FLAASH atmospheric correction.

2.4.3 Thermal atmospheric correction

Thermal Infrared Sensor (TIRS) in Landsat 8 measures the surface temperature in two narrow spectral thermal bands (bands 10 and 11) with 100-meter resolution. Meanwhile, Enhanced Thematic Mapper Plus (ETM+) in Landsat 7 includes a thermal band (band 6) with a 60-meter resolution. Thermal bands, as well as other spectral bands, are influenced by atmospheric disturbance; therefore, atmospheric correction is used as a pre-processing step for these bands.

In this study, the Thermal Atmospheric Correction toolbox from ENVI 5.3 was applied after radiometric calibration for converting DNs, for improving the thermal bands of Landsat imagery.

As in FLAASH, thermal atmospheric correction in images retrieved after 2003 from Landsat 7, is applied after filling the gaps in every scene.

ENVI's thermal atmospheric correction algorithm is based on the in-scene atmospheric compensation (ISAC) algorithm of Young *et al.*, 2002. Unlike other atmospheric compensation methods that demand meteorological data or atmospheric modelling, ISAC only makes use of at-

aperture radiance data to calculate the upwelling radiance and transmissivity of the atmosphere based on equation (4) (DiStasio Jr & Resmini, 2010; Young *et al.*, 2002).

$$\text{Lobs} = \tau B(T) + L_u \quad (4)$$

Where,

L_{obs} = observed at-aperture radiance,

τ = transmission of atmosphere,

B(T) = Planck function

L_u = upwelling radiance due to atmosphere.

The assumption here is that black bodies are objects with the highest radiance. The existence of a near blackbody surface in the scene is the second assumptions for calculating atmospheric compensation, while the first one is the uniformity of atmosphere over the scene.

ISAC analysis includes two steps, first, extraction of unscaled atmospheric compensation spectra from data and second, scaling them to quantitative compensation spectra. To accomplish that, first, the ground leaving radiance of each pixel is estimated based on the brightness temperature. Then, by fitting a straight line to the pixels with the emissivity of 1 in the produced scatterplot between the observed radiance and Planck function, the atmospheric transmission and upwelling are estimated. The slope and intercept of this line determine the atmospheric transmission and upwelling, respectively.

In this study, the only thermal band in use from Landsat 8 is band 10 since based on the U.S. geological survey's notices on Landsat 8 OLI and TIRS calibration, due to the large uncertainties on adjustment of the thermal band 11 to actual radiances, users are recommended to use only band 10 data as a single spectral band (Gerace & Montanaro, 2017).

Once thermal atmospheric correction is applied, DN values change but cannot be visually detected between images before and after, while the change can be detected through histograms

of DNs drawn using ENVI 5.3. Figure 2.6 shows DN histograms of one sample image before and after employing thermal atmospheric correction. Every pixel's DN value changes as a result as well as maximum and minimum DN value, which is shown in the figure.

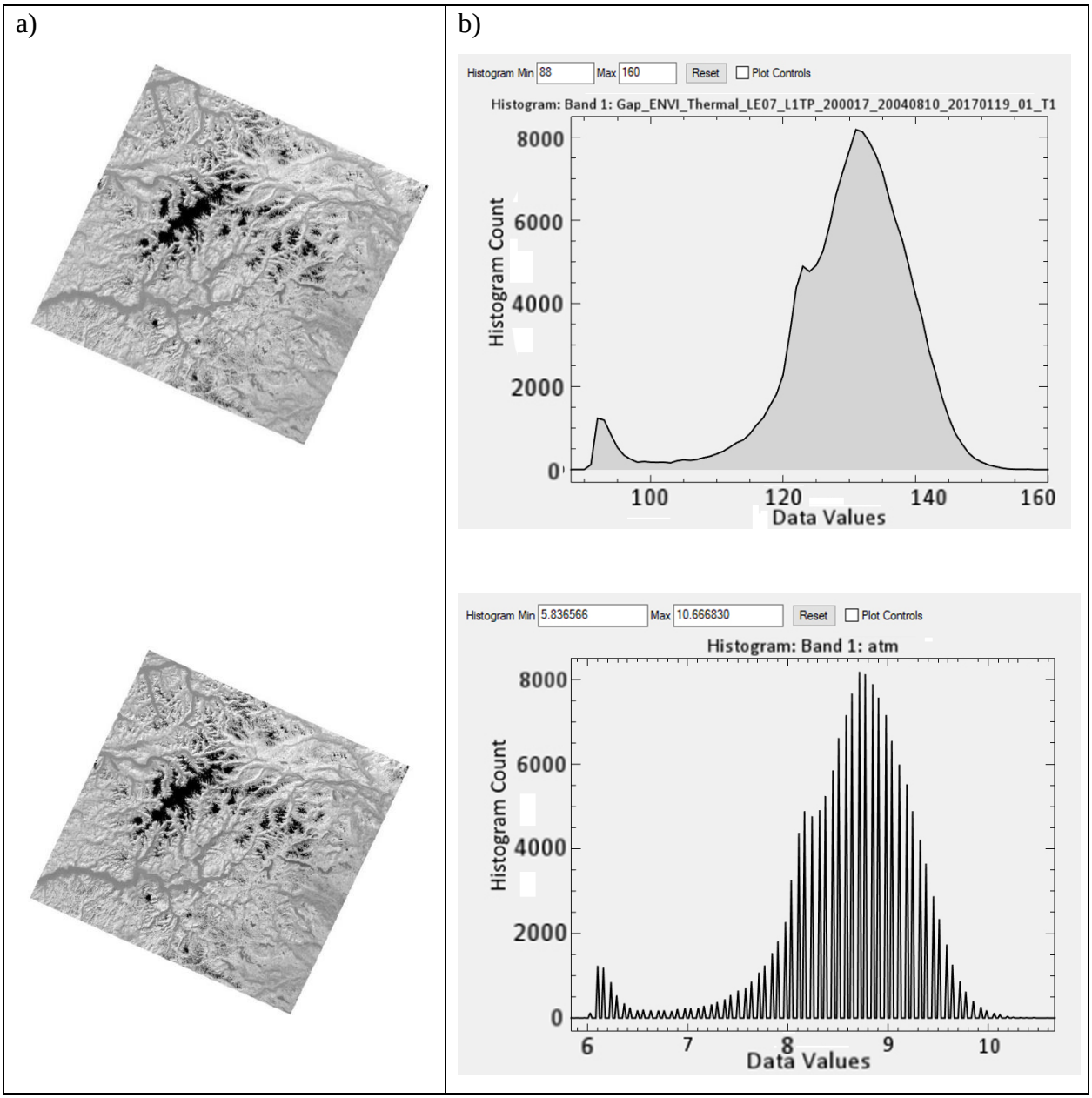

Figure 2.6 Thermal band from Landsat 7 retrieved in 2004.08.10, path/row: 200/017. a) Thermal band before (the image above) and after (lower) application of atmospheric correction, b) histograms of DN values before (above) and after (lower) application of atmospheric correction.

2.4.4 Resample Sentinel-2 bands

Sentinel-2 has different spatial resolution of spectral bands, with bands 2-4 and 8 having 10m, 5-7, 11 and 12 having 20m, and 1, 9 and 10 having 60m. Unlike Landsat level-1 images, Sentinel level-1C imagery are not resampled to the same spatial resolution. Therefore, resampling all the bands in use is the first necessary pre-processing step once the aim is classification. Resampling is the process through which the cell size of the raster changes while the extent of the dataset itself remains unchanged. The spatial resolution of Short Wave Infrared (SWIR) bands from Sentinel-2 is 20m, while the blue and Near Infrared (NIR) bands have a spatial resolution of 10m. Downsampling refers to the process through which higher resolution cells convert into lower resolution or larger cell sizes. It is a common process to achieve a homogenous spatial resolution of bands (König *et al.*, 2019). Three common methods of resampling are the nearest neighbour, bilinear interpolation and bicubic. In the first and simplest one, the nearest neighbour, the value of the closest pixel in the raw image to the computed pixel is used for the computed one. The advantage of this method is that the value of the pixel in the output image is real and not constituted from an interpolation of the algorithm like the other two methods.

The second method, bilinear interpolation, uses the average of four neighbouring pixel values to estimate the new pixel value. The four input pixel values are cell centres and located closest to the cell centre for the output cell. This method results in a smoother output image due to its averaging process, but it does not make it the best choice.

In the third technique, bicubic interpolation, the values of 16 surrounding pixels in the input image is used to calculate an interpolated value for each pixel in the output image. This method needs more computational power, so it is recommended when time is not a matter of concern (Mather & Koch, 2011).

To have a similar spatial resolution, I downsampled the blue and NIR bands to 20m resolution through the Resampling processor tool in Sentinel Application Platform (SNAP), which is freely available for download. An example of changed pixels due to resampling in band 8 is shown in figure 2.7.

The output resolution of the selected bands (blue and NIR) was set to 20m, and the Nearest neighbour was selected as the method for downsampling since all interpolation methods cause loss of high-frequency information (Mather & Koch, 2011). The result was four bands of 20m spatial resolution ready to apply classification on.

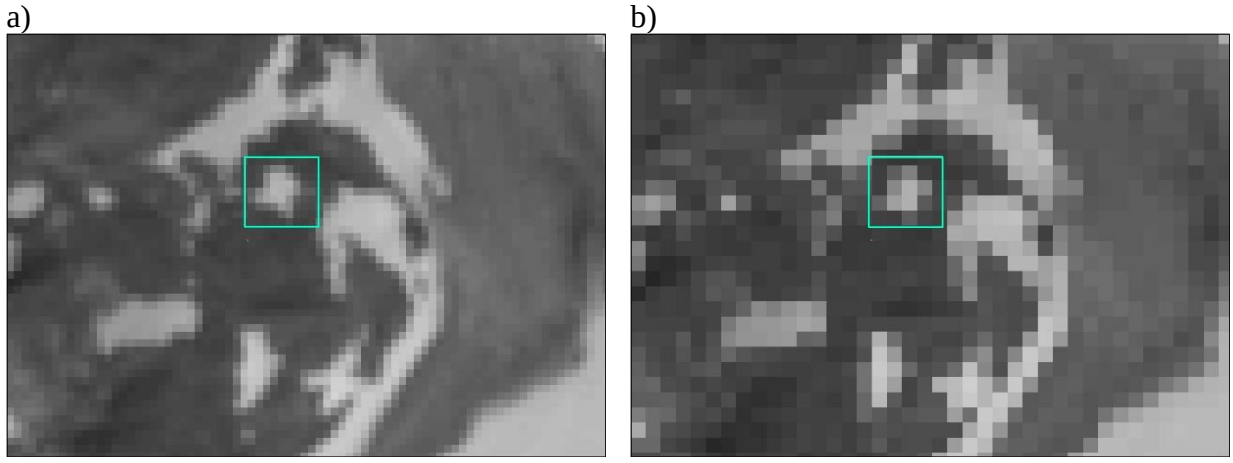

Figure 2.7 Difference of resolution and pixel size in Sentinel-2 band 8 a) before and b) after application of downsampling.

2.4.5 Composites

The next necessary pre-processing step in this study is creating composites. Every satellite has different sensors onboard, which are designed to record different amount of energy reflected in a specific portion of the electromagnetic spectrum. These sensors acquire data and save them in the form of an image, including different bands. These bands include numeric scales that show the amount of energy reflected from Earth's surface in each pixel of the imagery. The numerical values can then be converted to visual representations by using appropriate software to process their data. Thematic Mapper (TM) sensor onboard Landsat 4 and Landsat 5 include seven bands in general, from which five were also found on earlier Landsat satellites plus a thermal and a shortwave infrared band. In Landsat 7 Enhanced Thematic Mapper Plus (ETM+) sensor, a panchromatic band was added to the sensors from previous satellites. Subsequently, in Landsat 8, two separate sensors, the Operational Land Imager (OLI) and the Thermal Infrared Sensor (TIRS) acquire 11 bands overall (USGS.gov). Table 2.4 is comparing different bands and wavelengths from different sensors in the Landsat series.

To achieve a coloured image, assigning a colour from the visible portion of the electromagnetic spectrum (Red-Green-Blue) to each band is needed, so for example, instead of a black and white image, a gradation of green is observed.

Several combinations of the bands are used to create coloured images for different scientific research on geological, agriculture and urban features (Robert & Larry, 1987). Table 2.5 summarizes some of the most common band combinations for Landsat-8 OLI. After using multiple spectral band combinations, Senese A. et al. (2018) found Landsat-8 Flase Colour Composite (FCC) of bands 2, 3 and 5 useful in recognition of glacial lakes and other glacier features (Senese *et al.*, 2018). NASA's Earth Observatory uses a combination of blue and two different SWIR bands to distinguish snow, ice and clouds. In contrast, in the glacier inventory of Norway in 2012 (Liss M. Andreassen *et al.*, 2012), bands red, NIR and SWIR were used for recognition of ice and snow. Bhardwaj et al. (2015) used 1, 4, 5, 8, 9 and the thermal band in Landsat 8 OLI in application of a lake detection algorithm for glacial environments (Bhardwaj, Singh, *et al.*, 2015). Their use of thermal band supports distinguishing water features from accumulation zones of glaciers with wet snow. Bhardwaj et al. (2015) also used the thermal band to achieve a better distinction between different glacier facies and supraglacial debris and found it efficient in dividing the different surface types (Bhardwaj, Joshi, *et al.*, 2015).

Based on previous studies and recognition potential of different bands for particular land types that were addressed in this study, bands blue, NIR, both SWIR and thermal were used to generate composite images for every Landsat scene. Whereas, for the Sentinel images, due to the lack of thermal band, the other four bands were used (see table 2.4 for Sentinel-2 band specifications).

Table 2.4 Band specifications of Landsat-8 OLI. Landsat 4-5 TM. Landsat 7

Sensor	Landsat 4-5 TM			Landsat 7 ETM+			Landsat 8 OLI/TIRS			Sentinel-2			
	Band	Pixel size (m)	Wavelength (µm)	Band	Pixel size (m)	Wavelength (µm)	Band	Pixel size (m)	Wavelength (µm)	Sensor	Band	Pixel size (m)	Wavelength (µm)
CA							1	30	0.43-0.45	CA	1	60	0.42-0.457
Blue	1	30	0.45-0.52	1	30	0.45-0.52	2	30	0.45-0.51	Blue	2	10	0.43-0.53
Green	2	30	0.52-0.60	2	30	0.52-0.60	3	30	0.53-0.59	Green	3	10	0.53-0.58
Red	3	30	0.63-0.69	3	30	0.63-0.69	4	30	0.64-0.67	Red	4	10	0.64-0.68
NIR	4	30	0.76-0.90	4	30	0.77-0.90	5	30	0.85-0.88	Red edge	5	20	0.69-0.71
SWIR-1	5	30	1.55-1.75	5	30	1.55-1.75	6	30	1.57-1.65	Red edge	6	20	0.73-0.75
SWIR-2	7	30	2.08-2.35	7	30	2.09-2.35	7	30	2.11-2.29	Red edge	7	20	0.76-0.79
Pan				8	15	0.52-0.90	8	15	0.50-0.68	NIR	8	10	0.76-0.91
Cirrus							9	30	1.36-1.38	NIR	8a	20	0.85-0.88
TIR-1	6	120	10.40-12.50	6	60	10.40-12.50	10	100	10.60-11.19	WV	9	60	0.93-0.95
TIR-2							11	100	11.50-12.51	Cirrus	10	60	1.33-1.41
										SWIR-1	11	20	1.53-1.68
										SWIR-2	12	20	2.07-2.31

Table 2.5 Band combinations for Landsat 8 OLI.

Composite name	Bands
Natural color	4 3 2
FCC - Urban	7 6 4
Color infrared – Vegetation	5 4 3
Agriculture	6 5 2
Healthy vegetation	5 6 2
Land/Water	5 6 4
Shortwave Infrared	7 5 4
Vegetation analysis	6 5 4

In this study, a scene covering Jostedalsbreen in southern Norway was selected as a training area. Several composite images were produced, and maximum likelihood classification was applied on the scene retrieved on 29th of June 2018. Although the same training samples selection was used for applying MLC on different composites, the classes showed divergence in the number of pixels recognized as water bodies, ice and land. Figure 2.8 displays MLC result of the same training samples on different composites produced from the same scene. Overall composites are not visually distinctive unless zoomed into smaller areas. While the difference in pixel count is confirming variation of recognition potential of the method for each composite.

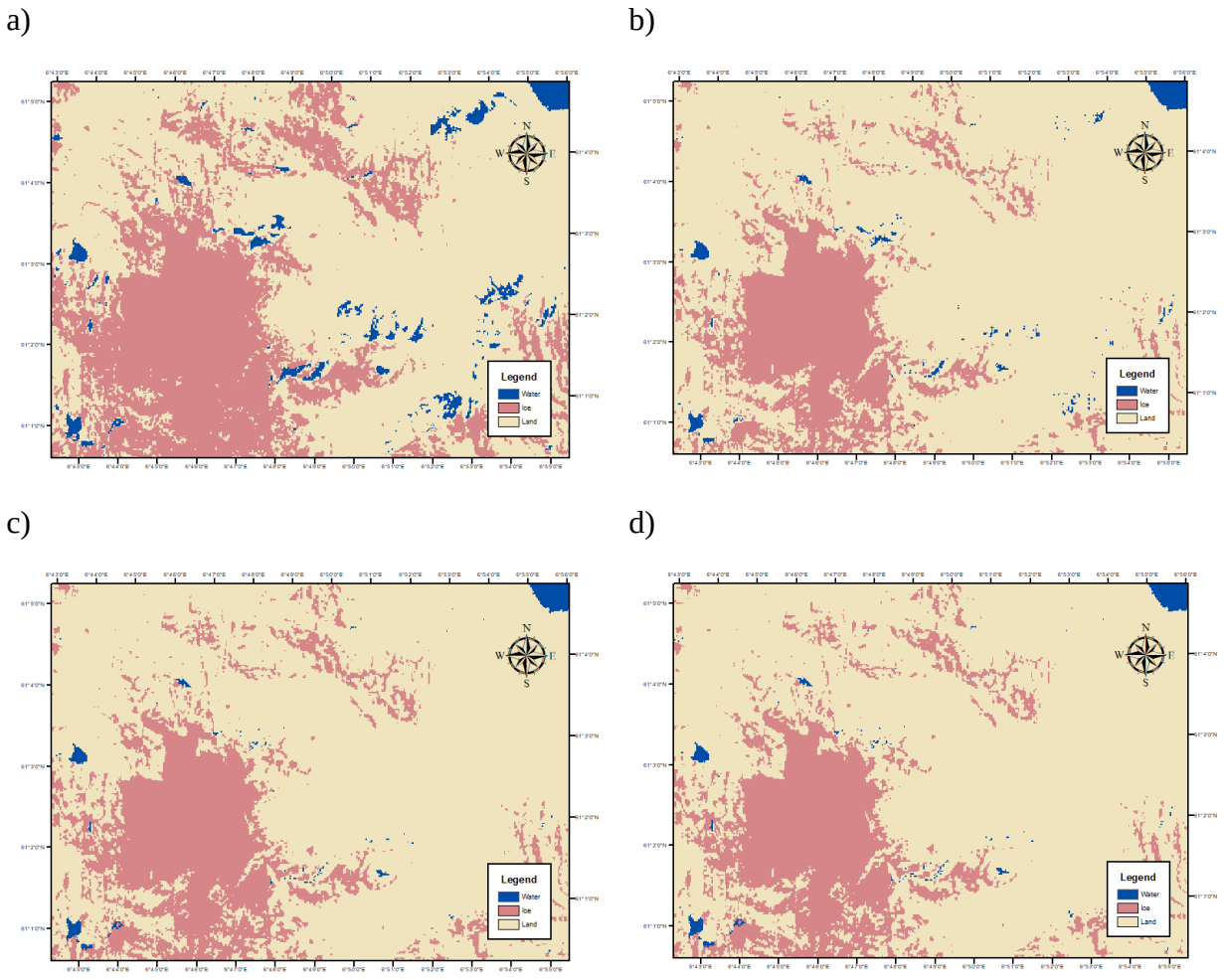

Figure 2.8 Three classes recognized by application of maximum likelihood classification on composites from a) bands 2-3-5, b) bands 4-5-6 c) bands 2-5-6-7 d) bands 2-5-6-7-10. Image used from Landsat 8 OLI, 29th June 2018.

Table 2.6 presents pixel counts for three classes from composites that were investigated for selecting the final composite to use further. By comparison with high resolution Google Earth images, composites produced by usage of blue, NIR, both SWIR, and thermal bands presented the most agreeable classification result. False colour composite of bands blue, green and NIR that was suggested by Bhradwaj A. et al. (2015) for recognition of ice and snow showed more discrepancy compared to the other composites. Figure 2.9-a points out extra water bodies recognized by using this composite. While figure 2.9-b depicts shadow improvement based on using the proposed composite in this study, including thermal band.

Table 2.6 Pixel counts for classes of water body, ice, and land after applying maximum likelihood on composites generated from the Landsat 8 OLI image retrieved above Jostedalsbreen area on 29 June 2018.

Composite	Pixel count for water bodies	Pixel count for ice	Pixel count for land
Bands 2-3-5	12459281	3395673	23714038
Bands 4-5-6	12003255	1741682	25824055
Bands 2-5-6-7	11982706	1935005	25651281
Bands 2-5-6-7-10	11989817	1917673	25661502

a) b)

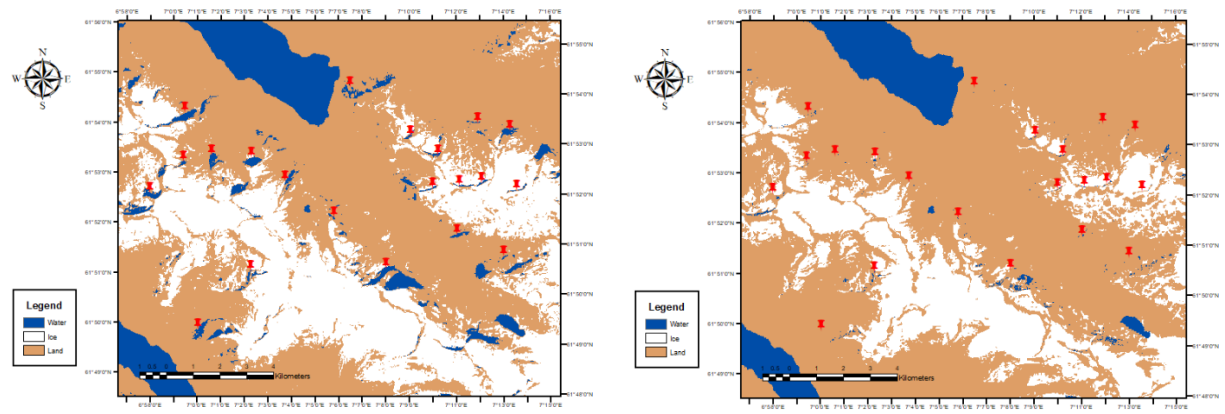

Figure 2.9 a) Maximum likelihood classes on a composite from bands 2, 3, 5 Landsat 8 OLI retrieved on 29 June 2018. Markers show shadowed slopes misclassified as water by application of method. b) Classes on a composite of bands 2, 5, 6, 7, 10 of the same image.

2.4.6 No-value pixels

The appearance of no-value pixels after application of atmospheric corrections is common as the atmospheric correction algorithms' assumption is that the target is illuminated. Thus, it can be deduced that some shadowed pixels get eliminated after applying the atmospheric corrections. FLAASH, as one of the many correction methods, is not an exception to this issue, and in every band, some pixels were assigned 0 value. Occurrence of data loss in pixels belonging to shadows

can then lead to their misclassification as water bodies by MLC. Figure 2.10 depicts this issue in classification.

Once making a mosaic image, the no-value pixels in the satellite scene, as well as the no-value pixels in the margins of every scene, get omitted. To prevent clearing out the no-value pixels inside the satellite scene, the no-value pixels in the satellite imagery were not automatically erased in this study. Instead, no-value margins in every scene were eliminated manually in ArcGIS so that the no-value pixels remain in the scene. Accordingly, mosaicking in ArcGIS was achievable afterwards.

a)

b)

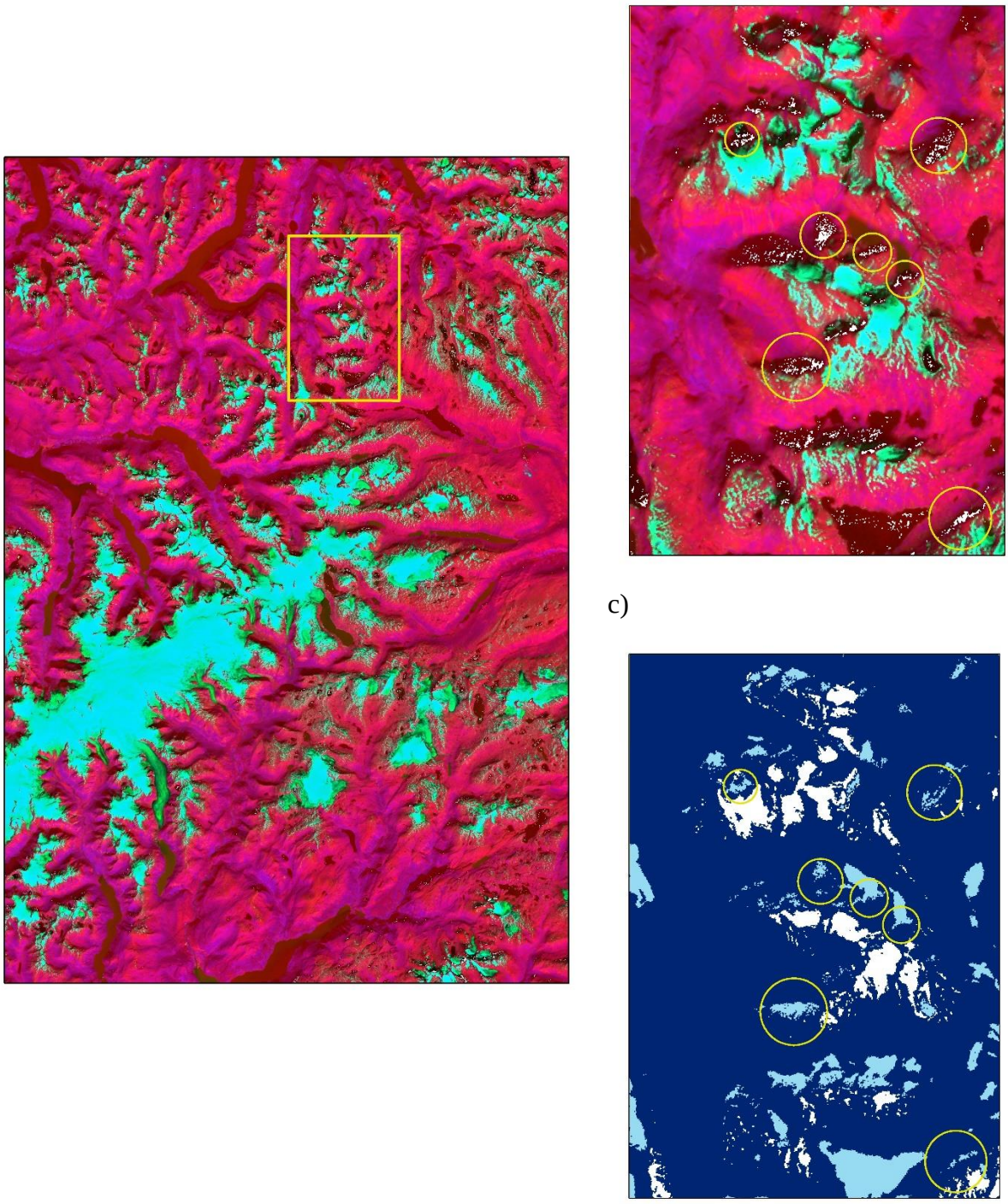

c)

Figure 2.10 a) Composite of bands blue, NIR, both SWIR and thermal from Landsat 7 in southern Norway over Jostedalsbreen area in 2004 after application of atmospheric correction b) Yellow circles depict areas where no-value pixels are in the shadow c) Appearance of no-value pixels as water bodies in some cases.

2.4.7 Composites without atmospheric correction

Having to use third-party software to correct atmospheric disturbances, as well as retaining aerosol and water vapour data, are some of the disadvantages of applying atmospheric correction on satellite imagery. Researchers avoid using atmospheric corrections in studies where the procedure can be followed without them. For instance, in the classification process where the different classes display contrasting signatures, atmospheric correction of imagery is not necessary. As Bhardwaj, Joshi, *et al.*, 2015 and Barbieux *et al.*, 2018 explain, once objects of interest show distinctive reflectance in different spectral bands of satellite images, atmospheric effects are not likely to have a significant effect on their characterization. Moreover, as Goslee, 2011 argues, in the case of assessing the changes in imagery through a wide range of time, substantial pre-processing is not necessary, and handling change detection can be done through minimum processing. Therefore, it is possible to pursue image processing without application of atmospheric corrections.

In order to test the differences of using imagery after application of atmospheric correction versus without it, I implemented my classification method on the same scenes with and without atmospheric correction. Thus, maximum likelihood is assessed based on whether the imagery was atmospherically corrected or not. For ease of following in the text, atmospherically corrected imagery and original imagery without application of atmospheric correction will be abbreviated as ACI and non-ACI, respectively.

By performing the process without atmospherically corrected images, in addition to eliminating the usage of third-party software, the issue of no-value pixels associated with atmospherically corrected imagery is solved intrinsically.

2.4.8 Mosaicking

Image mosaicking is the process of assembling several images as one of the steps before processing the satellite imagery. It is the construction of a larger image by attaching neighbouring and overlapping images. ArcGIS was used to produce the mosaics in this study.

The extent of raster data from satellite imagery, for example, from Landsat, contains null data in the borders, which is problematic when creating a mosaic from several images is the final goal. Covering parts of one scene by overlapping borders with no-value results in loss of data in those portions of the image in the final mosaic. The basic need to apply the mosaicking method in ArcGIS is to delete the no-value borders of each satellite scene ahead of applying mosaicking.

2.5 Remote sensing methods for glacial lake extraction

Availability, global coverage, spectrally and temporally varied data provided within a short time, and the least financial cost make satellite remote sensing a very popular and efficient material for monitoring and studying hardly accessible areas such as glaciers and their surrounding areas. One of the limitations of satellite imagery is their proneness to certain weather conditions that make it difficult to obtain consecutive observations due to, for instance, cloud coverage. One of the suggested methods that has been used in several studies is to use time series when the research involves observations of long-term changes of landscape features (Song, Huang, & Ke, 2014; Song, Huang, Ke, *et al.*, 2014).

With the growth in usage of remote sensing in glacial studies, different methods were developed to determine different glacial landscape features from which glacial lakes are of interest to us.

Manually digitizing water bodies from remote sensing images, thresholding, machine learning algorithms (supervised and unsupervised classifications), band ratio and indexes such as Normalized Difference Water Index (NDWI) are some of the most common methods to extract water bodies (Jha *et al.*, 2017), from which two of the machine learning algorithms were used in this study.

2.5.1 Machine learning algorithms

Machine learning algorithms are computational methods that improve automatically by getting exposed to more data to make predictions (Mohri *et al.*, 2018). The algorithms are divided into three types: 1) Supervised, 2) Unsupervised, and 3) Reinforcement learning.

In supervised machine learning algorithms, the learning process is a function of input-output pair. The algorithm analyzes the training samples as input values to produce the inferred function or the output and make the final product that is the prediction. While, in unsupervised learning, no training data is available, and the learning process is based on unlabeled training data to make predictions for all unseen points. Reinforcement learning is a mixed training and testing process through which the learner interacts with the environment. It involves affecting the environment and receiving a reward for every action. The learner must either explore the actions to gain more information or use the information it has already collected (Mohri *et al.*, 2018).

Image classification is a machine learning process that can be done through supervised and unsupervised methods, which are also widely used to extract water bodies in remote sensing imagery. This study focuses on the application of supervised classification methods that will be explained further in the following sections.

2.5.2 Supervised classification

As suggested by its name, the analyst supervises the classification by establishing various pixel values as signatures that associate every class in supervised classification. These are called training samples or areas, and they are representing certain surface types. Following the establishment of training datasets, the algorithm classifies the whole image based on the training datasets. Maximum Likelihood Classification (MLC) and Support Vector Machine (SVM), among well-known supervised classification techniques that are widely used in remote sensing studies (Mondal *et al.*, 2012), are explained in the following sections.

2.5.2.1 Maximum likelihood classification

Among supervised classification methods used, MLC is one of the commonly used algorithms that use the training sample data to calculate necessary statistics like mean and variance-covariance and run a probability function. The basic assumption in maximum likelihood is that statistics for each class is normally distributed. It then calculates the probability of an observation belonging to a specific class (Myung, 2003). Like any other supervised classification algorithm, maximum likelihood in remote sensing uses the relation between the surface characteristics and the set of predefined classes in the selected pixels to predict and identify the classes of the rest of the pixels.

To implement MLC the following function for each pixel is calculated:

$$\text{“}g_i(x) = \ln p(\omega_i) - \tfrac{1}{2} \ln \left|\sum_i\right| - \tfrac{1}{2} (x-m_i)^T \sum_i^{-1} (x-m_i) \qquad (5)$$

where:

i= class

x= n-dimensional data (n is number of bands)

$p(\omega_i)$= probability that class ω_i occurs in the image and is assumed the same for all classes

$\left|\sum_i\right|$ = determinant of the covariance matrix of data in class ω_i

$\sum_i^{-1}$ = its inverse matrix

M_i= mean vector”

(Richards & Richards, 1999)

2.5.2.2 Implementation of Maximum Likelihood Classification in ArcGIS

In order to perform the classification of the targets over the surface in this study, the built-in MLC tool in ArcGIS was used. The tool assigns cells to classes defined in the signature file when they have the highest probability based on the mean vector and covariance matrix of the class signatures. In the tool specifications for this work, *EQUAL* option was assigned for *A priori probability weighting* so that 'each cell was assigned to the class to which it had the highest probability of being a member' (ArcGIS). The *Reject fraction* is the value that defines the portion of pixels that remain unclassified and assigning 0 means every pixel gets classified in the input image.

2.5.2.3 Support Vector Machine

SVM is another type of supervised classification methods. It uses a decision surface or a hyperplane that divides a dataset into classes by maximizing the margin between the classes. The data points closest to the hyperplane are called support vectors that are critical to the dataset as removal of these points results in altering the position of the hyperplane. The margin is the distance between the points and the dividing line. Once there is maximum margin, proper generalization is reached, and the hyperplane becomes optimal (Cortes & Vapnik, 1995; Hsu *et al.*, 2010).

Once the dataset is linearly non-separable, SVM can be adapted to a nonlinear classifier using nonlinear kernels. To classify a non-linear dataset, it is necessary to move from a 2D view to a 3D view of data by transforming them into a higher dimension. The idea behind it is that by a high enough dimension, a hyperplane to divide classes can always be found. By repetition, more hyperplanes can be found to separate all classes in n-dimension space (Cortes & Vapnik, 1995).

For a training set of pairs (x_i , y_i), I = 1,…l where $x_i \in R^n$ and $y \in \{1, -1\}^l$, support vector machine solves the following optimization problem:

$$\min_{w,b,\xi} \frac{1}{2} w\,T\,w + C \sum_{i=1}^{l} \xi i \qquad (6)$$

Subject to $y_i (w^T \phi(x_i) + b) \geq 1 - \xi_i, \quad \xi_i \geq 0$ (7)

Here function ϕ develops training vectors x_i into a higher dimension, then SVM chooses the hyperplane with the maximal margin in this dimensional space. $C>0$ is the penalty parameter which will be explained further (Hsu *et al.*, 2010).

There are different types of kernel available from which four of the most common ones are explained here, linear, polynomial, Radial Basis Function (RBF), sigmoid.

The use of different kernel types depends on the dataset. Linear kernel works well when the dataset is linearly separable and consists of only two dimensions. If it is not linearly separable, applying the RBF kernel is more efficient. What it does is to create non-linear combinations of the features to take samples into a higher dimensional space and use a linear boundary or a hyperplane to divide the classes. Each kernel function can be mathematically defined as follows:

Linear $K(x_i, x_j) = x_i^T x_j$

Polynomial $K(x_i, x_j) = (g x_i^T x_j + r)^d, g>0$

RBF $K(x_i, x_j) = \exp(-g\|x_i - x_j\|^2), g>0$

Sigmoid $K(x_i, x_j) = \tanh(g x_i^T x_j + r)$

In the polynomial kernel function, ^{d} is the degree of the kernel polynomial. By increasing this parameter, the boundary between classes is delineated more accurately. Value 1 is a first-degree polynomial function and delineates a straight line between two classes in case they are distinctive in the first place. While more commonly, the imageries have mixed pixels and variations, and increasing the polynomial value is necessary to produce a more accurate distinction between the classes.

The “r” in Polynomial and Sigmoid kernel functions is the kernel bias. With more bias, the error in prediction increases. The “g” in Polynomial, RBF, and Sigmoid kernel functions is the gamma

parameter. Gamma value controls different transformations. Penalty in SVM is what allows training errors and controls the compensation of rigid margins. In non-separable training sets, by setting the penalty, a degree of misclassification is allowed. Based on the knowledge of parameters involved in SVM, the method was applied through ENVI program.

2.5.2.4 Implementation of Support Vector Machine in ENVI

In this study, SVM was implemented through ENVI. ENVI uses the pairwise classification strategy for multiclass classification to apply SVM. The applicable parameters in use were described in section 2.5.2.3.

In ENVI's SVM classification toolbox, four Kernel types are available to use, from which the Radial Basis Function (RBF) is the default that is the most used type of kernel as well (Hsu *et al.*, 2010). Other types of kernel available in ENVI are linear, polynomial, and sigmoid.

The "r" in Polynomial and Sigmoid kernel functions is the kernel bias which is set to 1 as default in ENVI while applying SVM. The "g" in Polynomial, Radial Basis Function and Sigmoid kernel functions is the gamma parameter. Kernel's function is to transform the data into a high dimension to make the data separable. Gamma value controls different transformations. The default gamma parameter in ENVI is the inverse of the number of bands used in the image being used for the application of SVM. In this study using five bands, the default gamma value was 0.200.

Penalty in SVM is what allows training errors and controls the compensation of rigid margins. In non-separable training sets, by setting the penalty, a degree of misclassification is allowed. The default is set to 100 in ENVI.

Hsu et al. (2010) proposed to use RBF as the first choice of kernel function since it is the most compatible with imagery with training samples with less overlap; secondly, because RBF kernel has less numerical difficulties. Here, $0 < K_{ij} \leq 1$ is in contrast with polynomial kernels in which the kernel value may stretch between zero to infinity while the degree is large. (Hsu *et al.*, 2010).

The next step in applying SVM is to choose the right penalty and gamma values. These values are not predefined to use; hence to identify the best gamma-penalty values, it is suggested to perform a cross validation (Geospatial, 2010; Hsu *et al.*, 2010). As a common method of classification evaluation, k-fold cross validation is performed, in which k is usually between 4 and 10. For instance, to apply a 4-fold cross validation, the original sample is divided into four subsamples where these subsamples are used as training data. Each time, three subsamples are used as training, and one is left for validation. Accuracy of classification is evaluated every time, and after applying the classification four times, average accuracy is calculated to get an overall result.

2.5.3 Training sample sets/ Region Of Interest

Accuracy of supervised classification of satellite images depends on the accuracy of the training sample sets, the skill of the individual applying the training and processing the image, and the spectral distinction between classes. If some classes have close spectral reflectance, recognition of algorithm may be affected and lowered for dividing them; therefore, misclassifications tend to be higher. If the training data are not representative of the classes, the results will not be as accurate and discriminating as necessary (Barandela & Gasca, 2000; García-Borroto *et al.*, 2014). Minimizing the overlap between classes produces a better separation in the final classified image with lower probabilities of misclassified pixels which causes the process prior to the actual classification to take more effort and time.

While the procedure for training data selection was the same in both supervised classification methods in use in this work, the tool to collect pixels as training samples was called differently in ENVI. The Region Of Interest (ROI) tool in ENVI is designed to collect training samples as the Training Sample Manager tool in ArcGIS does.

2.5.3.1 Signature file for maximum likelihood

The focus in this study was on the water bodies which showed distinct signature from the rest of the image. Therefore, pixels with the distinct characterization of ice and water bodies for training sample sets were assigned, and any other surface type, e.g., urban, agriculture, land, and rocks, were grouped under one class since they were not of specific interest to the study for performing the classification procedure. Training samples for the three classes were then visually selected and saved as a signature file. To achieve a more accurate classification, which is more comparable to reality, it is necessary to collect the training samples precisely and homogenously, as Lillesand and Kiefer (2000) suggested (Lillesand, 2000).

The training samples from composite images were selected in ArcMap and compared with the same scene's natural-colour and Google Earth high-resolution satellite imagery. It is common to see water bodies everywhere in a satellite imagery scene in Norway, although it is obvious that some are very different in size. Therefore, finding samples for water bodies and land was not a challenging task. While distribution of glaciers in each scene was more complicated, it was necessary to limit training samples for the class of ice on the glacier areas. In order to keep the number of samples homogenous in the scene and solve the issue of the class of ice, a mesh of 9 cells was applied to the imagery to select a uniform number of samples. The same number of samples in every mesh was picked, and the training samples for ice were selected from the mesh cells that contained icecaps, glaciers, and ice patches.

In order to achieve a more successful classification, it is essential to have a sufficient number of training samples for each class but, that does not mean the same number has to be selected for every one of them. The probability of over or under-estimation of a class will be lessened by using an optimal number of training samples. As the optimal number is not pre-defined for such use, training samples were selected, and several signature files were assigned to apply maximum likelihood in one representative scene, and the results were compared with the scene’s natural colour image. As predicted, with over-training the method, a precise classification cannot be reached, while a few trials with several training samples makes it possible to have an almost optimal signature file that is able to classify an image more thoroughly.

Towards improving the accuracy of the classification, a fragmentation of the larger area of study was used, and the procedure was practised separately before applying to the whole area. The fragmentation was in a representative scene in southern Norway that includes Jostedalsbreen, the largest icecap in mainland Norway (NVE), and the surrounding area, which includes several glacial lakes. A signature file was assigned and created for the three classes in this scene on the composite of bands from Landsat-8 image in 2018.06.29. Figure 2.11 shows the three classes from the maximum likelihood classification method in this area.

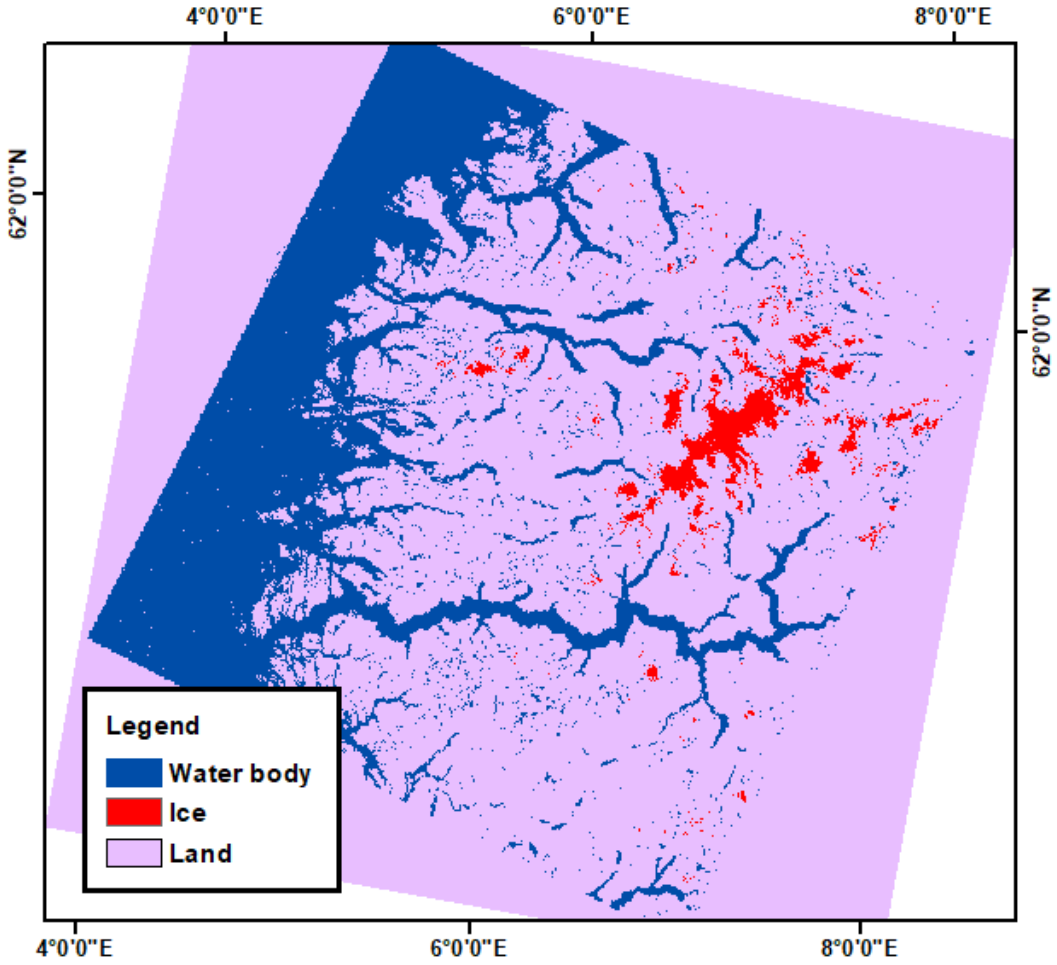

Figure 2.11 Application of maximum likelihood classification in the scene from Jostedalsbreen and the surrounding area in southern Norway. Red represents ice, blue, water bodies and yellow, land classes. The Landsat-8 image was retrieved in 2018.06.29.

2.5.3.2 Area division

As explained previously in 2.5.3.1, a representative area was selected to improve the training samples. Jostedalsbreen scene contains Norway's largest glacier and therefore clearly recognizable ice and water areas to collect the training samples.

After application of MLC on a mosaic achieved from image tiles from all over Norway,

there was a visually obvious lack of recognized pixels of ice and water in areas in northern Norway in the resulted classification as presented in figure 2.12.

The issue could be due to the difference in satellite imagery properties such as sun azimuth, date and time of retrieval in different parts. As Norway is located between 58° and 71° north latitudes, imagery achieved on the same date in north and south can present accordingly different properties. Therefore, it is not advisable to use the same training sample signatures in the whole country.

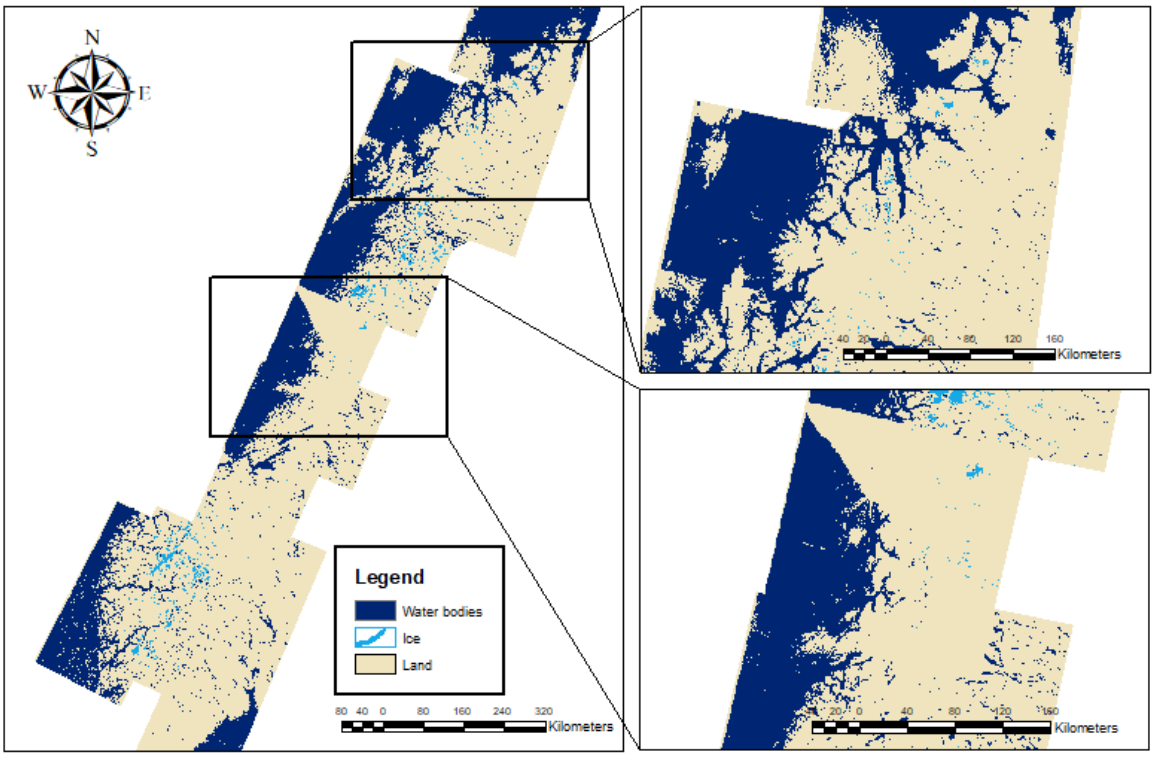

Figure 2.12 Application of maximum likelihood on the mosaicked imageries by using training samples signature from the Jostedalsbreen scene located in southern Norway

To avoid this problem, we divided the country into three regions of south, mid- and north Norway (figure 2.13). The division is based on the geographical location to provide consideration of image properties. Thus, although south western Norway has a significant geographical difference from the south east, their location in the same latitude places them in the south Norway division in this study.

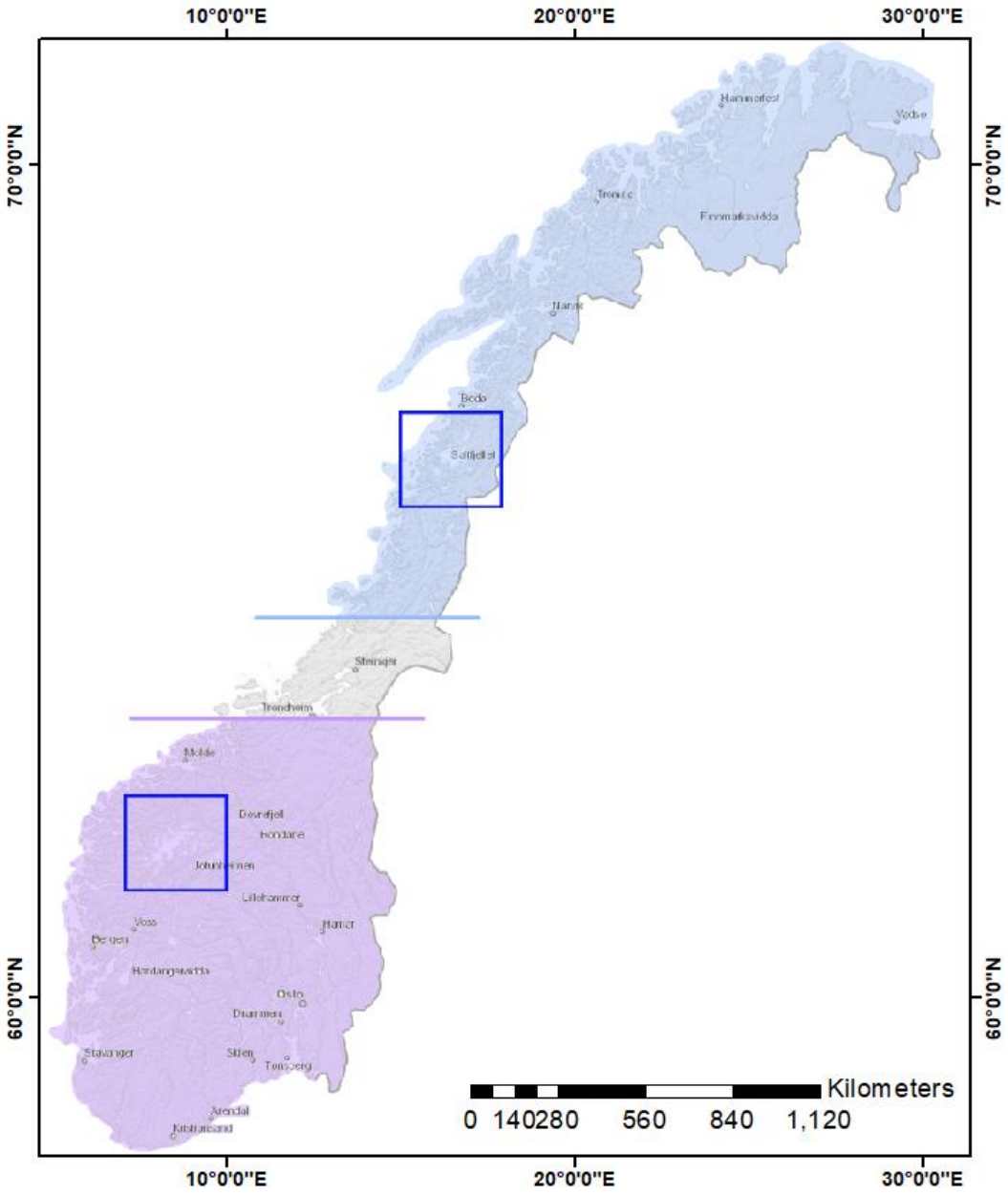

Figure 2.13 Division of Norway based on geographical and satellite image properties into south, mid and north Norway. Location of representative scenes in every division. Blue boxes show the representative areas for collecting

training samples in the south from the tile covering the Jostedalsbreen and north from the tile covering the Østre and Vestre Svartisen.

Training samples were then selected in one representative scene in each division. The scene containing Jostedalsbreen was used as the representative scene for south Norway, while as mid-Norway contains too few ice pixels in the imagery, collecting efficient training samples was not achievable. The fact that the only ice pixels in the images were located close to the south Norway division led us to merge that tile of imagery from mid-Norway to the south Norway division to expect better results.

The representative scene in northern Norway was selected from a scene containing Vestre and Østre Svartisen glaciers that are the second and fourth largest glaciers in Norway, respectively (figure 2.13).

2.5.4 Maximum likelihood classification in ENVI

To ensure the comparability of the two programs, MLC was applied in ENVI as well, and the results were compared with the ones from ArcGIS. MLC in ENVI follows the same rules as in ArcGIS. "Unless a probability threshold is selected, all pixels are classified, and each pixel is assigned to the class that has the highest probability" (Geospatial, 2010). ROIs were then selected for every class as explained in the training samples for MLC in ArcGIS.

In the *Set Probability Threshold* field, no threshold was used to classify all the pixels in the image. By selection of thresholds, a value is chosen for ENVI to classify all pixels over that. This way, similar to ArcGIS *Reject fraction*, pixels with values lower than the threshold do not get classified.

2.6 Glacial lake extraction

There are three classes as the result of applying maximum likelihood classification, ice, water bodies and land, which in this study is defined as every other land type that exists in the imagery. Based on the definition of glacial lakes in this study, the first step to extract glacial lakes from

the rest of water bodies is to define a buffer zone of 100 meters around the glacier outlines. By using the buffer toolbox in ArcMap, it is possible to draw the 100m glacier buffers around glacier outlines provided by NVE. Considering this matter, maximum likelihood was applied using imagery achieved in relevant years to the glacier outlines. The whole process is summarized in figure 2.14.

After defining a buffer zone around the glaciers, the lakes within this distance are selected automatically in ArcMap and saved as a separate layer of polygons. The result is a layer including all the water bodies recognized by maximum likelihood within the buffer zone.

By visually inspecting these selected water bodies, it was observed that some of the selected polygons are, in fact, not water bodies but shadowed slopes that were wrongly classified as water bodies due to similar spectral characteristics of shadow with water bodies in the satellite images. While, for instance, water remaining from previous glacial cirques can form a glacial lake in a slope, generally mean velocity of water has a reverse relationship with the surface slope (Sadler, 1891) so, as a general rule, lakes cannot form in slopes. As mentioned previously (see section 2.1.3), DEMs have been used by researchers to define potential areas for existence of lakes (Huggel *et al.*, 2002; Li & Sheng, 2012). Li and Sheng, 2012 consider glacial lakes when they form on slopes with less than 10° gradient.

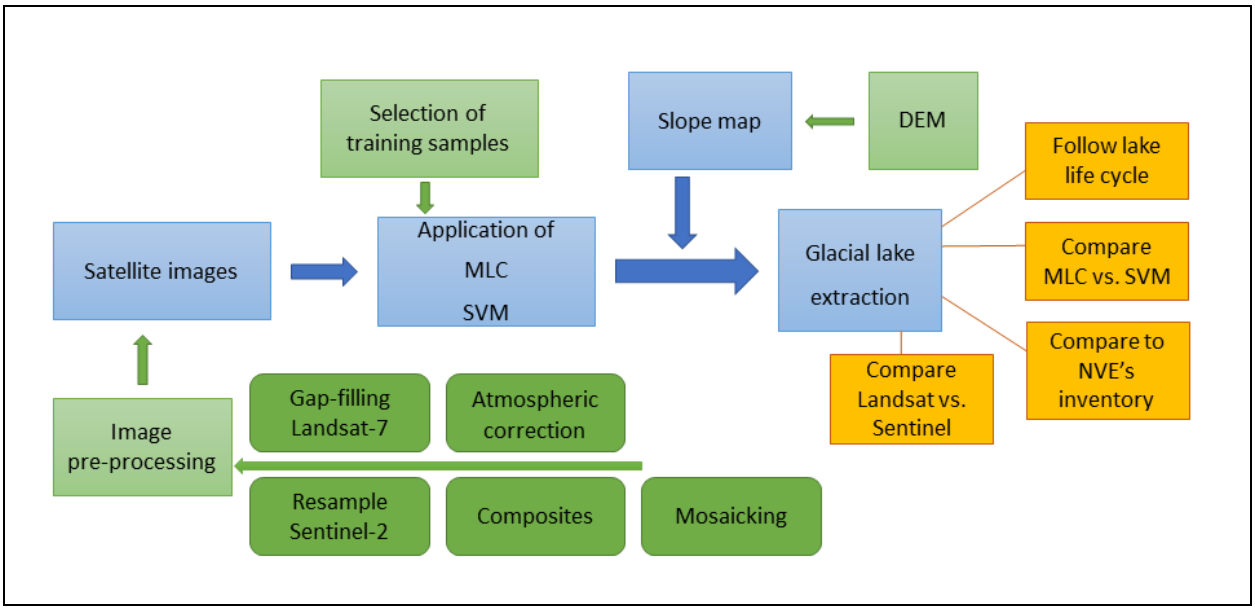

Figure 2.14 Glacial lake extraction and processing based on satellite images and machine learning methods

To resolve the issue of misrecognition of shadowed slopes for lakes, I employed a slope map constructed from the DEMs of the study area. A polygon layer of water bodies extracted from the maximum likelihood application was then intersected with the slope map. Intersection uses the common areas between two or more selected features and creates a new feature. The new feature includes features of different layers in one. In this case, intersection of the two layers provided slope characteristics of the recognized water bodies in the maximum likelihood layer.

In the intersected layer, it was obvious that water bodies recognized in slopes were not initially properly classified. Therefore, it is necessary to separate those from the rest of the water body class. In this study, I eliminated polygons of water body layer that were intersected with slopes over 14 degrees. The remaining polygons of water bodies contained lakes more realistically.

3 Results:

As discussed in Chapter 1, the main database for lake and water catchments in Norway has been generated and maintained by NVE including regional glacier and glacial lake inventories. Although a combination of machine learning algorithms and remote-sensed observations has become commonplace in studies assessing glacial lake distribution over large regions, glacial lake inventories in Norway are largely based on manual mapping and have yet to benefit from these recent trends enabling an automated classification of water bodies. This study is the first attempt to quantify the potential of machine learning algorithms and satellite data with different temporal and spatial resolution to be adapted on a Norway-wide scale in future glacial lake inventories. Maximum likelihood and support vector machine methods have been selected as two of the commonly used machine learning algorithms for classification tasks of comparable complexities (Bolstad & Lillesand, 1991; Shlien & Smith, 1975; Sun *et al.*, 2013). These are combined with the Landsat and Sentinel datasets to tease out the specifics of each classification method and the potential to extend a relatively short, yet higher-resolution observational record obtained with Sentinel into the historical period of nearly 50 years enabled by lower resolution observations with Landsat. The technical analyses related to a systematic evaluation of the above methods and datasets have not only revealed their relative strengths and weaknesses but also produced a number of unexpected scientific findings related to the nature of glacier-glacial lake co-existence and challenges associated with the studies of such complex environments.

To enable the scientific analyses below, the satellite data have undergone the following preprocessing steps that are detailed in Chapter 2: (1) Gap filling of Landsat 7 images (see section 2.4.1), (2) Atmospheric corrections (see Section 2.4.2), (3) Thermal atmospheric correction (see section 2.4.3), (4) Resampling of Sentinel-2 images (see section 2.4.4), (5) Generation of composites (see section 2.4.5) and (6) Mosaicking (see section 2.4.8).

This chapter first contrasts the results of maximum likelihood classification (MLC) on the atmospherically corrected satellite images (ACIs) and the original uncorrected images (non-ACIs) over a Norway-wide scale and then zooms into differences between the outcomes of

glacial lake recognition in Landsat and Sentinel images in the southern study domain (Section 3.1). Using the advantage of the Landsat series that extend over five decades into the past, Sections 3.1.3-3.1.4 compare the delineated glacial lakes during three time intervals - 1988-1997, 1999-2006 and 2018-2019 - and follows the reconstructed stages to present a synopsis of local changes that occurred in these environments during the last ~30 years. Finally, Section 3.2 puts MLC to a hard test by contrasting its performance with the Support Vector Machine (SVM) classification algorithm on both Landsat and Sentinel-2 images.

3.1 Time-evolved classification of glacial lakes: Implications for the use of atmospheric corrections

In this section, I present the results of MLC on the pre-processed Landsat imagery spanning several years and historical periods aligned with the existing glacier inventories in Norway (see section 1.2). The focus on the time periods with glacier inventories is justified by the fact that historical glacier outlines are needed for the separation of glacial lakes from the rest of water bodies classified by the method. The first focus period of the MLC application is therefore 1999-2006, for which NVE has provided a complete glacier inventory for whole Norway. The second focus period is 2018-2019 for which at the time of study NVE was in a process of glacier and glacial lake outlining, thus limiting the application of classification methods to southern Norway. Finally, the third focus period is 1988-1997 with the analysis spanning northern and southern Norway except for the Jostedalsbreen area that was excluded due to lack of glacier outlines in the inventory.

In order to delineate glacial lakes from the rest of water bodies, an application of MLC within the three focus periods, is followed by several post-processing stages that are summarized here to prevent repetition in every section. The first stage after the application of MLC on the satellite images is to generate a mosaic image to separate water bodies from the other land types. Extraction of glacial lakes is carried out at the second stage by first intersecting the slope layer to remove misclassified shadowed slopes from the water body class and then considering a buffer of 100m from glacier outlines. These stages naturally lead to a final set of glacial lake outlines

that are separated from the rest of water bodies and other land types (see section 2.6 for more information on the steps).

3.1.1 Selection of training samples for Maximum Likelihood Classification of land classes

Due to remarkable dependence of the accuracy of supervised classification on training samples, it was first necessary to evaluate the collected samples and create signature files. The selection strategy for training samples has therefore been tested on a representative area where I evaluated the skill of classification using scatterplots of the three target surface classes (land, water and ice) using different imagery bands. Figure 3.1 shows scatterplots for the Jostedalsbreen representative area produced in ArcMap, where *x* and *y* axes feature blue, NIR, SWIR1, SWIR2 and thermal bands numbered as 1 to 5, respectively.

a)

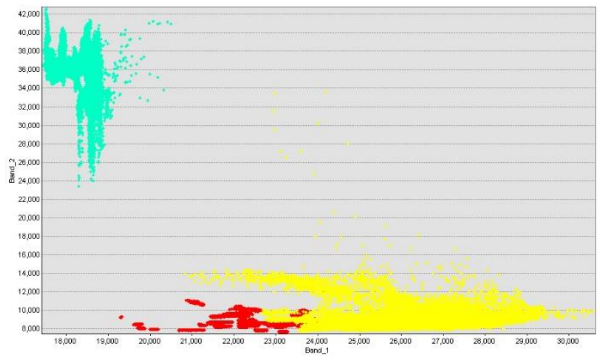

b)

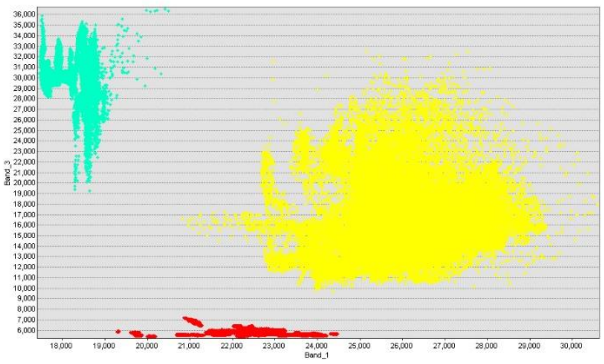

c)

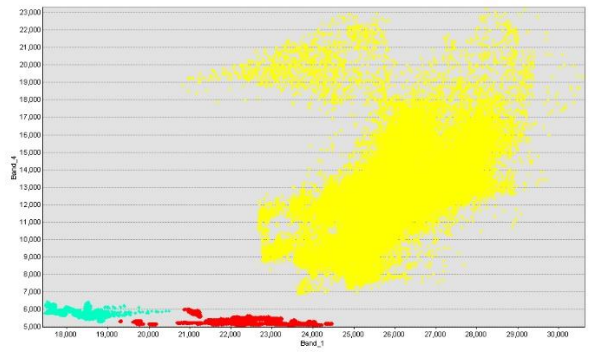

d)

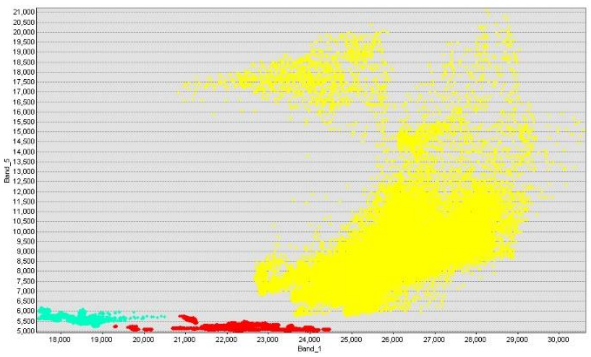

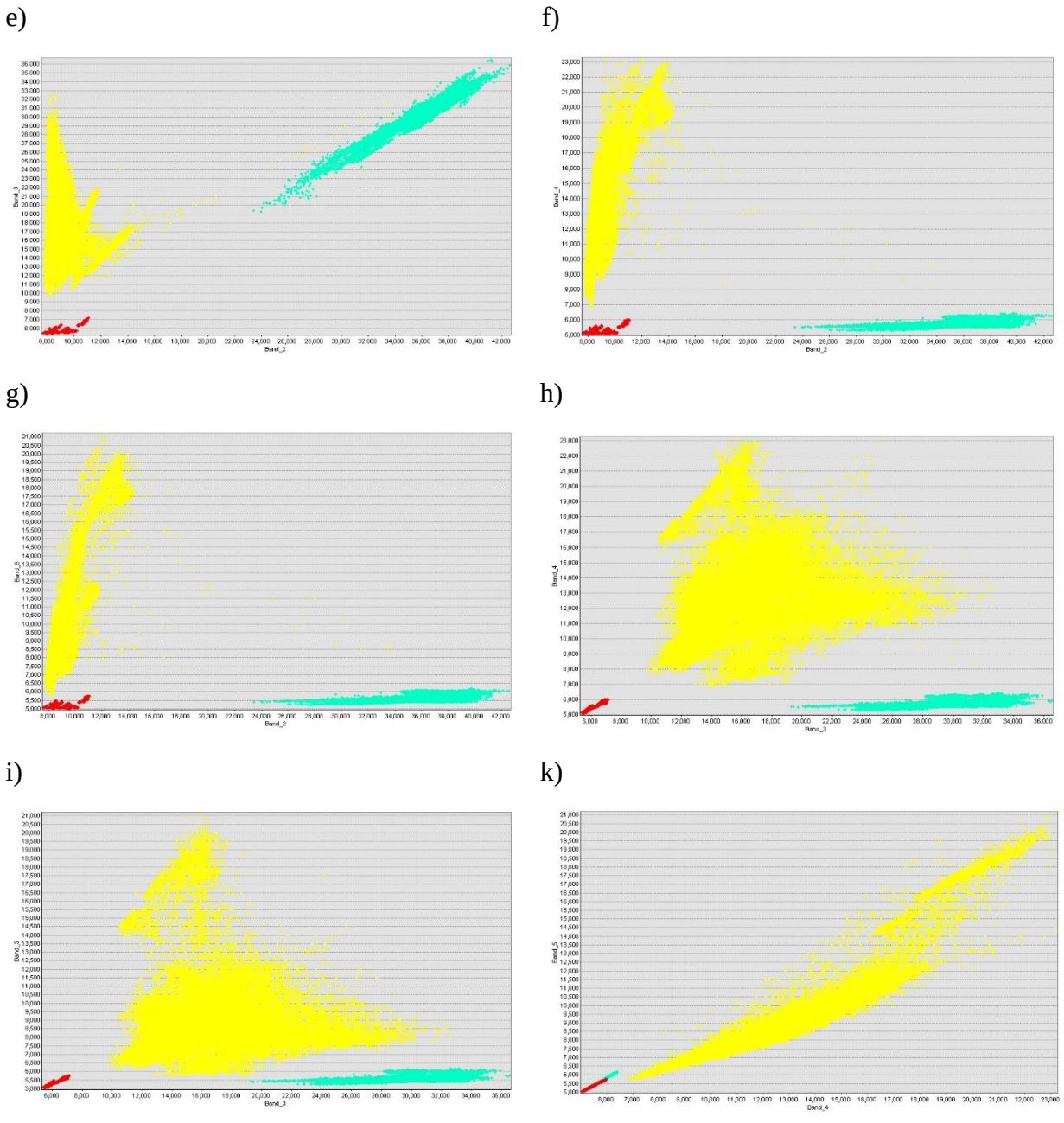

Figure 3.1 Scatterplots of the three classes for the representative area in Jostedalsbreen. X and Y axes show different bands. Each figure displays separability of classes based on comparison of band pairs. Bands 1-5 represent blue, NIR, SWIR1, SWIR2, and thermal bands, respectively. Classes in scatterplots: Yellow: land, Red: water bodies, cyan: ice. Landsat-8 image retrieval date: 2018.06.29.

Two characteristics define a good selection of training samples in a scatterplot: firstly, the points in every class should form a fairly tight cluster, and secondly, classes should not overlap. Disregarding these two factors can lead to a misclassification of land classes. Based on figure 3.1, it can be inferred that blue-SWIR1, NIR-SWIR1, and SWIR1-SWIR2 band pairs show a

better recognition skill for the three classes, as every cluster is thoroughly bundled and separated from the two others (figure 3.1-b, e, and h). Since the separation of water bodies from the other two classes is of a higher priority for this work, the SWIR1-thermal band pair is also considered essential due to its impressive skill in shaping a well-defined cluster of pixel values belonging to water bodies (figure 3.1-i).

Albeit the fairly satisfactory separation of classes visible in figure 3.1 based on an image from the 29th of June 2018, the situation changes drastically if it gets replaced by an image from the 25th of May. Although both images cover the same area and the same year, the use of the latter results in conflicting scatterplots due to seasonal snow and ice cover. To demonstrate the importance of the correct sample selection, the same training samples have been used on the image from May as those selected for the image from June in Figure 3.1. However, this time their alignment with the correct land type was not visually inspected, leading to an erroneous assignment of training samples that were originally selected as representative of one of three targeted land classes. For example, some pixels that were included in the training samples as water bodies in the image from June because liked to locations covered by seasonal ice in May, while training samples for the land class coincided with ice- or water-covered surfaces. As demonstrated by scatterplots in Figure 3.2, the above poor alignment between the training samples and the surface types has created an immense overlap between the three classes, hindering the pixel association. These scatterplots vividly demonstrate that the training samples for one scene are not directly transferable to another scene without adjustments, leading to unreliable MLC applications, marked by misclassification of images and assignment of incorrect land classes.

a)

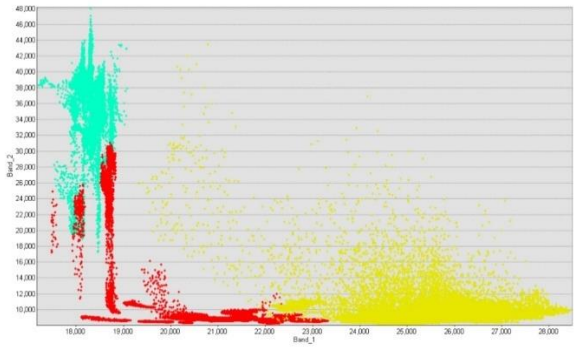

b)

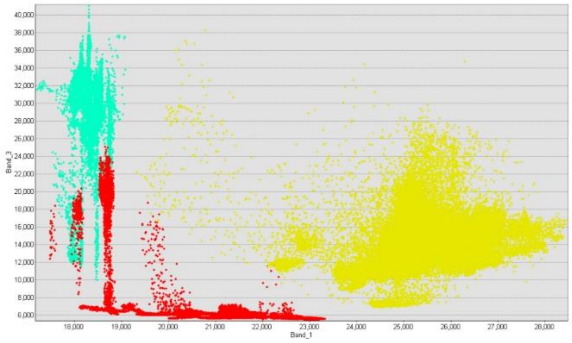

c)

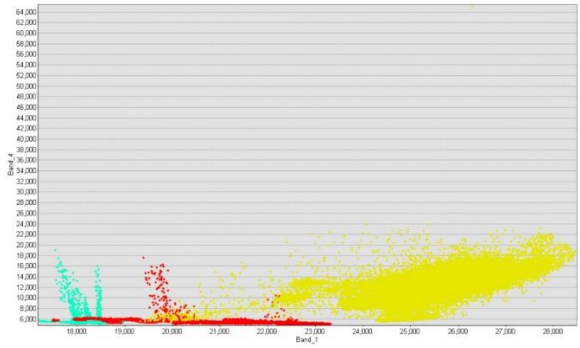

d)

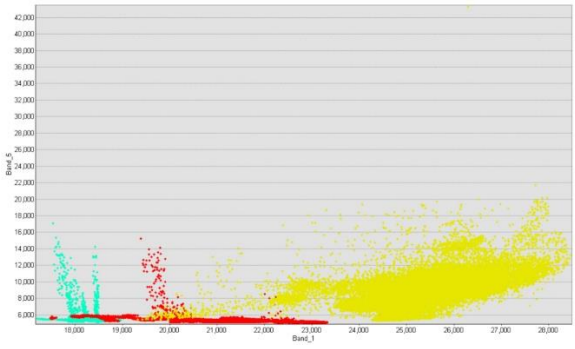

e)

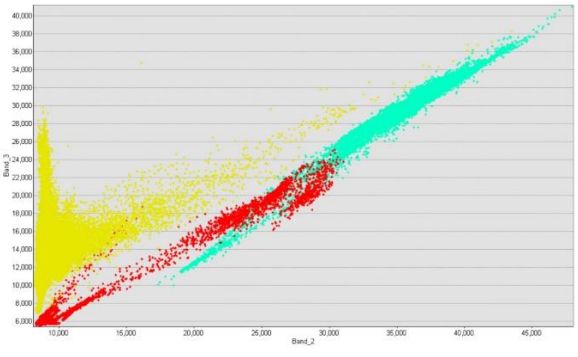

f)

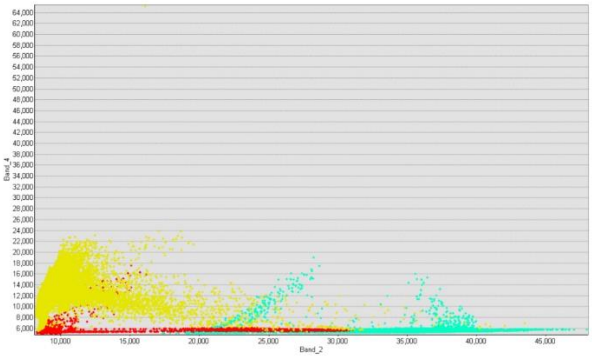

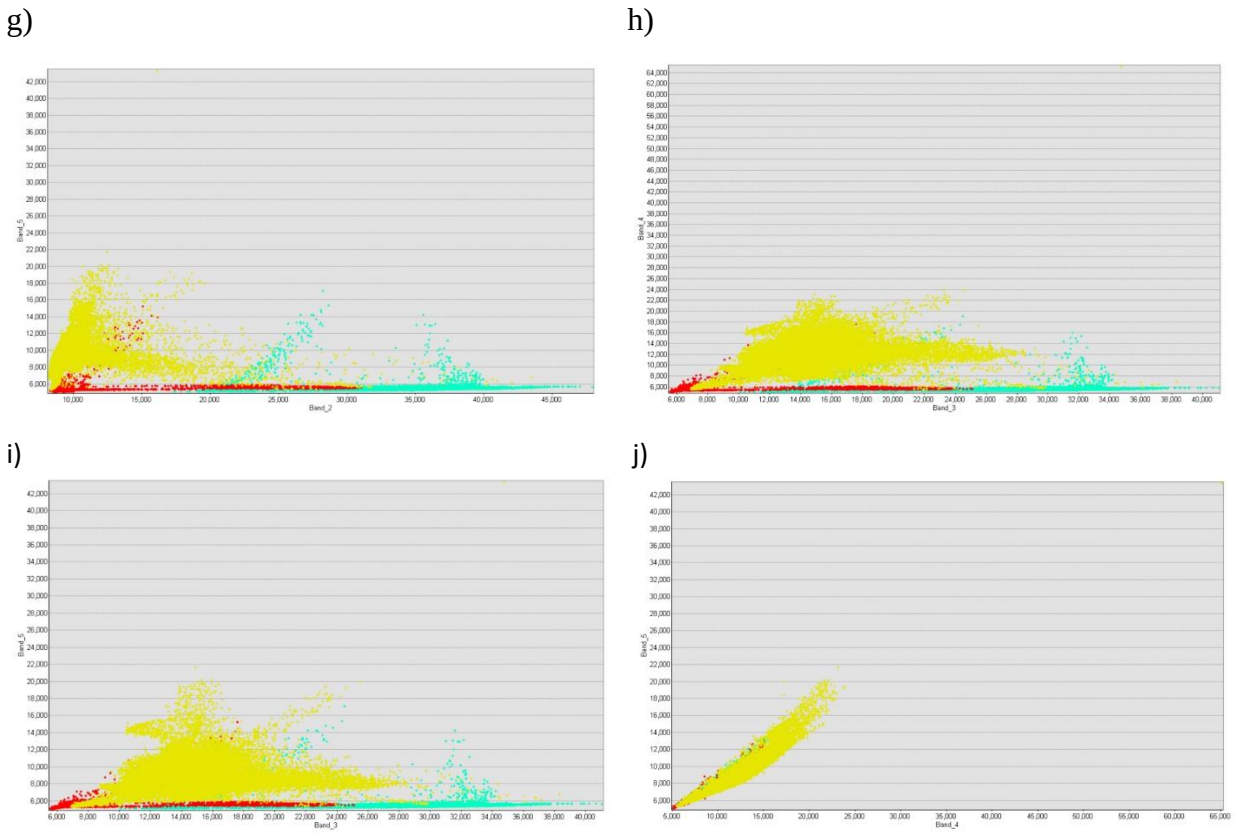

Figure 3.2 Scatterplots of the three classes for the representative area in Jostedalsbreen. Each figure here displays inseparability of classes based on a comparison of two bands. Bands 1-5 in X and Y axes represent blue, NIR, SWIR1, SWIR2, and thermal bands, respectively. Classes in every figure: Yellow: land, red: water bodies, cyan: ice. Landsat-8 image retrieval date: 2018.05.21.

To guide the correct selection of training samples (section 2.5.3), I have carried out a 4-step cross-validation on the representative scene in southern Norway. In this process, MLC was applied with randomly picked three quarters of the training samples, while the accuracy of class recognition was measured on the remaining quarter of the samples. Based on this analysis, the overall accuracy rate was calculated as an average accuracy rate for every sample set, resulting in an overall estimate of the MLC accuracy of 99%.

3.1.2 Elimination of shadow-related misclassifications using Digital Elevation Models

Glacial lakes are often small lakes located in steep terrain areas with complex physical conditions. Hence, the classification of such lakes and proximal slopes might be affected by shadows from their surroundings, leading to their attribution to a wrong surface type. As mentioned in section 2.4.5 in this study, thermal band from Landsat images was adopted to help reduce the shadow effects. The results from composites including thermal band showed improved classification thus the issue of misclassified shadowed slopes as water body was not fully resolved. Previous studies have demonstrated that shadow-related misclassifications can be partly eliminated using DEMs and information on slope parameters (Huggel *et al.*, 2002; Li & Sheng, 2012) - the approach that I have adapted in this study.

Here, 50-meter and 10-meter DEMs are used to produce slope maps and get rid of the shadows that have been misclassified as water bodies. A combination of visual inspection of the existing glacial lake inventories and slope maps has displayed the peculiarity of lake slopes: several glacial lakes in the proximity of glaciers or at the glacier termini appear to have slopes with angles of above 0° and sometimes as high as 14°. Although this finding clashes with the laws of physics, it obviously marks inaccuracies in DEMs that misrepresent the topography in poorly surveyed mountain regions. Surprisingly, the use of a higher resolution DEM instead of its low-resolution predecessor does not lead to any significant improvements: the existence of glacial lakes with surface slope angles of over 0° has been confirmed by both datasets and in the same locations. Table 3.1 summarizes the information on glacial lakes derived from Landsat-8 and Sentinel-2 images in combination with 10- and 50-meter DEMs. Considering insignificant differences in the glacial lake areas recognized when comparing higher- and lower-resolution DEMs (2%), the 50-meter dataset has been selected for the rest of the analyses in this study to minimize the computational time, which increased substantially for the 10-meter DEM.

Table 3.1 Use of two existing DEMs for glacial lake recognition in Landsat-8 and Sentinel-2 images.

Satellite imagery	DEM in use	Glacial lake area (km^2)
Landsat-8 OLI	10-meter	30.90
Landsat-8 OLI	50-meter	31.45
Sentinel-2	10-meter	24.70
Sentinel-2	50-meter	24.45

In their study focusing on glacial lake dynamics, Li and Sheng (2012) used a surface slope angle threshold of ≤10° to define potential glacial lake areas subject to shadows. In contrast, the inspection of the slope maps and glacial lake outlines in this study has revealed that water bodies can be often characterized by up to 14°-surface slope angles, defining the threshold for shadowed glacier lake recognition in my experiments. Figure 3.3 presents instances of existing glacial lakes on surface slopes with angles of above 0°. By applying the range of slope angles below the threshold value (14°), glacial lakes have been separated from shadows and recognized more precisely than when using a slope threshold of 0° that would result in partitioning of single glacial lakes into much smaller segments as well as their partial elimination.

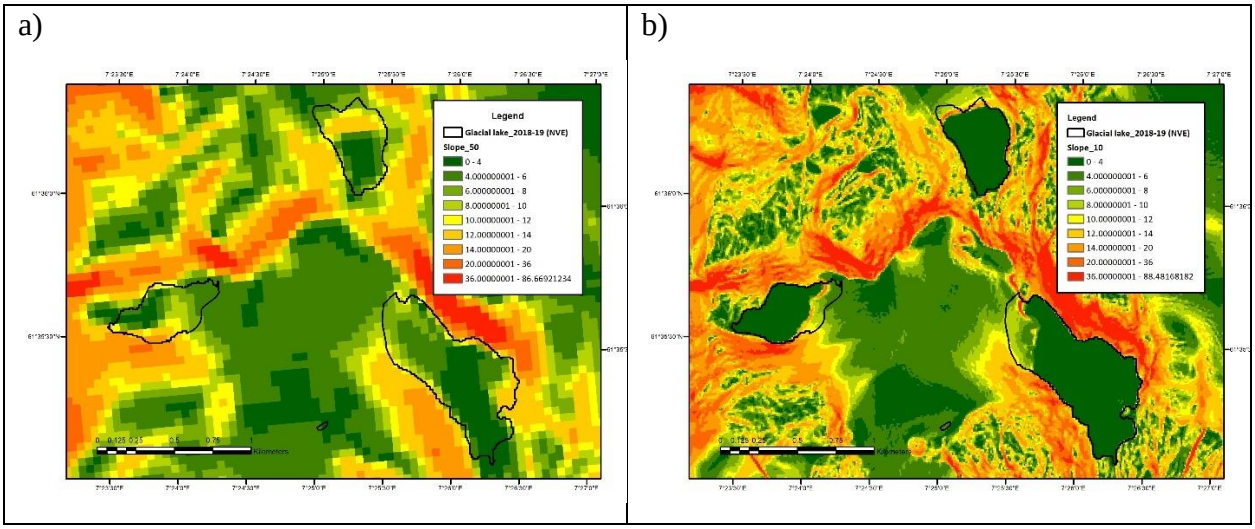

Figure 3.3 Examples of glacial lakes on surface slopes with angles above 0° in a) 50-meter DEM, and b) 10-meter DEM.

3.1.3 Glacier lake statistics in northern versus southern Norway during the period of 1999-2006

Prior to applying MLC, training samples were selected from the two representative scenes in the south and north of Norway following the procedure outlined in Section 3.1.1. A separation of training sample sets into the southern and northern domains has been introduced to avoid issues associated with the differences in imagery properties and climatic settings in the two regions (see figure 2.6). To evaluate the skill of MLC on imagery before and after atmospheric corrections, the classification was repeated in every scene on the corrected and uncorrected sets of imagery. The glacial lake inventory representative of this period (see Section 1.2) was used as a database for the comparison of the MLC-classified lake shapes with the lake outlines derived through semi-automatic (NDWI) and manual mapping in the inventory including 130 and 265 glacial lakes in the north and south, respectively.

Using the signature file from the representative scene covering Østre and Vestre Svartisen, MLC was applied to each satellite imagery pre-selected and retrieved within the northern study domain. Overall, MLC was applied on seven scenes, and the output images were then mosaicked to form the complete northern domain. The next step was to extract the glacial lakes from all recognized water bodies across the mosaic image. Figures 3.4 and 3.5 compare lakes recognized by MLC on non-ACIs (original pre-processed images, see section 2.4.1) and ACIs (images with atmospheric corrections, see Section 2.4.2) with the lakes from the NVE's inventory for 1999-2006 in the area surrounding Vestre and Østre Svartisen. The large lake in the figures, Storglomvatnet, is a regulated glacial lake that serves as a reservoir for the Svartisen hydroelectric power station.

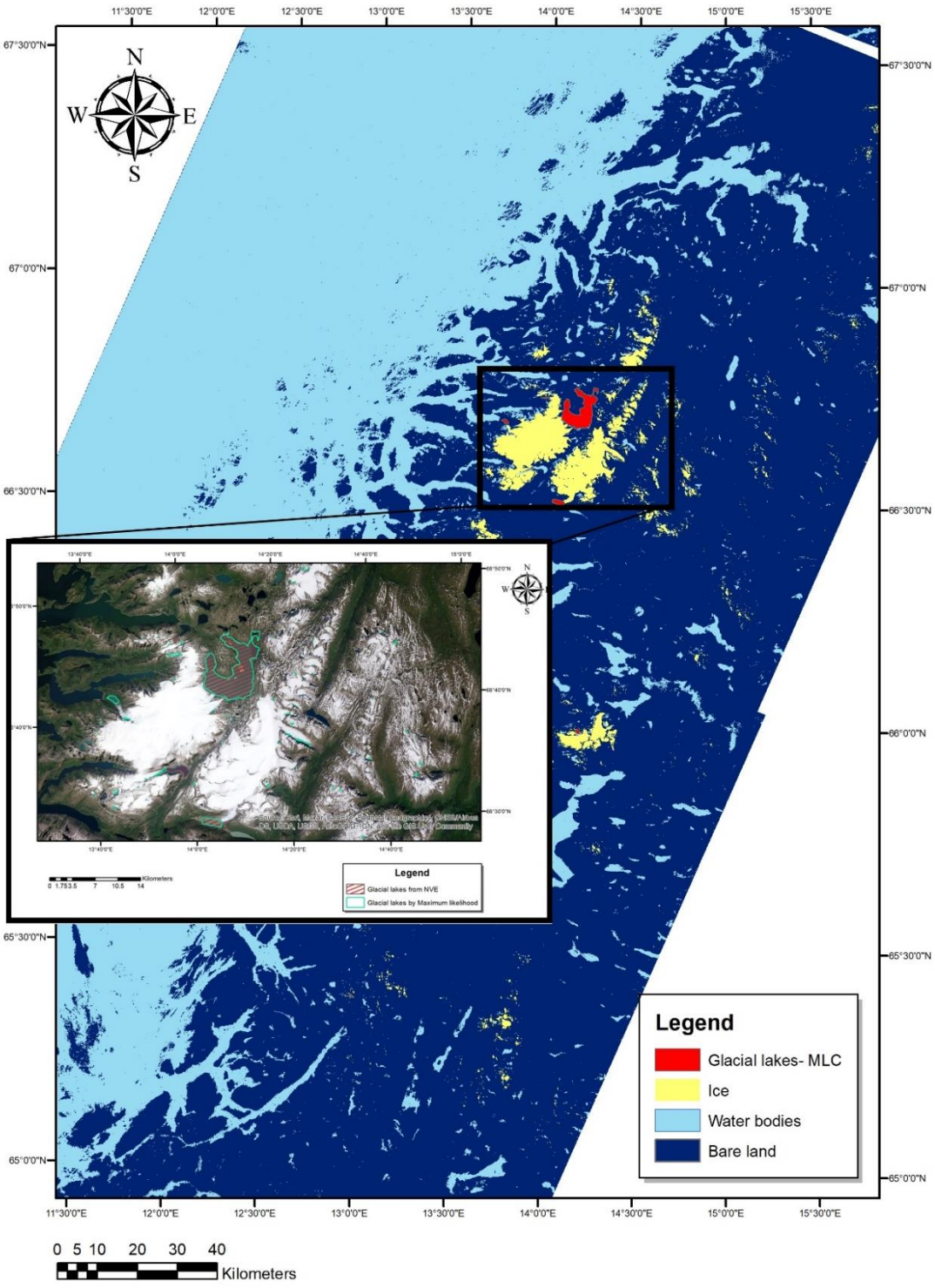

Figure 3.4 Three classes recognized by MLC on non-ACIs for the period of 1999-2006: ice, water bodies and land. The focused area represents Vestre and Østre Svartisen that is the representative scene in northern Norway. Glacial lakes extracted from the water body class are the lakes within the buffer of <100m from glacier outlines of the same year.

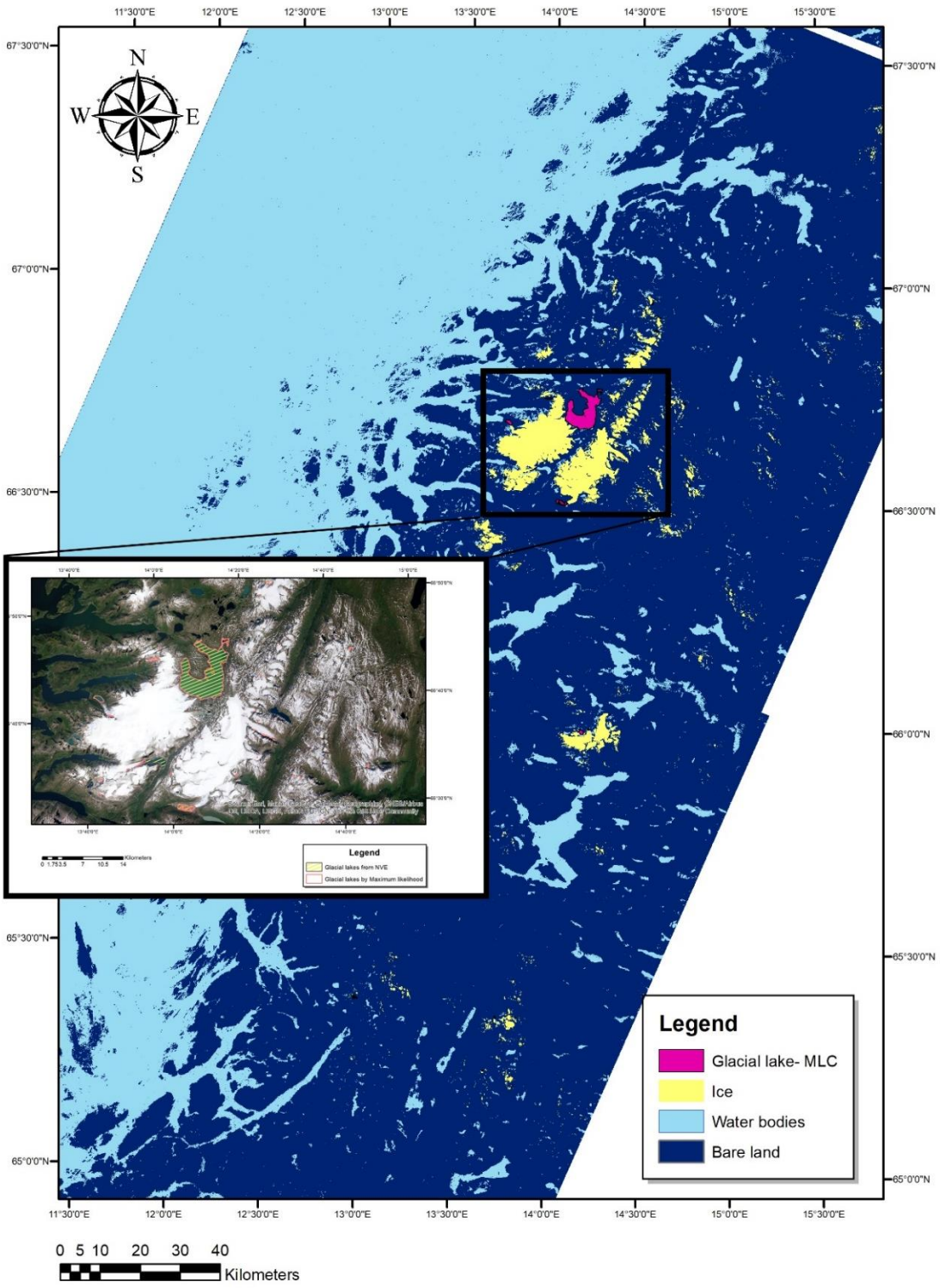

Figure 3.5 Three classes recognized by MLC on ACIs for the period of 1999-2006: ice, water bodies and land. The focused area represents Vestre and Østre Svartisen that is the representative scene in northern Norway. Glacial lakes extracted from the water body class are the lakes within the buffer of <100m from glacier outlines of the same year.

Comparison of the MLC results on non-ACIs and ACIs has revealed 592 polygons of glacial lakes in the non-ACI application and 504 polygons in the ACI application. The former has also produced a much larger area covered by glacial lakes, 85.3 km^2, as opposed to the latter that only identified glacial lakes with a total area of 70.19 km^2 (see Table 3.2). The numbers presented above only include polygons of glacial lakes with sizes larger than 0.001 km^2. Further analysis has identified that of the 504 lake polygons recognized when using ACIs, only 30 were not recognized by the non-ACI application.

Table 3.2 Number and area of glacial lakes in the northern and southern domains based on non-ACIs and ACIs in 1999-2006.

Region	Method and Imagery in use	Number of lakes	Area (km^2)
Northern Norway	MLC on ACI	504	70.19
	MLC on non-ACI	592	85.3
	NVE's inventory	130	80.19
Southern Norway	MLC on ACI	249	39.16
	MLC on non-ACI	384	48.56
	NVE's inventory	265	51.32

In the southern domain, I applied MLC using the signature file from the satellite scene with five tiles covering Jostedalsbreen. As well as for the northern domain, the results of MLC on the mosaicked non-ACIs and ACIs were compared to each other and to the glacial lake inventory (see table 3.2). Figure 3.6 shows lakes recognized by MLC in the Hardangerjøkulen area before and after applying the atmospheric corrections to the imagery.

a)

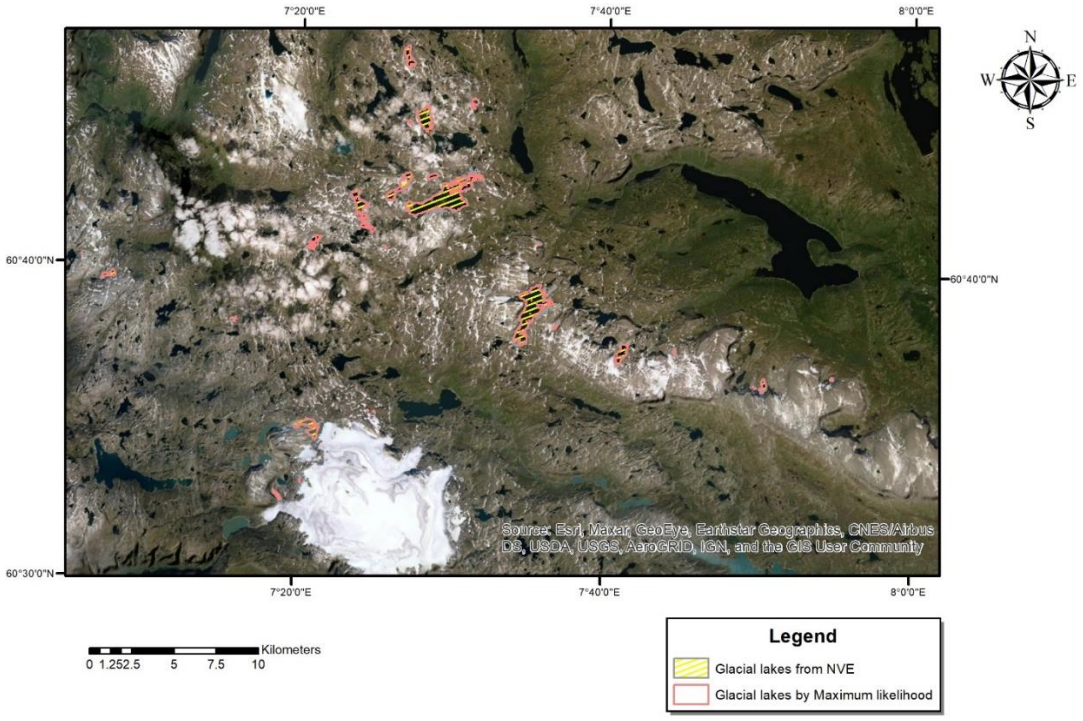

b)

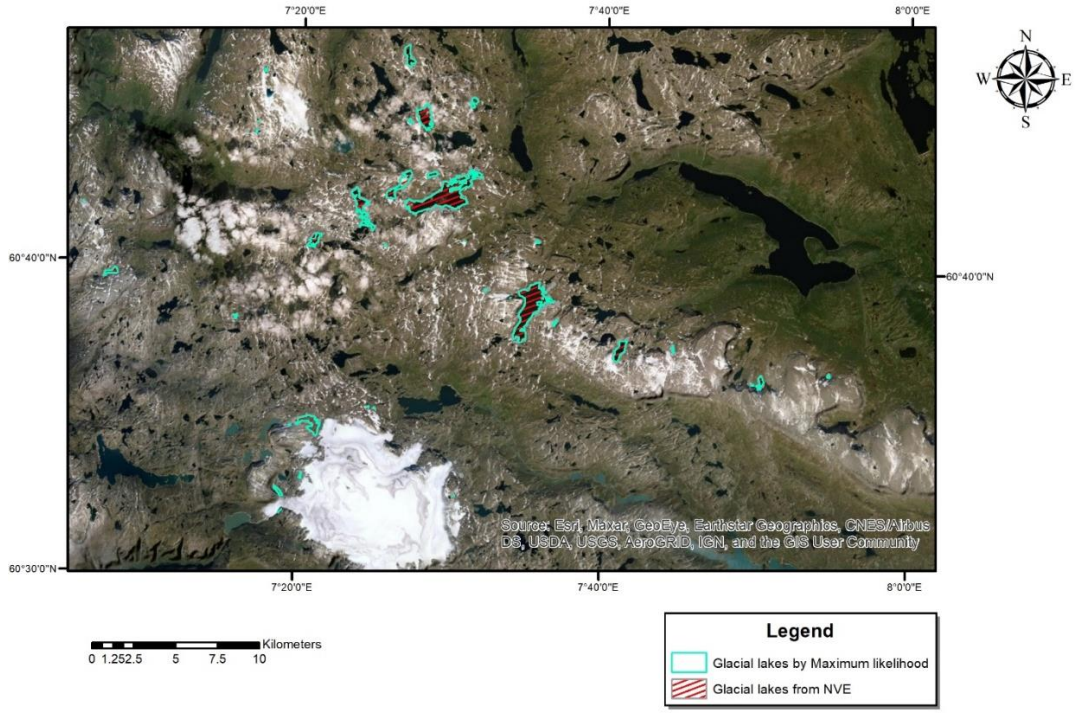

Figure 3.6 Glacial lakes outlined by MLC in Hardangerjøkulen using a) ACIs, and b) non-ACIs for the period of 1999-2006.

There are 384 glacial lakes with a total area of 48.56 km^2 recognized by the application of non-ACIs across the southern domain, in contrast to the ACI classification, where the lake number and total area drop to 249 and 39.16 km^2, respectively. Thus, the non-ACI application produced a higher number of glacial lakes but a smaller lake-covered area compared to 265 lakes with a total area of 51.32 km^2 included in the NVE's inventory. In comparison, the ACI classification resulted in a significant underestimation of both the lake number and area. Further analysis has indicated that only four lake polygons from the ACI classification were not recognized by the classification on non-ACIs.

3.1.4 Glacier lake statistics in southern Norway during the period of 2018-2019

Due to its focus on the most recent period that is covered by Landsat and Sentinel, this section presents a direct comparison of the classification results performed on images from both satellites. Training samples for MLC application on 2018-2019 images have been selected from the scene covering Jostedalsbreen in southern Norway. Since at the time of map production in this study, the NVE's glacier inventory for 2018 was incomplete and only contained areas from southern Norway, I had to limit the MLC application domain to the satellite images from the area where glacier outlines were available. Here again I performed classification on both ACIs and non-ACIs from Landsat and compared their relative performance. Given the observations of poor performance of ACIs described in this and previous sections, atmospheric corrections have not been applied to the Sentinel images.

The new NVE's glacial lake inventory includes 321 lakes, which are only partially captured by MLC on both ACIs and non-ACIs. In total, MLC has succeeded to identify 168 and 273 polygons with glacial lakes from ACIs and non-ACIs, respectively (see table 3.3). About half of all the lakes recognized by the ACI application are overlapping with lakes classified using non-ACIs. The lake number and total area extracted from non-ACIs are comparable to the those estimated in the NVE's inventory, in contrast to the classification on ACIs that drastically underestimates both quantities.

Table 3.3 Number and area of glacial lakes in the southern domain based on ACIs and non-ACIs in 2018-2019.

Method	Number of lakes	Area (km^2)
MLC by ACI	168	23.22
MLC by non-ACI	273	31.45
MLC on Sentinel-2 images	189	24.45
NVE's inventory	321	35.13

Although I have tried to keep the design of MLC applications on both Landsat and Sentinel-2 images consistent, some adjustments had to be made with respect to the selection of training samples from the Sentinel dataset (see table 2.1 for the information on the images). After having evaluated the correctness of training samples from the image covering the representative Jostedalsbreen area that were used in the Landsat classification, they were transferred for the use on Sentinel-2 images. However, Sentinel-2 images are available for download in tiles of 100x100 km, which are different from the Landsat dataset. Hence, the training samples that fell outside the scene were omitted and replaced by new samples to cover the entire image. The training samples separability was again assessed using scatterplots for the three defined classes (see section 3.1.1 for details), albeit with different band combinations (excluding the thermal band). Based on the scatterplot analysis, blue-SWIR1, NIR-SWIR1, and SWIR1-SWIR2 band pairs showed a good recognition potential for all three classes.

Following corrections for the misclassified shadowed slopes (see Section 3.1.2), a total of 189 lakes was recognized, covering a sum area of 24.45 km^2. Performance of MLC on the Sentinel images is therefore deemed less accurate compared to Landsat non-ACIs, resulting in an underestimation of >40% in the lake number and ~30% in the lake-covered area. Several recognized glacial lakes from Sentinel-2 and Landsat-8 OLI images were well-paired. However, in some cases, the classification using only one of the two imagery sets was able to recognize some glacial lakes, while missing them when the other set was used as input. Figure 3.7 zooms into some of the well-paired lakes recognized by MCL on both sets of imagery.

a)

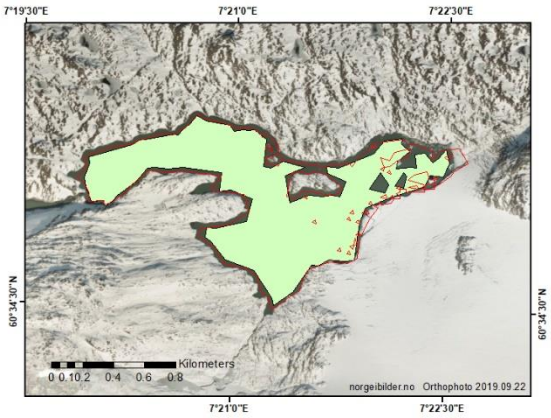
7°19'30"E
7°21'0"E
7°22'30"E
60°34'30"N
Kilometers
0 0.1 0.2 0.4 0.6 0.8
norgeibilder.no Orthophoto 2019.09.22

b)

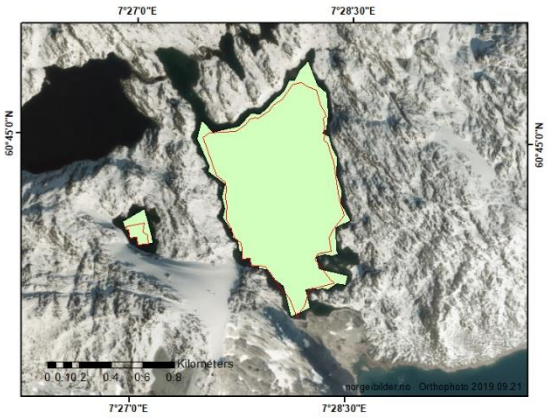
7°27'0"E
7°28'30"E
60°45'0"N
Kilometers
0 0.1 0.2 0.4 0.6 0.8
norgeibilder.no Orthophoto 2019.09.21

c)

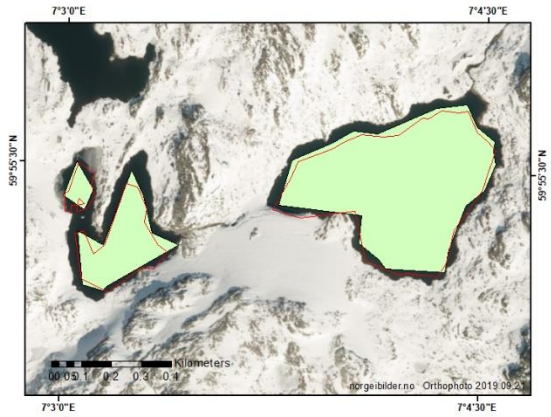
7°3'0"E
7°4'30"E
59°55'30"N
Kilometers
norgeibilder.no Orthophoto 2019.09.21

d)

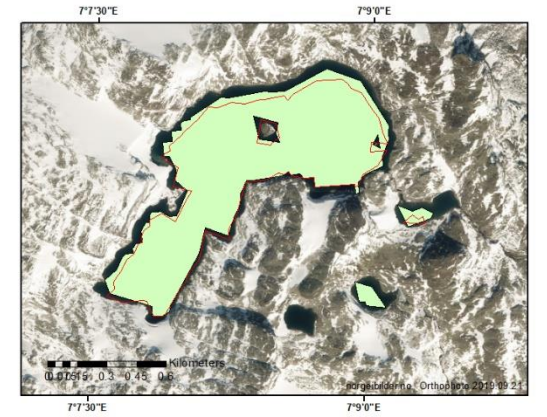
7°7'30"E
7°9'0"E
Kilometers
norgeibilder.no Orthophoto 2019.09.21

e)

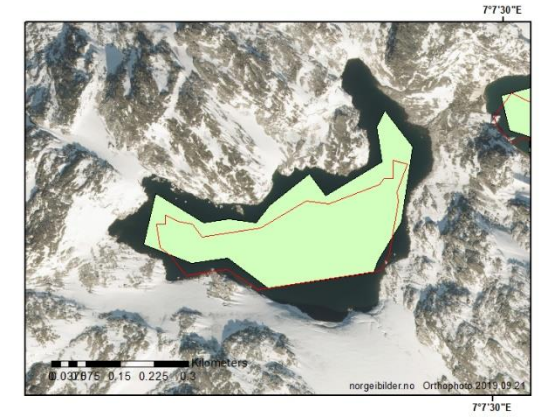
7°7'30"E
Kilometers
0 0.075 0.15 0.225 0.3
norgeibilder.no Orthophoto 2019.09.21

f)

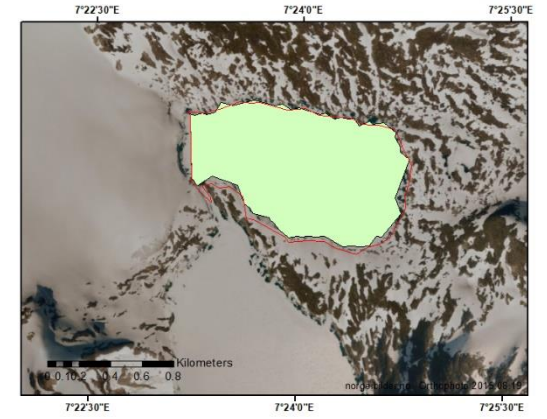
7°22'30"E
7°24'0"E
7°25'30"E
Kilometers
0 0.1 0.2 0.4 0.6 0.8

g) h)

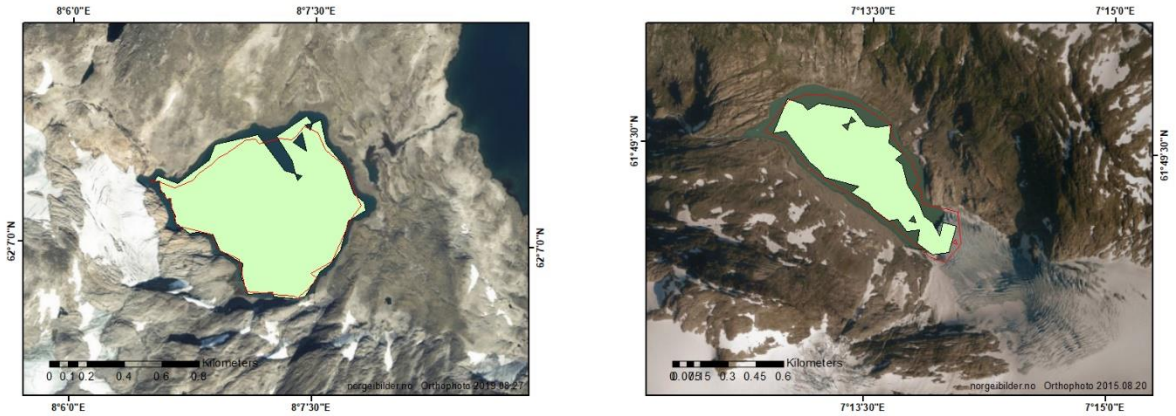

Figure 3.7 Instances of glacial lakes recognized by MLC applied on Landsat-8 OLI and Sentinel-2 images from 2018-2019 in southern Norway. The red outlines and green polygons belong to application of method on Sentinel and Landsat images, respectively.

3.1.5 Glacier lake statistics in northern versus southern Norway during the period of 1988-1997

NVE's database contains another glacier inventory spanning the period between 1988 and 1997, which can be used in this study to track the evolution of glacial lakes through a longer time interval. Training samples were selected in the two representative areas as discussed previously: the Jostedalsbreen region in the south and Østre and Vestre Svartisen region in the north. Since applying FLAASH as a module for the atmospheric corrections on the imagery from Landsat 4-5 was not recommended, the analysis presented here has focused entirely on non-ACIs, which does not appear problematic due to a generally poor performance of MLC on ACIs as demonstrated in the previous sections.

Similarly, to the classification in Section 3.1.3, MLC was applied on seven scenes, covering all glacial areas in the north. 1085 polygons of water body have been separated as glacial lakes, with the overall lake area of 58.33 km^2 (table 3.4). This is contrasting the numbers provided in the NVE's glacial lake inventory for the same period, where only 91 glacial lakes covering a total area of 47.41 km^2 were identified within the northern domain. Figure 3.8 presents glacial lake

outlines recognized by MLC on non-ACIs from the oldest historical period analyzed in this study.

Table 3.4 Number and area of glacial lakes in northern and southern domains based on different methods in 1988-1997.

Region	Method and Imagery in use	Number of lakes	Area (km^2)
Northern Norway	MLC on non-ACI	1058	58.33
	NVE's inventory	91	47.41
Southern Norway	MLC on non-ACI	1182	39.49
	NVE's inventory	102	23.34

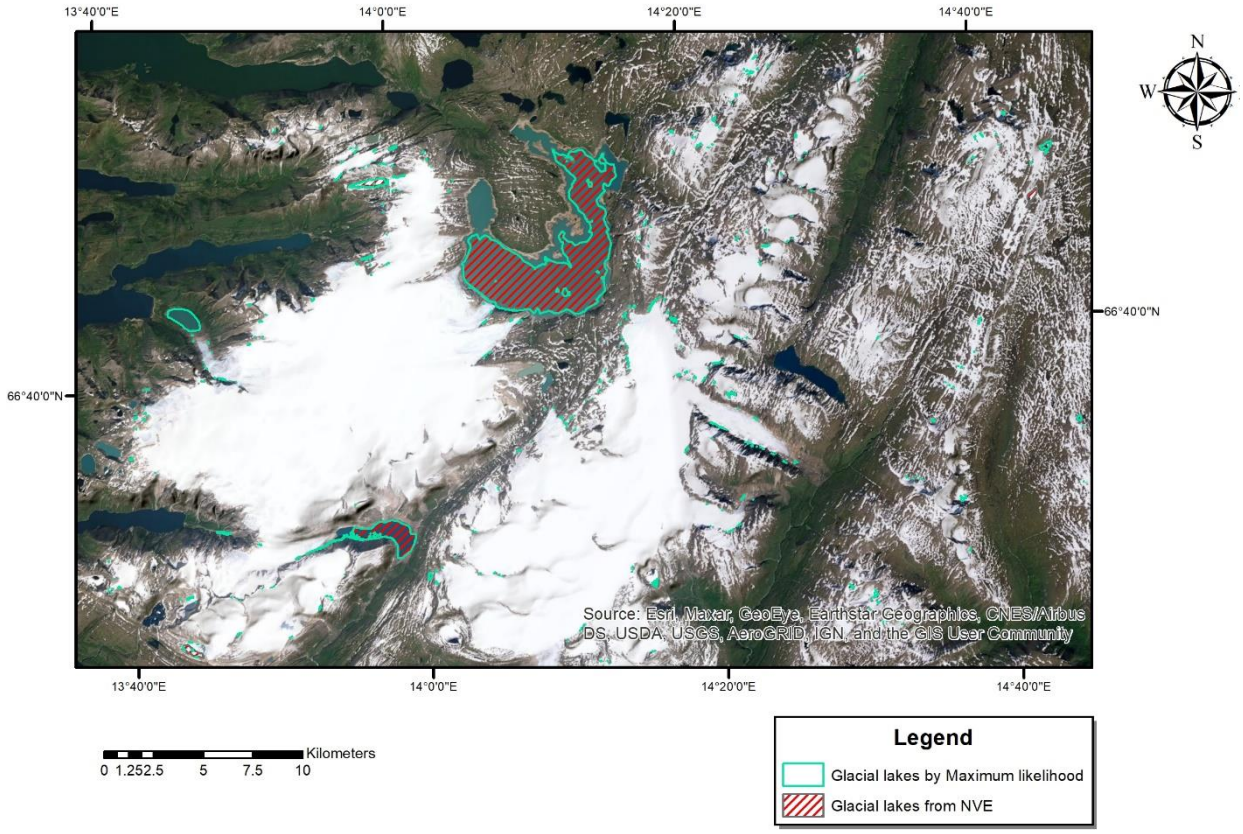

Figure 3.8 Glacial lakes outlined using MLC on non-ACIs in northern Norway in the period of 1988-1997.

In the south, the NVE's glacier inventory is missing the glacier outlines from the Jostedalsbreen area that has been excluded from the evaluation of the classification results in the southern domain. Only three satellite images were pre-selected and mosaicked to cover all glaciated areas

in the south. Figure 3.9 depicts glacial lake outlines recognized by MCL on non-ACIs in the sample area in southern Norway. The number and area of the recognized glacial lakes are 1182 and 39.49 km^2, respectively, which is again difficult to compare with the statistics provided by the NVE's inventory including 102 lakes with a total area of 23.34 km^2 (table 3.4). Both in the north and south, MLC has produced a ten-fold number of glacial lakes compared to the NVE inventory and overestimated their total areas by 23% in the north and nearly 70% in the south.

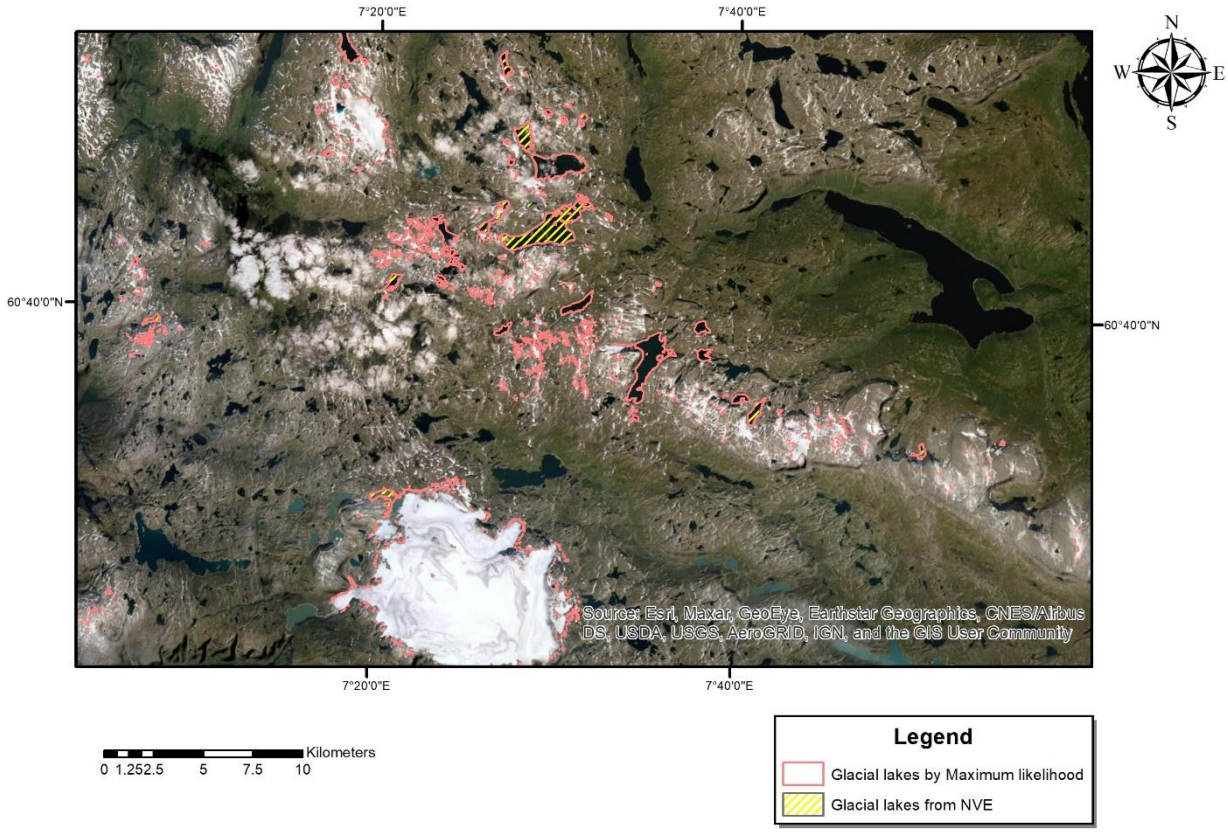

Figure 3.9 Glacial lakes outlined using MLC on non-ACIs in southern Norway in the period of 1988-1997.

3.1.1 Comparison of Maximum Likelihood Classification results in ArcGIS and ENVI – method validation stage

Since the Support Vector Machine (SVM) classification has not been implemented in ArcGIS, I have opted for testing it using another software, ENVI (see Section 2.5.4). It has been a

necessary step however to evaluate to which extent the results of identical classification methods diverge in the two types of software implemented by different developers – ENVI and ArcGIS – to enable a clean comparison of their classification skills. Since ENVI also includes MLC, I have compared its results to those obtained with MLC in ArcGIS. The scene selected for this comparison covering the representative scene over the Jostedalsbreen area with Landsat image (non-ACIs) for the period of 2018-2019 (Landsat-8, 2018.06.29, path/row: 201/017), which is identical to that in section 3.1.4. Naturally, MLC tests with ENVI have also been performed with exactly the same training samples (named as Region Of Interest in ENVI, see section 2.5.3). Similar to MLC in ArcGIS, I have not imposed any thresholds on pixel classification, and as a result, the MLC outcomes in ArcGIS and ENVI were visually inseparable. However, quantitative analyses of the results have indicated that MLC in ENVI classified 128,004 more pixels as ice compared to ArcGIS. Consequently, 4,518 less pixels were assigned the water class and 123,486 less pixels– the land class. Regardless, the classification accuracy rate was very similar to the MLC applications in ArcGIS, and the overall difference in pixel class counts was 0.13%. Therefore, it has been concluded that both ENVI and ArcGIS display comparable performance and do not show drastic differences in the classification results, giving credit to the transferability of general conclusions based on the MLC results in ArcGIS and SVM/MLC results in ENVI.

3.2 Application of Support Vector Machine as the second method

- Base for comparison

In this section results from the application of SVM are presented to enable a comparison of its performance with that of MLC. As a pre-requisite for application of any supervised method, selection of training samples is the first necessary step. As mentioned in section 2.5.2.3, by using ENVI for application of SVM, ROIs cannot generate a signature file to enable the use in a larger area. Therefore, SVM is applied on Landsat-8 and Sentinel-2 images covering the representative scene of Jostedalsbreen retrieved in 2018.06.29 and 2018.07.26, respectively.

3.2.1 Selection of training samples for Support Vector Machine in separation of land classes

For application of SVM in this study, to keep the consistency, the same training samples that were selected for performing MLC were imported into ENVI to form the Region Of Interest (ROI). ROI is the substitute name that ENVI uses for the training samples from MLC in ArcGIS, and to keep it corresponding to the program, I also use ROIs in this work.

As mentioned in 3.1.4, since Sentinel and Landsat images have difference in their size and coverage area, the ROIs from Landsat were not completely covering Sentinel image. Due to inequality in the number of training samples in Sentinel-2 and Landsat-8, I added new ROIs to the Sentinel-2 image.

To assess the spectral separability between the selected ROIs for the image in use, the ROI separability tool in ENVI was used. The tool reports the separability by both Jeffries-Matusita and Transformed Divergence measures. The reported values could vary between 0 to 2, indicating how well separable the ROI pairs are. Closer values to 2 imply better separability of ROI pairs. In case the ROI pairs mark a low value (less than 1), it is suggested to combine them into a single ROI (Geospatial, 2010). In this study, the ROI separability report indicated very good separability as the training sets had values of 1.99, 1.99 and 2.0 for pairs of ice-land, water bodies-land and ice-water bodies, respectively for Landsat 8 and Sentinel 2 images (table 3.5).

Table 3.5 ROI separability report where records 1, 2 and 3 were ice, water bodies and land, respectively. The ROIs belong to the Landsat-8 image retrieved on 2018.06.29 and Sentinel-2 image retrieved on 2018.07.26.

Landsat-8	Input File: Composite_LC08_L1TP_201017_20180629_20180716_01_band10 ROI Name: (Jeffries-Matusita, Transformed Divergence)
	trainingfromgis [RECORD=1]: trainingfromgis [RECORD=2]: (2.00000000 2.00000000) trainingfromgis [RECORD=3]: (1.99609303 2.00000000)
	trainingfromgis [RECORD=2]: trainingfromgis [RECORD=1]: (2.00000000 2.00000000) trainingfromgis [RECORD=3]: (1.99997736 2.00000000)
	trainingfromgis [RECORD=3]: trainingfromgis [RECORD=1]: (1.99609303 2.00000000) trainingfromgis [RECORD=2]: (1.99997736 2.00000000)
	Pair Separation (least to most); trainingfromgis [RECORD=1] and trainingfromgis [RECORD=3] - 1.99609303 trainingfromgis [RECORD=2] and trainingfromgis [RECORD=3] - 1.99997736 trainingfromgis [RECORD=1] and trainingfromgis [RECORD=2] - 2.00000000
Sentinel-2	Input File: STACK_S2A_MSIL1C_20180726T110621_N0206_R137_T32VLP_20180726T113410 ROI Name: (Jeffries-Matusita, Transformed Divergence)
	Training_SENTINEL [RECORD=1]: Training_SENTINEL [RECORD=2]: (2.00000000 2.00000000) Training_SENTINEL [RECORD=3]: (1.99999999 2.00000000)
	Training_SENTINEL [RECORD=2]: Training_SENTINEL [RECORD=1]: (2.00000000 2.00000000) Training_SENTINEL [RECORD=3]: (1.99987663 2.00000000)
	Training_SENTINEL [RECORD=3]: Training_SENTINEL [RECORD=1]: (1.99999999 2.00000000) Training_SENTINEL [RECORD=2]: (1.99987663 2.00000000)
	Pair Separation (least to most): Training_SENTINEL [RECORD=2] and Training_SENTINEL [RECORD=3] - 1.99987663 Training_SENTINEL [RECORD=1] and Training_SENTINEL [RECORD=3] - 1.99999999 Training_SENTINEL [RECORD=1] and Training_SENTINEL [RECORD=2] - 2.00000000

3.2.2 Application of Support Vector Machine

In application of SVM, selecting the right gamma and penalty values in the kernel function are important since gamma defines the margin between the hyperplane and the support vectors that are the data points nearest to the hyperplane. This defines the influence of a single training sample. At the same time, penalty is the value that allows an error in drawing the margin and controls the compensation of rigid margins. A higher penalty value allows more error in the training samples, therefore, possibility of misclassification. The default gamma and penalty value in ENVI are the inverse number of bands (in this study 0.2 for Landsat-8 using 5 bands and 0.25 for Sentinel-2 image with 4 bands) and 100, respectively. But cross validation is usually performed to identify the best gamma-penalty values. In this study a 4-fold cross validation was performed. The classification was performed four times, and each time one fourth of the training samples were used for validation. The average accuracy rate was calculated afterwards. Three different gamma values of 0.14, 0.2 and 0.3 for Landsat image and 0.3, 0.25 and 0.16 for the Sentinel image were chosen to try for two penalty values of 100 and 200. By change of the gamma value, no difference was recognized in the classes when penalties of 100 and 200 were applied separately. The overall accuracy by performing the cross validation was 95.75% and 94.25% for Landsat and Sentinel, respectively.

Even though the result of accuracy test showed no difference between applying the penalty of 100 and 200, visual inspection of the classified image showed that by selection of penalty value of 200, more pixels were misclassified as ice and water in the Landsat image and more pixels of land were misclassified as water bodies in the Sentinel image. So, in this study, the final choice was gamma-penalty value of 0.2-100 and 0.25-100 for Landsat and Sentinel images, respectively.

3.3 Recognition potential : Maximum Likelihood vs Support Vector Machine

The next step after application of SVM on Sentinel-2 and Landsat-8 images is the comparison and evaluation of glacial lakes outlined by this method and MLC. The homogeneous extraction method of glacial lakes in SVM and MLC on the two satellite imagery in use allows a fine

comparison of the methods applied. Although both methods show good potential for glacial lake recognition, in both Sentinel and Landsat images, more glacial lakes were recognized by the SVM method. Table 3.6 summarizes the lakes' details.

In the scene used from Landsat-8, glacial lakes recognized by SVM covered 20.20 km^2 of area in total, while MLC and NVE's inventories covered 13.83 and 21.21 $km^{2,}$ respectively. In the image, SVM overestimates the number of recognized lakes while MLC showed significant underestimation to less than one third. This is while in the used Sentinel-2 scene, SVM presented a closer number and area of glacial lakes in total with 59 and 2.85 km^2. Still, MLC produced a larger difference in glacial lake outlining by delineating only 38 lakes with a total area of 1.82 km^2. As well as the number and sum of the glacial lakes' area, SVM recognizes glacial lake outlines closer to the outline in NVE's inventory (Images a-l in figure 3.10).

Table 3.6 Number and area of recognized glacial lakes based on every method on Landsat-8 OLI and Sentinel-2 images.

Satellite image	Classification method	Number of glacial lakes	Area (km^2)	
Landsat-8 OLI	MLC	46	Sum	13.83
			Smallest	0.0018
			Largest	6.18
	SVM	241	Sum	20.20
			Smallest	0.00101
			Largest	6.7
	NVE's inventory	152	Sum	21.21
			Smallest	0.0011
			Largest	7.39
Sentinel-2	MLC	38	Sum	1.82
			Smallest	0.0012
			Largest	0.46
	SVM	59	Sum	2.85
			Smallest	0.0012
			Largest	0.49
	NVE's inventory	63	Sum	2.98
			Smallest	0.0011
			Largest	0.48

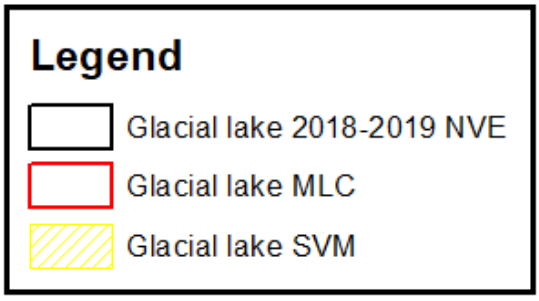
Legend
Glacial lake 2018-2019 NVE
Glacial lake MLC
Glacial lake SVM

a)

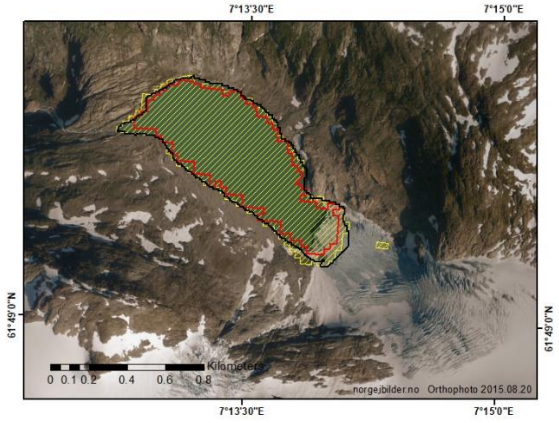
7°13'30"E
7°15'0"E
61°49'0"N
Kilometers
0 0.1 0.2 0.4 0.6 0.8
norgeibilder.no Orthophoto 2015.08.20

b)

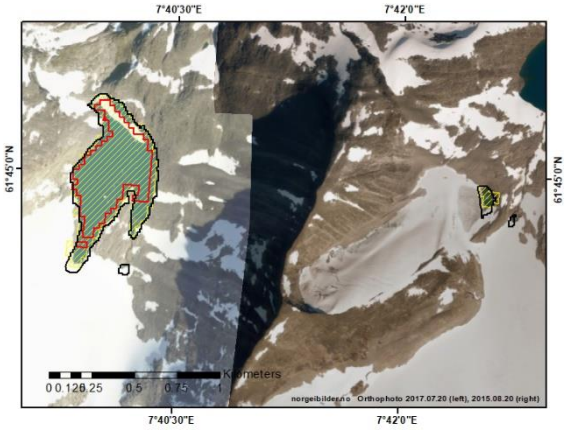
7°40'30"E
7°42'0"E
61°45'0"N
Kilometers
0 0.125 0.25 0.5 0.75 1
norgeibilder.no Orthophoto 2017.07.20 (left), 2015.08.20 (right)

c)

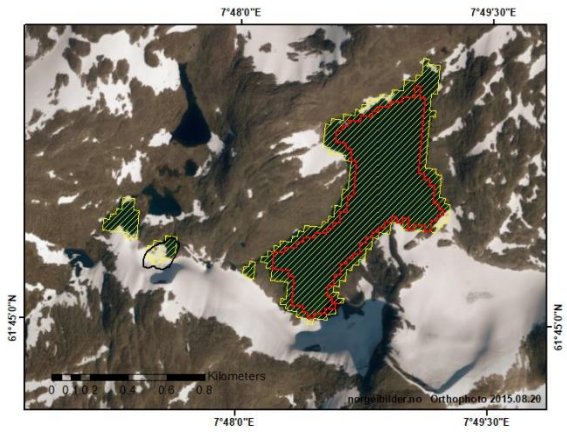
7°48'0"E
7°49'30"E
61°45'0"N
Kilometers
0 0.1 0.2 0.4 0.6 0.8
norgeibilder.no Orthophoto 2015.08.20

d)

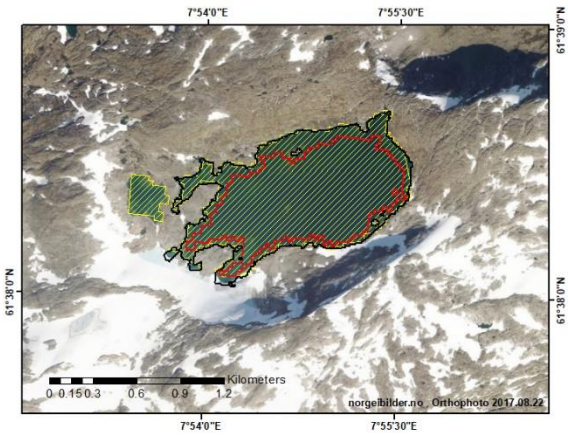
7°54'0"E
7°55'30"E
61°38'0"N
Kilometers
0 0.15 0.3 0.6 0.9 1.2
norgeibilder.no Orthophoto 2017.08.22

e)

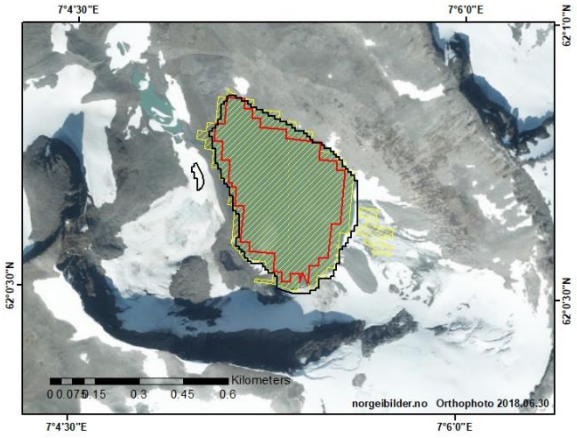
7°4'30"E
7°6'0"E
62°1'0"N
62°0'30"N
Kilometers
0 0.075 0.15 0.3 0.45 0.6
norgeibilder.no Orthophoto 2018.06.30

f)

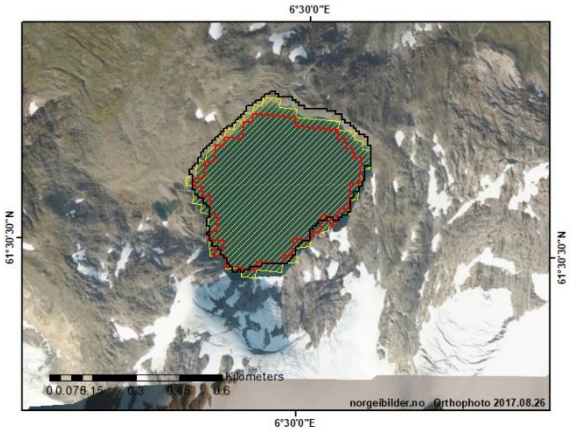
6°30'0"E
61°30'30"N
61°30'0"N
Kilometers
0 0.075 0.15 0.3 0.45 0.6
norgeibilder.no Orthophoto 2017.08.26

g)

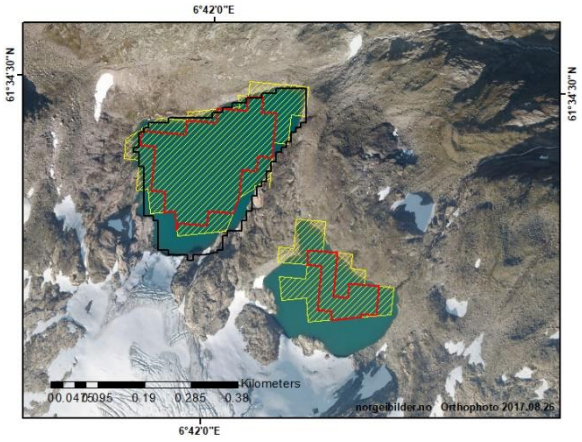
6°42'0"E
61°34'30"N
Kilometers
0 0.0475 0.095 0.19 0.285 0.38
norgeibilder.no Orthophoto 2017.08.26

h)

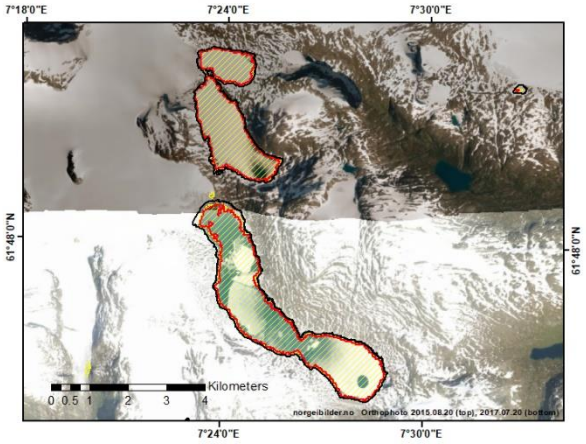
7°18'0"E
7°24'0"E
7°30'0"E
61°48'0"N
Kilometers
0 0.5 1 2 3 4
norgeibilder.no Orthophoto 2015.08.20 (top), 2017.07.20 (bottom)

i)

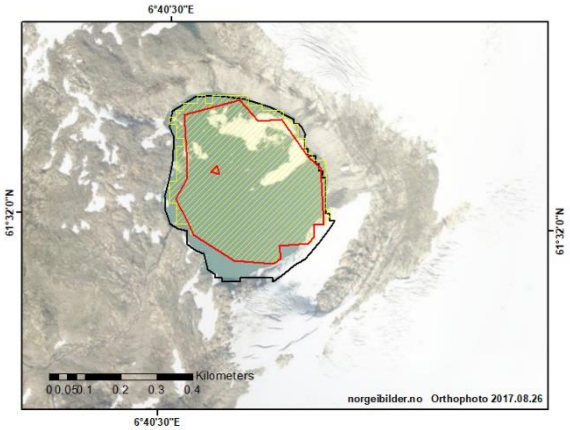
6°40'30"E
61°32'0"N
Kilometers
0 0.05 0.1 0.2 0.3 0.4
norgeibilder.no Orthophoto 2017.08.26

j)

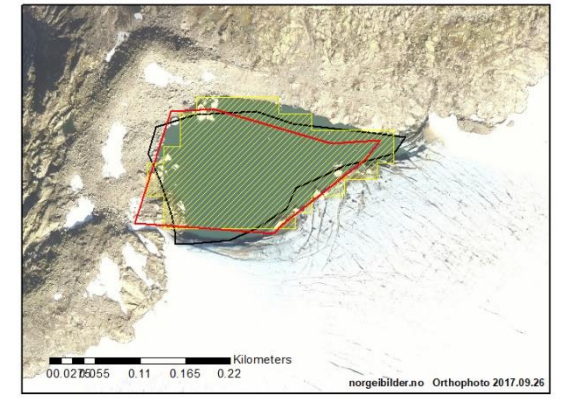
Kilometers
0 0.0275 0.055 0.11 0.165 0.22
norgeibilder.no Orthophoto 2017.09.26

k) l)

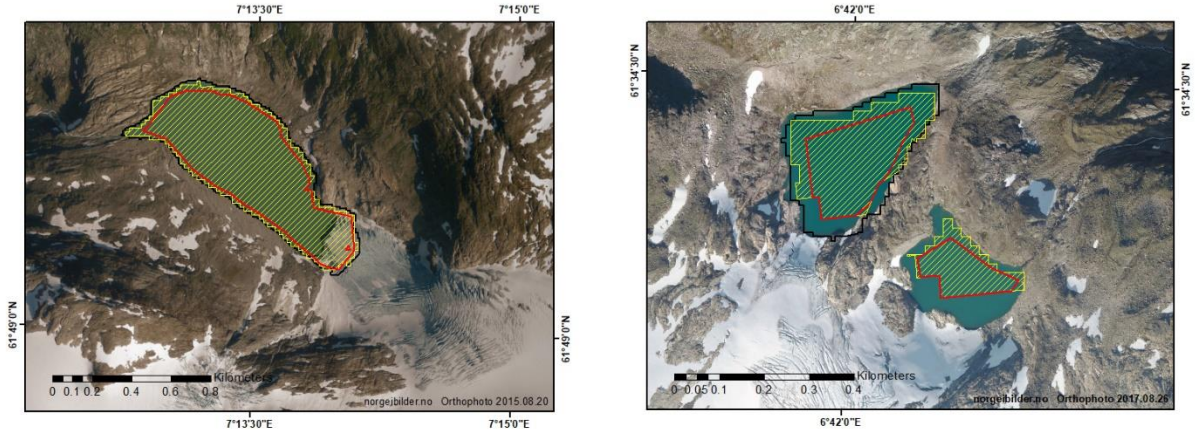

Figure 3.10 (a-h) Glacial lake outlines from MLC, SVM, and NVE's inventory in 2018-19 on Landsat-8 OLI scene retrieved in 2018.06.29- path/row: 201/017. (i-l) Glacial lake outlines from MLC, SVM, and NVE's inventory in 2018-19 on Sentinel-2 scene retrieved in 2018.07.26, tile number: T32VLP.

3.4 Comparison of glacial lake outlines

As classification models, MLC and SVM separate every pixel of satellite images into classes that are defined for them through the training samples. The pixel by pixel allocation of classes leads to a pixelized display of classified image. Figure 3.11-a presents an example of a glacial lake surrounded by ice and land as they appear in the final classified image produced by either of the methods applied in this study.

As a step in glacial lake extraction (see section 2.6), the layer produced by the methods would change into a polygon layer dividing the water body class from the rest. During the process of extracting water bodies, ArcGIS simplifies polygons to smooth them into simpler shapes. With the smoothing process, polygons are drawn as close as possible to the original shape while containing a minimum number of segments. The simplified lake area is displayed in figure 3.11-b. The size of the pixels is obviously based on the original satellite image pixel size which in this study is 30*30 meters for Landsat and 20*20 meters for Sentinel-2 images.

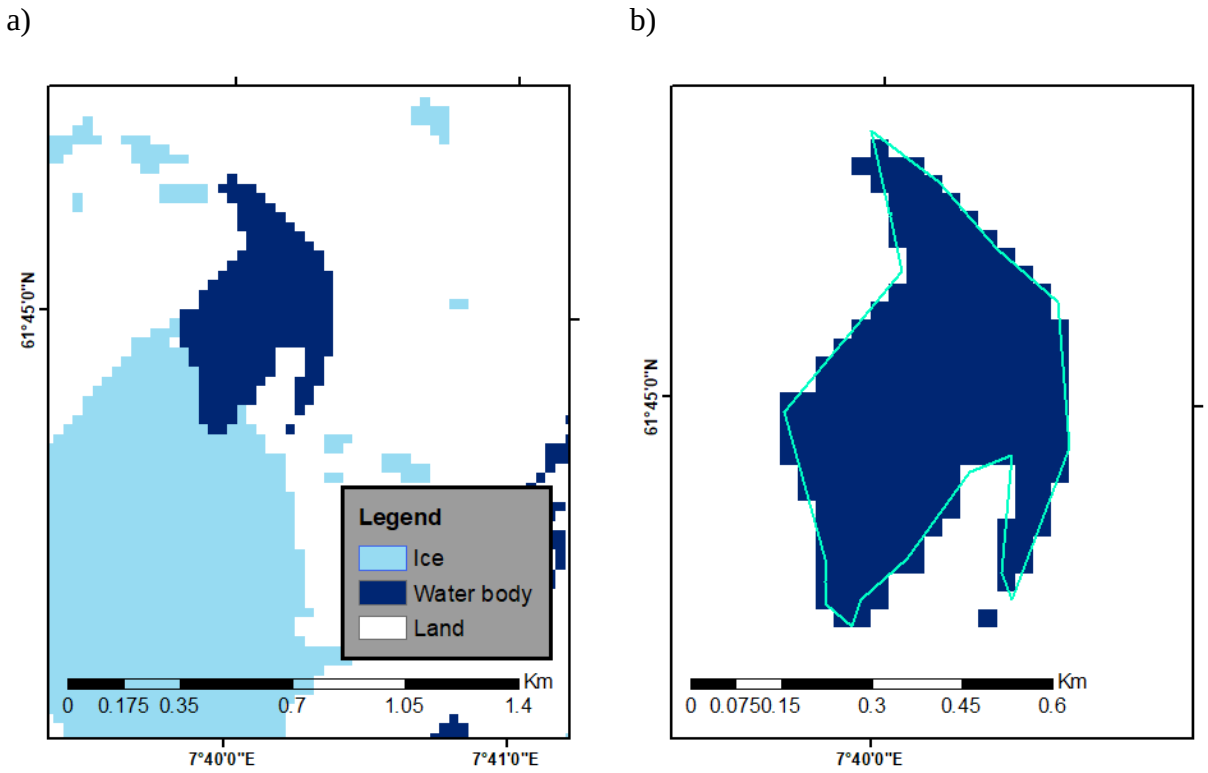

Figure 3.11 a) Pixel by pixel maximum likelihood classes display. b) Simplified outline of the glacial lake based on the pixelized class produced by MLC. The MLC belongs to the period of 1999-2006 and is based on the Landsat-7 image retrieved in 2004.08.10.

As mentioned, pixel size of satellite images differs due to their spatial resolution. Figure 3.12 displays visual differences of image overview in Landsat 8 and Sentinel 2 as satellite images used in this study, orthophoto and N50 topographical map. The images show the glacial lake neighbouring Erdalsbreen in Jostedalsbreen area.

As visible from the images, the lake has developed since 2015 when the orthophoto was taken and N50 topographic map was produced. Therefore, although higher resolution of orthophotos makes them a potential comparison base, the produced outlines from MLC and SVM must be from a close time period to the orthophotos to enable precise comparison. In this study, unless existence of a glacial lake was of question, orthophotos were only used for display reasons. The comparison of MLC and SVM in recognition of the glacial lake on different satellite images (figure 3.12-e and f) is further discussed in section 4.3.

a)

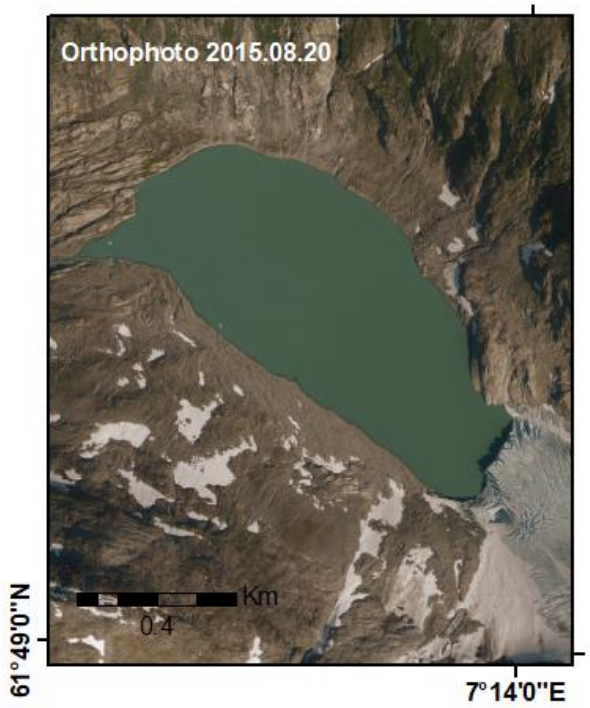
Orthophoto 2015.08.20
Km
0.4
61°49'0"N
7°14'0"E

b)

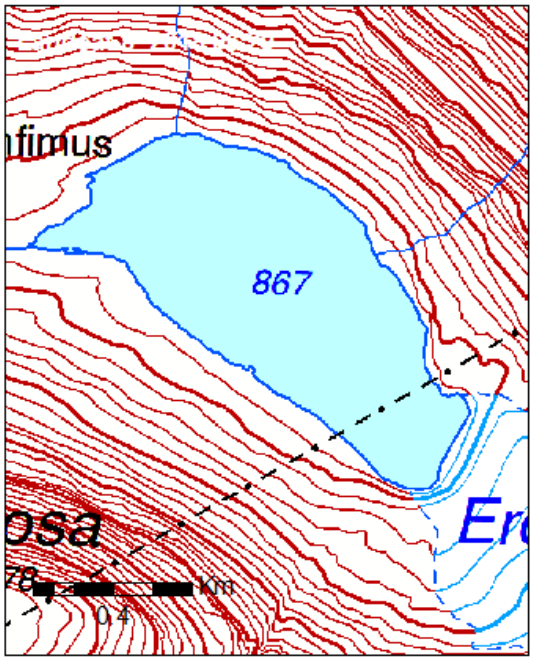
867
Km
0.4

c)


Sentinel-2 2018.07.26
Kilometer
0.4

d)

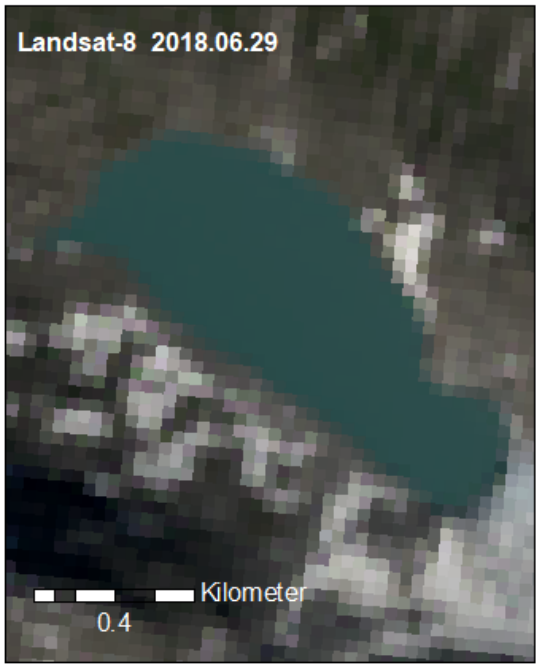
Landsat-8 2018.06.29
Kilometer
0.4

e) f)

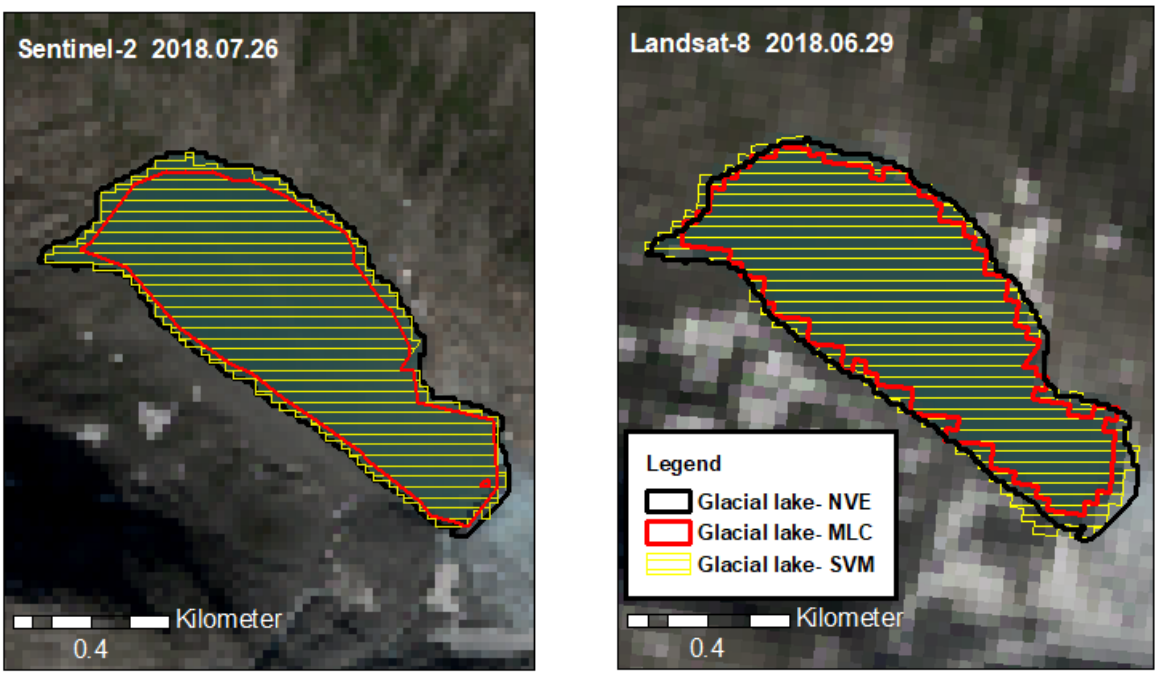

Figure 3.12 Comparison of different imagery and topographic map in presenting a glacial lake. The lake is located by Erdalsbreen in Jostedalsbreen area. a) Orthophoto retrieved from norgeibilder.no that covers the lake in 2015.08.20. b) n50 topographic map from kartverket.no produced in December 2015 presenting a smaller glacial lake area compared to more recent satellite images. c) Sentinel-2 image from 2018.07.26, in natural color composite. d) Landsat-8 image from 2018.06.29, in natural color composite. e) SVM, MLC and NVE's outline of the lake on the same Sentinel-2 image. f) SVM, MLC and NVE's outline of the lake on the same Landsat-8 image.

3.5 Evolution of glacial lakes through 1988-2019

As another aim of this study was to assess and study evolution of glacial lakes by application of machine learning methods, the recognized outlines of glacial lakes in the three time spans of study, were investigated in contrast. Therefore, MLC was applied on ACIs and non-ACIs in two of the time spans in this study, 1999-2006 and 2018-2019 (see section 3.1.3 and 3.1.4). The method was also applied on non-ACIs from the period of 1988-1997 (see section 3.1.5).

Unlike 1999-2006, glacier inventory for 2018-2019 was not completed, which led the focus of this part of the study to southern Norway. Figure 3.13 depicts some of the glacial lakes recognized by application of MLC on ACIs. As visible from this figure, using atmospherically corrected images caused a discrepancy in the recognition potential of MLC (See figure 3.14 (a-j)

for comparison). Glacial lakes were either partially recognized, recognized smaller than the actual size of lake in the image or not recognized at all in different periods of imagery in use. This issue made the comparison of glacial lake outlines impractical for the purpose of this study; thus, adopting non-ACIs was identified as the only option for following glacial lakes evolution and change through years.

Figure 3.14 shows some of the recognized glacial lakes through the years in this study. Images (a) to (j) are comparable to the ones recognized by using ACIs in figure 3.13. Use of non-ACIs resulted in more precise glacial lake outlines, providing the opportunity for comparison and following the changes.

Images a, c, f, h, j, and m contain outlines of glacial lakes in all years included in this study and make a complete assessment of lake change possible, meanwhile, in images b, d, e, one of the lakes in h, one of the lakes in j, k, l, n, o, p, and q the outlines are missing one period. In section 4.1 of discussion, I describe the possible reasons for the lakes that remained unidentified by MLC in these images in different years.

a)

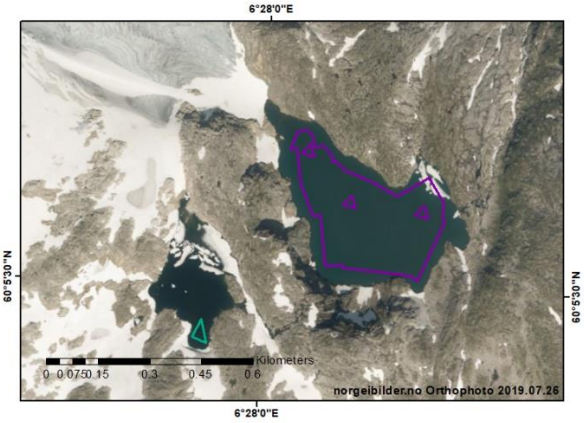
6°28'0"E
60°5'30"N
Kilometers
0 0.075 0.15 0.3 0.45 0.6
norgeibilder.no Orthophoto 2019.07.26

b)

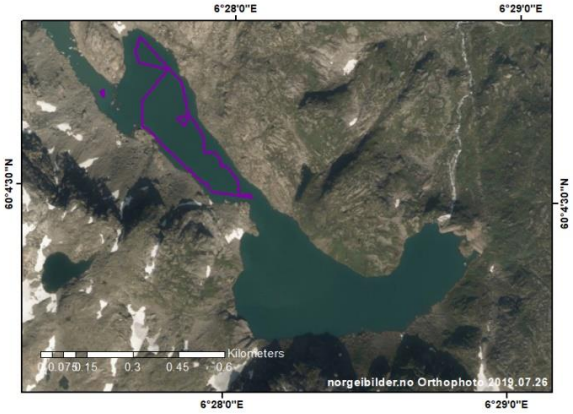
6°28'0"E
6°29'0"E
60°4'30"N
Kilometers
0 0.075 0.15 0.3 0.45 0.6
norgeibilder.no Orthophoto 2019.07.26

c)

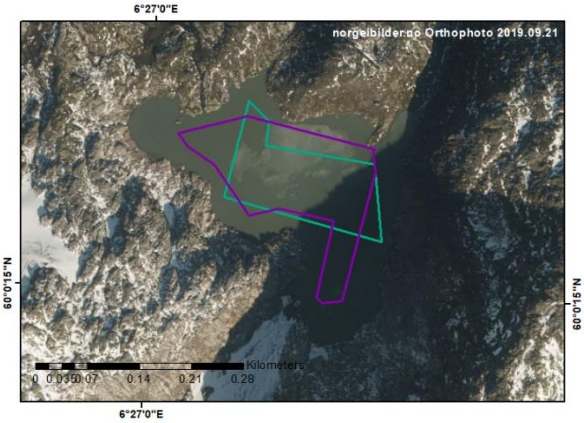
6°27'0"E
60°0'15"N
norgeibilder.no Orthophoto 2019.09.21
Kilometers
0 0.035 0.07 0.14 0.21 0.28

d)

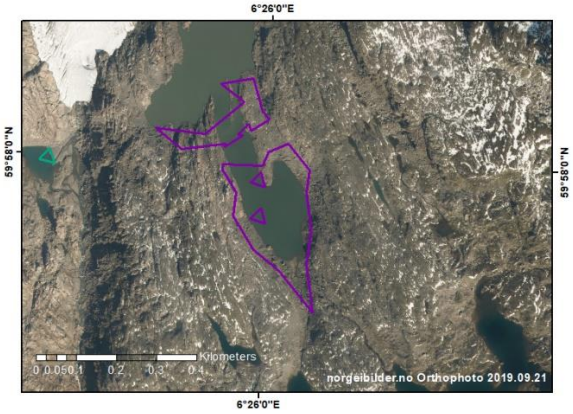
6°26'0"E
59°58'0"N
Kilometers
0 0.05 0.1 0.2 0.3 0.4
norgeibilder.no Orthophoto 2019.09.21

e)

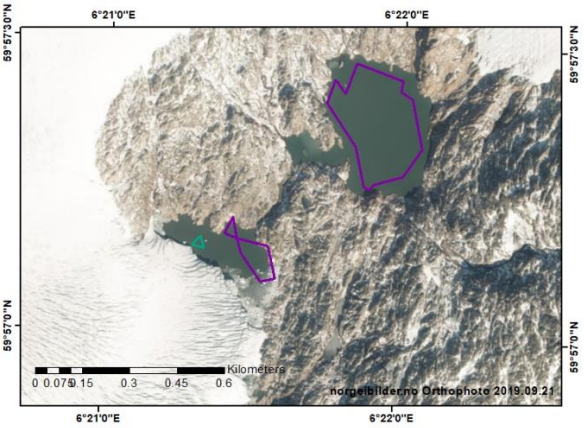
6°21'0"E
6°22'0"E
59°57'30"N
59°57'0"N
Kilometers
0 0.075 0.15 0.3 0.45 0.6
norgeibilder.no Orthophoto 2019.09.21

f)

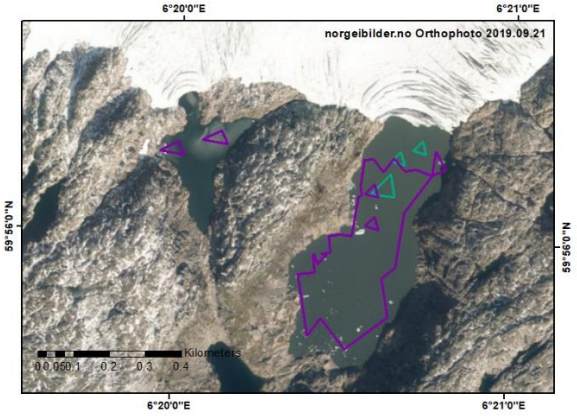
6°20'0"E
6°21'0"E
59°59'0"N
Kilometers
0 0.05 0.1 0.2 0.3 0.4
norgeibilder.no Orthophoto 2019.09.21

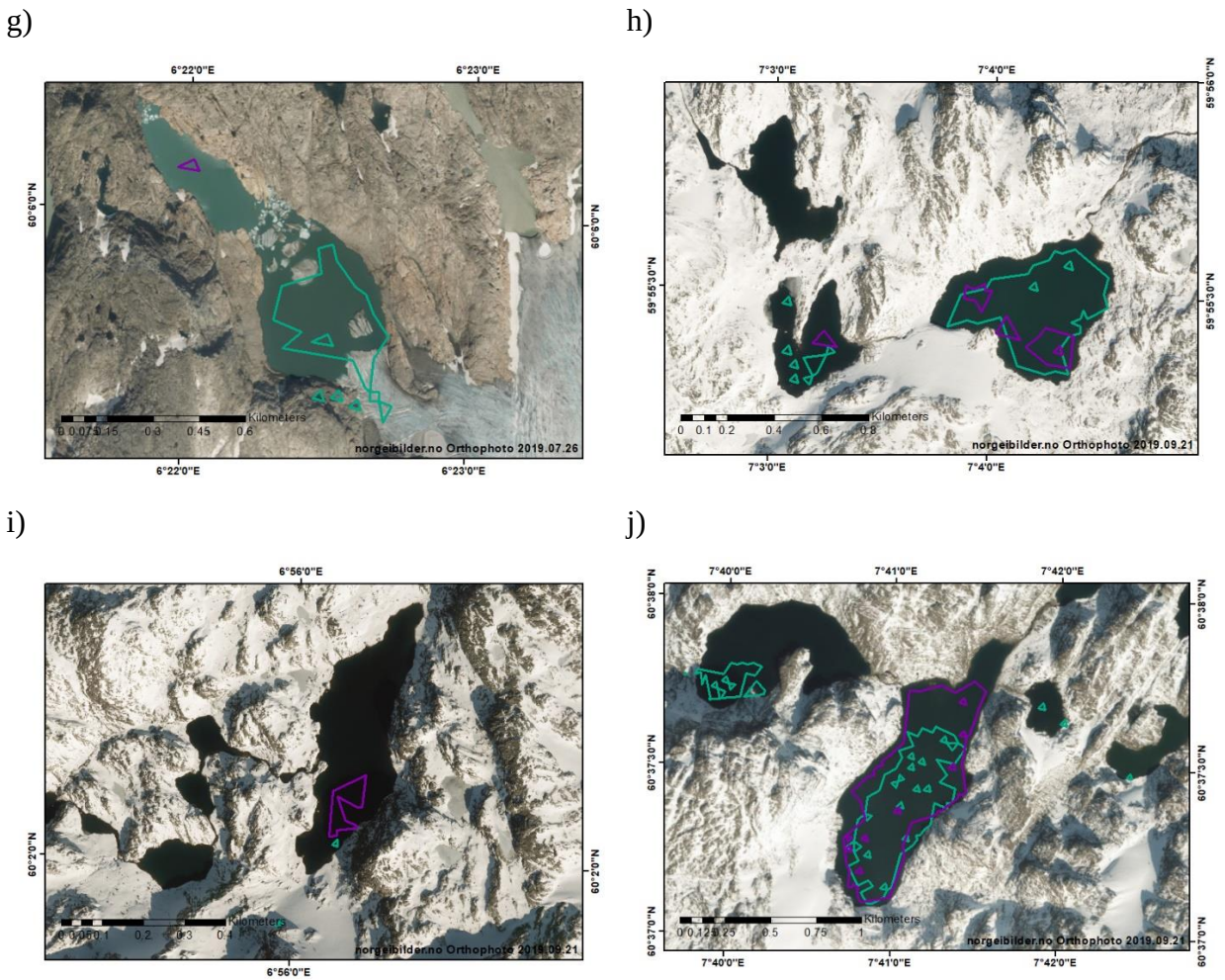

Figure 3.13 Recognition of glacial lakes by MLC applied on ACIs. Purple and cyan outlines of glacial lakes belong to 1999-2006 and 2018-2019, respectively. The orthophotos in the background are used for display purpose, from norgeibilder.no.

a)

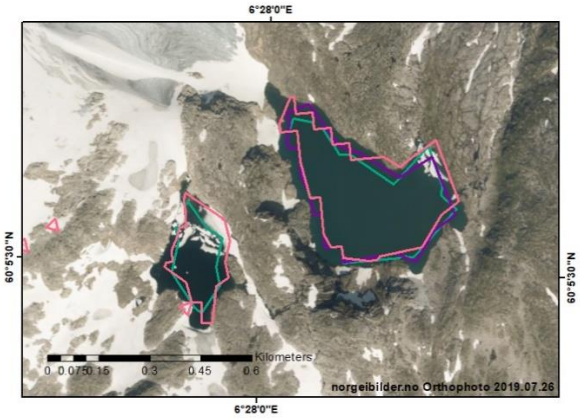
6°28'0"E
60°5'30"N
Kilometers
0 0.075 0.15 0.3 0.45 0.6
norgeibilder.no Orthophoto 2019.07.26

b)

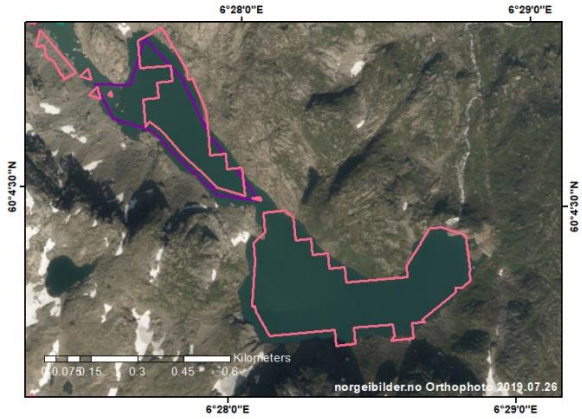
6°28'0"E
6°29'0"E
60°4'30"N
Kilometers
0 0.075 0.15 0.3 0.45 0.6
norgeibilder.no Orthophoto 2019.07.26

c)

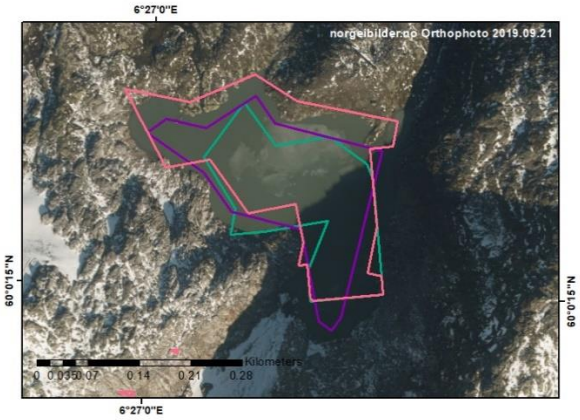
6°27'0"E
60°0'15"N
Kilometers
0 0.035 0.07 0.14 0.21 0.28
norgeibilder.no Orthophoto 2019.09.21

d)

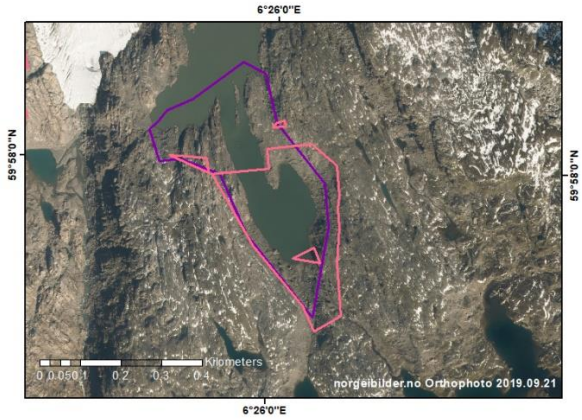
6°26'0"E
59°58'0"N
Kilometers
0 0.05 0.1 0.2 0.3 0.4
norgeibilder.no Orthophoto 2019.09.21

e)

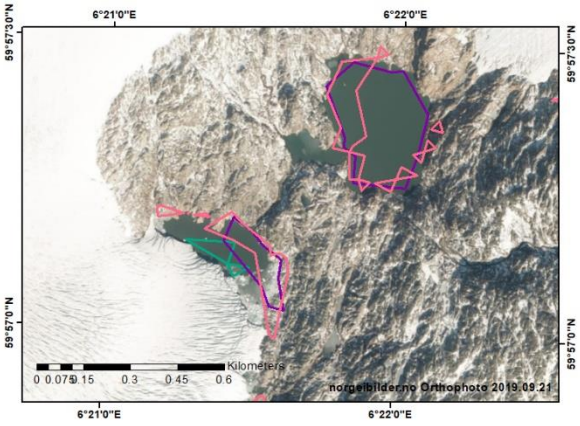
6°21'0"E
6°22'0"E
59°57'30"N
59°57'0"N
Kilometers
0 0.075 0.15 0.3 0.45 0.6
norgeibilder.no Orthophoto 2019.09.21

f)

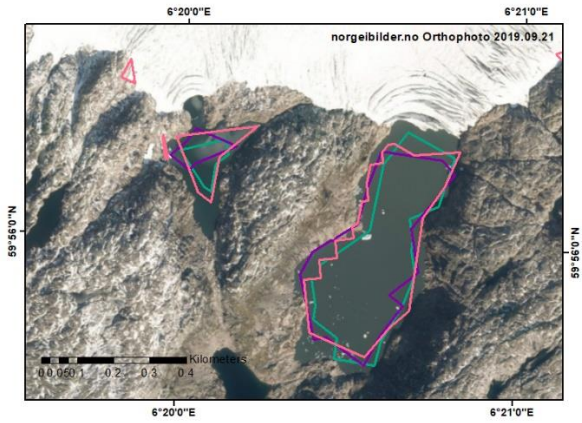
6°20'0"E
6°21'0"E
59°56'0"N
Kilometers
0 0.05 0.1 0.2 0.3 0.4
norgeibilder.no Orthophoto 2019.09.21

g)

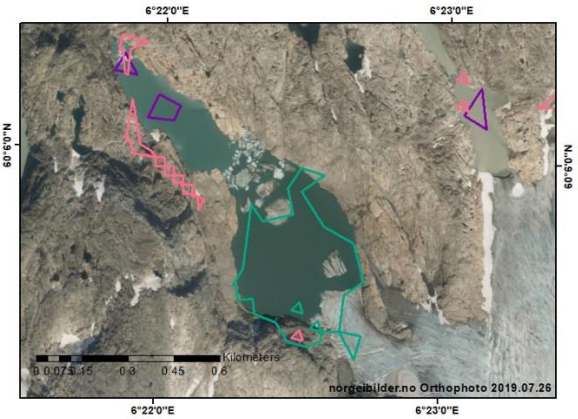
6°22'0"E
6°23'0"E
60°5'0"N
60°4'0"N
Kilometers
0 0.075 0.15 0.3 0.45 0.6
norgeibilder.no Orthophoto 2019.07.26

h)

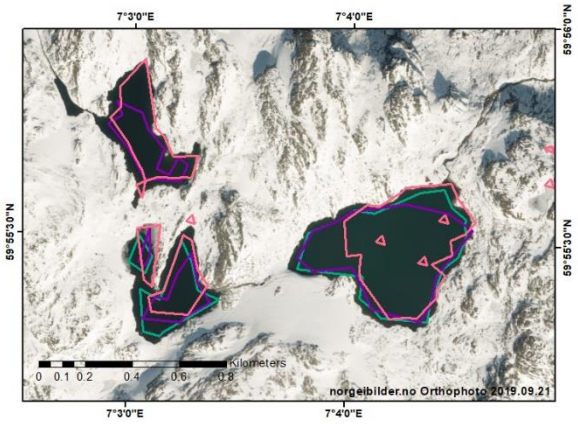
7°3'0"E
7°4'0"E
59°56'0"N
59°55'30"N
Kilometers
0 0.1 0.2 0.4 0.6 0.8
norgeibilder.no Orthophoto 2019.09.21

i)

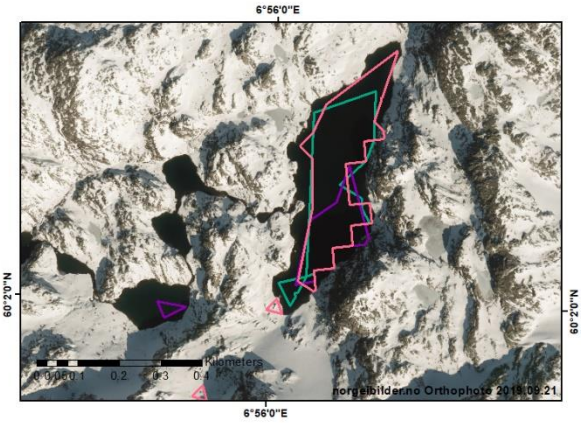
6°56'0"E
60°21'0"N
60°20'0"N
Kilometers
0 0.05 0.1 0.2 0.3 0.4
norgeibilder.no Orthophoto 2019.09.21

j)

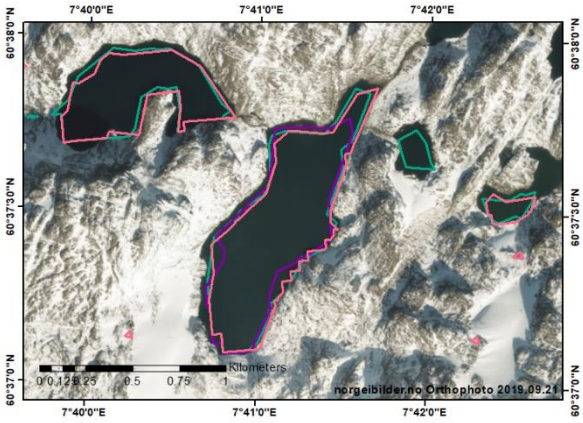
7°40'0"E
7°41'0"E
7°42'0"E
60°38'0"N
60°37'30"N
60°37'0"N
Kilometers
0 0.125 0.25 0.5 0.75 1
norgeibilder.no Orthophoto 2019.09.21

k)

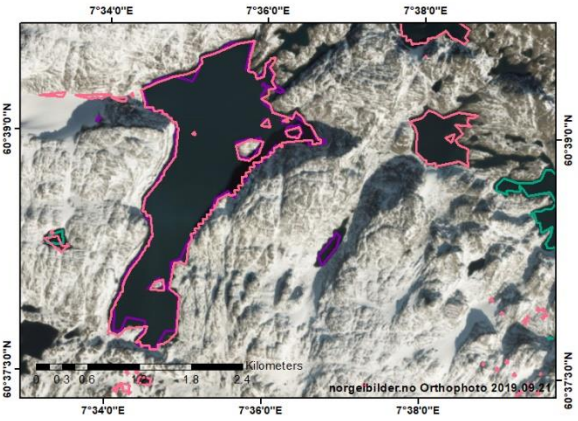
7°34'0"E
7°36'0"E
7°38'0"E
60°39'0"N
60°38'30"N
60°37'30"N
Kilometers
0 0.3 0.6 1.2 1.8 2.4
norgeibilder.no Orthophoto 2019.09.21

l)

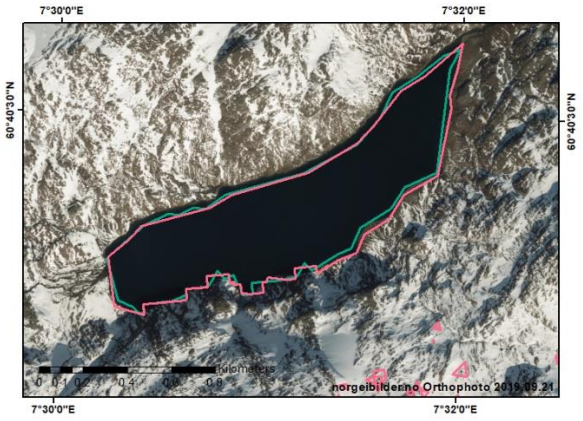
7°30'0"E
7°32'0"E
60°40'30"N
60°40'0"N
Kilometers
0 0.1 0.2 0.4 0.6 0.8
norgeibilder.no Orthophoto 2019.09.21

m)

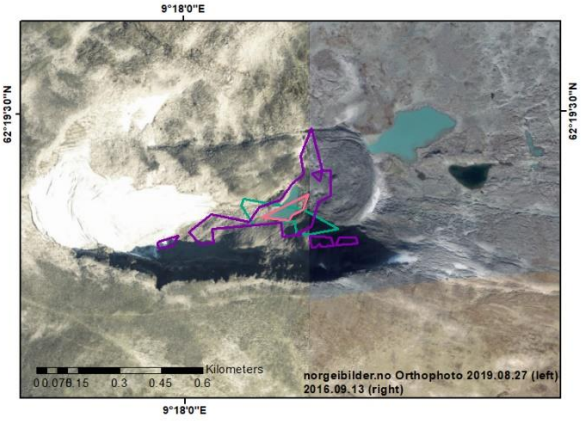
9°18'0"E
62°19'30"N
Kilometers
norgeibilder.no Orthophoto 2019.08.27 (left)
2016.09.13 (right)

n)

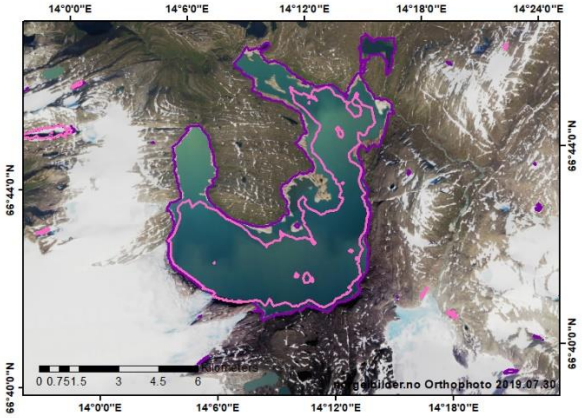
14°0'0"E
14°6'0"E
14°12'0"E
14°18'0"E
14°24'0"E
Kilometers
norgeibilder.no Orthophoto 2019.07.30

o)

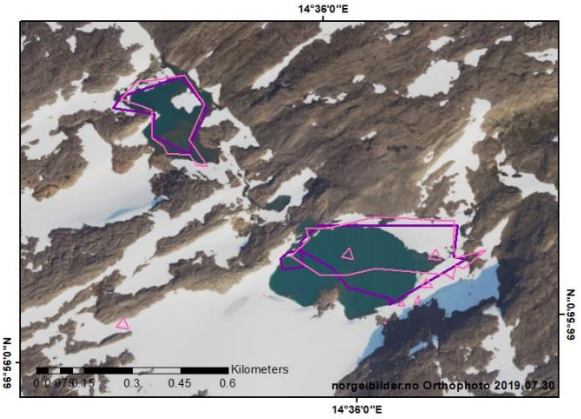
14°36'0"E
Kilometers
norgeibilder.no Orthophoto 2019.07.30

p)

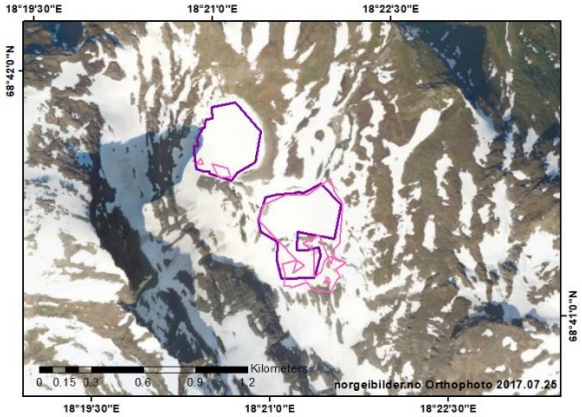
18°19'30"E
18°21'0"E
18°22'30"E
68°42'0"N
Kilometers
norgeibilder.no Orthophoto 2017.07.25

q)

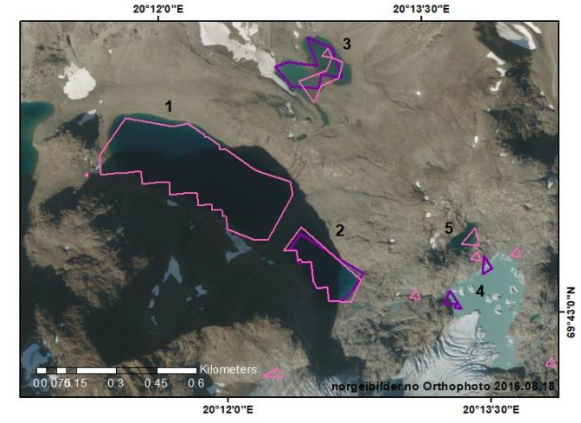
20°12'0"E
20°13'30"E
1
2
3
4
5
Kilometers
norgeibilder.no Orthophoto 2016.08.18

r)

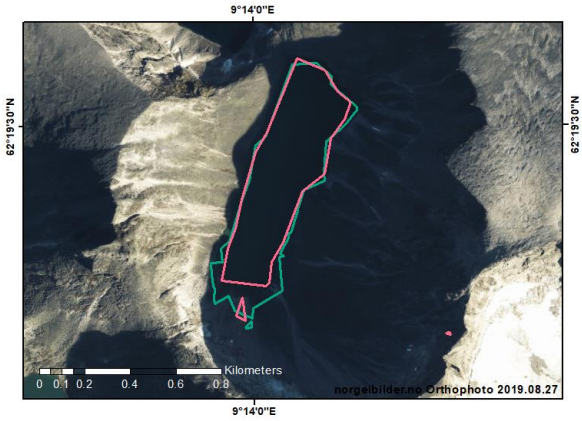
9°14'0"E
62°19'30"N
Kilometers
norgeibilder.no Orthophoto 2019.08.27

s)

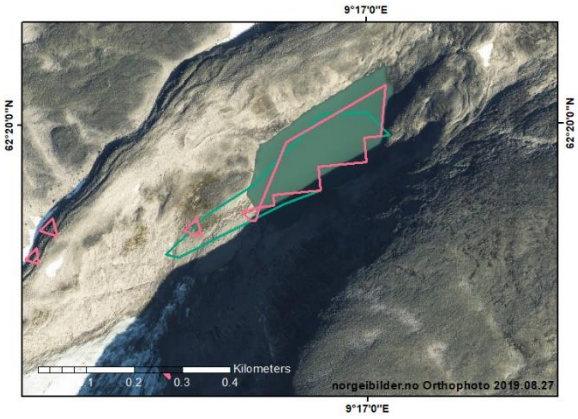

Figure 3.14 Recognition of glacial lakes by MLC applied on non-ACIs. Pink, purple, and cyan outlines of glacial lakes belong to 1988-1997, 1999-2006, 2018-2019, respectively. The orthophotos in the background are used for display purpose only, from norgeibilder.no.

4 Discussion

The discussion in this study is structured in four sections which analyze the technical and scientific results presented in Chapter 3 in the light of the main objectives of this thesis outlined in the introduction (Section 1.3).

In this chapter, I first discuss the ability of the Maximum Likelihood Classification (MLC) to recognize and track long-term changes in glacial lakes using Landsat series, including its potential to identify the timing of their formation and their subsequent life cycle. As part of this analysis, I question whether atmospheric corrections on satellite imagery are potentially harmful to studies that target alike methods and processes. Subsequently, the discussion revolves around pros and cons of glacial lake classification based on the Sentinel images versus the Landsat series (Section 4.2) and assesses the performance of the Support Vector Machine (SVM) classification against the outcomes of MLC on both Landsat and Sentinel images (Section 4.3).

4.1 Glacial lake recognition

4.1.1 Constitutional factors interfering studies on glacial lake changes

To support the assertion that machine learning algorithms have the potential to recognize and follow glacial lake life cycles, MLC has been applied on Landsat images in three time periods: 1988-1997, 1999-2006 and 2018-2019. The results of this study have made it blatantly clear that image preprocessing steps taken prior to glacial lake classification have large and sometimes unexpected effects on the quality of the final product. Figure 4.1 contains an example of such unexpected effects: Although atmospheric corrections are among common steps preceding an application of classification methods on satellite imagery, they do not always lead to improvements in the classification outcomes and indeed may lead to the opposite, as visualized here and in the results presented in Section 3.1. Although some glacial lakes are recognized when applying MLC on both atmospherically corrected and uncorrected images (ACIs and non-

ACIs, respectively, yellow circles in figure 4.1), many more lakes remain undetected or only partially outlined in ACIs (cyan circles in figure 4.1). This is due to the fact that digital numbers (DNs) of pixels in the satellite imagery are altered by atmospheric corrections (section 2.4.2). Once an image undergoes an atmospheric correction intended to reduce the effects of solar radiation scattering, a constant value is subtracted from the entire image, leading to a decrease in DN values. In contrast, corrections for solar radiation absorption have a multiplicative effect and can lead to an increase in the DN value. As a result, correcting for both the absorption and scattering effects often leads to non-uniform changes in DN values (Goslee, 2011).

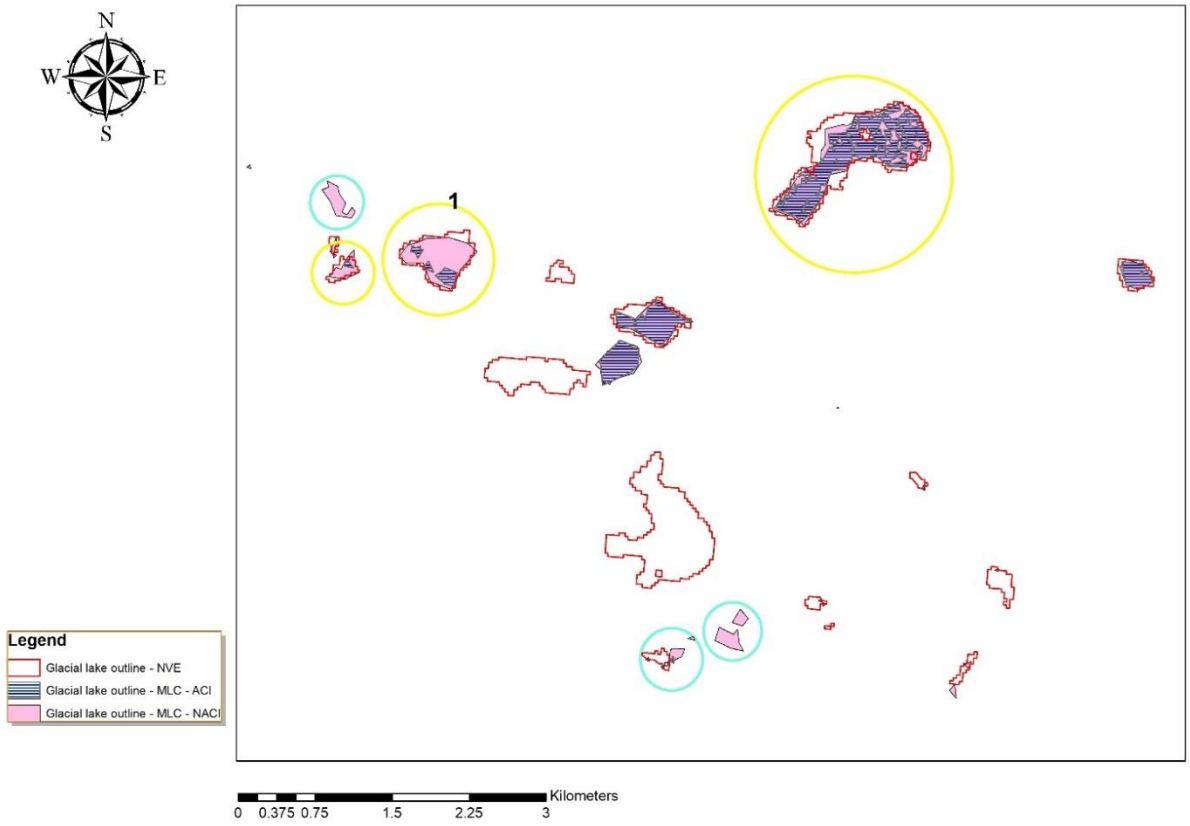

Figure 4.1 Comparison of glacial lake outlines extracted by MLC from ACIs vs non-ACIs in 1999-2006. Yellow circles mark glacial lakes recognized by both ACIs and non-ACIs. Cyan circles mark no detection or partial recognition of glacial lakes by ACIs.

As explained in the preceding chapters, supervised classification methods perform the selection of pixel values that are representative of a certain land class using signature files from training

samples created by the user. The findings in this study show that pixel values belonging to bands NIR and SWIR1 have a greater influence on the method's ability to isolate water bodies compared to other bands. The correction-induced changes in their pixel values have been observed to push DNs outside the value range assigned to water bodies, thus impairing the quality of the lake recognition. My general observation based on the evaluation of classification results presented in Section 3.1 is that MLC captures glacial lake outlines more realistically when applied on non-ACIs.

This result is important because it obviates the necessity to involve additional image pre-processing tools. Applications of atmospheric corrections on satellite images require the use of third-party software, which, in the case of this study, is ENVI 5.8. Furthermore, atmospheric corrections tend to introduce no-value pixels in the imagery that obscure the quality of their classification (section 2.4.6). In most cases, the classification method recognizes no-value pixels as water bodies, affecting sizes and shapes of the identified lakes and introducing noise in the classification. Overall, the false recognition of no-value pixels leads to a general overestimation of the number of classified water bodies, putting a heavier weight on the subsequent corrections for shadow-related misclassifications. Although the classification on ACIs leads to an increase in falsely recognized water bodies, my results show that it generally fails to recognize many of the existing glacial lakes that are detected by the classification on non-ACIs. In the results for southern Norway obtained for the period of 1999-2006, 154 of 316 lakes recognized by the classification on non-ACIs have been missed by the ACI application. In addition, the ACI applications tend to partition larger lakes into smaller water bodies, as demonstrated in figure 4.1 by one of the yellow circles (circle 1). Here a larger glacial lake is divided into three smaller lakes due to ACI-induced artefacts. Such artificial lake divisions do not only inflate the number of glacial lakes recognized but also lead to some of the lake sectors being misclassified as proglacial instead of glacial. Thus, 249 lakes recognized by MLC on ACIs within the southern domain (1999-2006) are not necessarily separate glacial lakes but could be parts of the same lakes that were not recognized as a whole.

A ten-fold overestimation of the number of recognized glacial lakes in both southern and northern domains in the oldest period included in this study (1988-1997) is also partly due to the

partitioning of larger glacial lakes into smaller lake polygons, albeit for a different reason. While in other time intervals, this issue is mainly related to the image corruption by the atmospheric corrections in 1988-1997, it also affects the results of classification on non-ACIs, displaying highly unrealistic increases in the glacier lake number. Overall, 1085 and 1182 glacial lakes were identified in northern and southern Norway, respectively, as opposed to only 91 and 102 lakes included in the inventory. As discussed below, the numbers included in the glacial lake inventory for this period should be treated with caution since they are derived using vastly different criteria for the glacial lake identification than in other inventories and in this study. Nevertheless, the inferred number of glacial lakes is also substantially larger than in the inventories and classification results for other periods. A deeper analysis of the classification outcomes has revealed that the larger number of lakes recognized during the oldest studied period is a consequence of not only lake division but also of the false classification of wet snow and ice along glacier margins. This issue has led to a large additional number of lakes with a size of <0.002. This peculiar circumstance can be likely attributed to the low resolution of the imagery retrieved from Landsat 5 between 1988 and 1997 since this issue does not appear in the classification of images from more recent periods.

4.1.2 External factors interfering studies on glacial lake changes

It is noteworthy that the NVE's inventories of glaciers and glacial lakes follow different definitions and division fundamentals for different time spans (see sections 1.1 and 1.2). In fact, each of the glacier and glacial lake inventories has been generated using different criteria, thereby complicating any attempts to infer temporal changes in the glacial lake numbers and areas. Therefore, the fact that some glacial lakes, which are not included in the inventories, are detected by MLC does not necessarily challenge the correctness of the classification outcomes but may instead indicate differences in the criteria used. After all, the main purpose of NVE's inventories in this study is to enable validation of automatically generated glacial lake outlines. They served this purpose well when classification methods failed to detect glacial lakes where they were indicated by inventories. For example, while assessing the MLC-based glacial lake outlines for the period of 1999-2006, I spotted some lakes that were missing compared to the

NVE's inventory. A comparison of the retrieved classes with the original composite and good resolution images of Google Earth has shown that the missing lakes located in the proximity of glaciers were covered in snow and ice at the time of image retrieval. In figure 4.2, the black arrows numbered 1-5 point at glacial lakes that appear as snow or ice in the composite image (light green colour marks ice and snow).

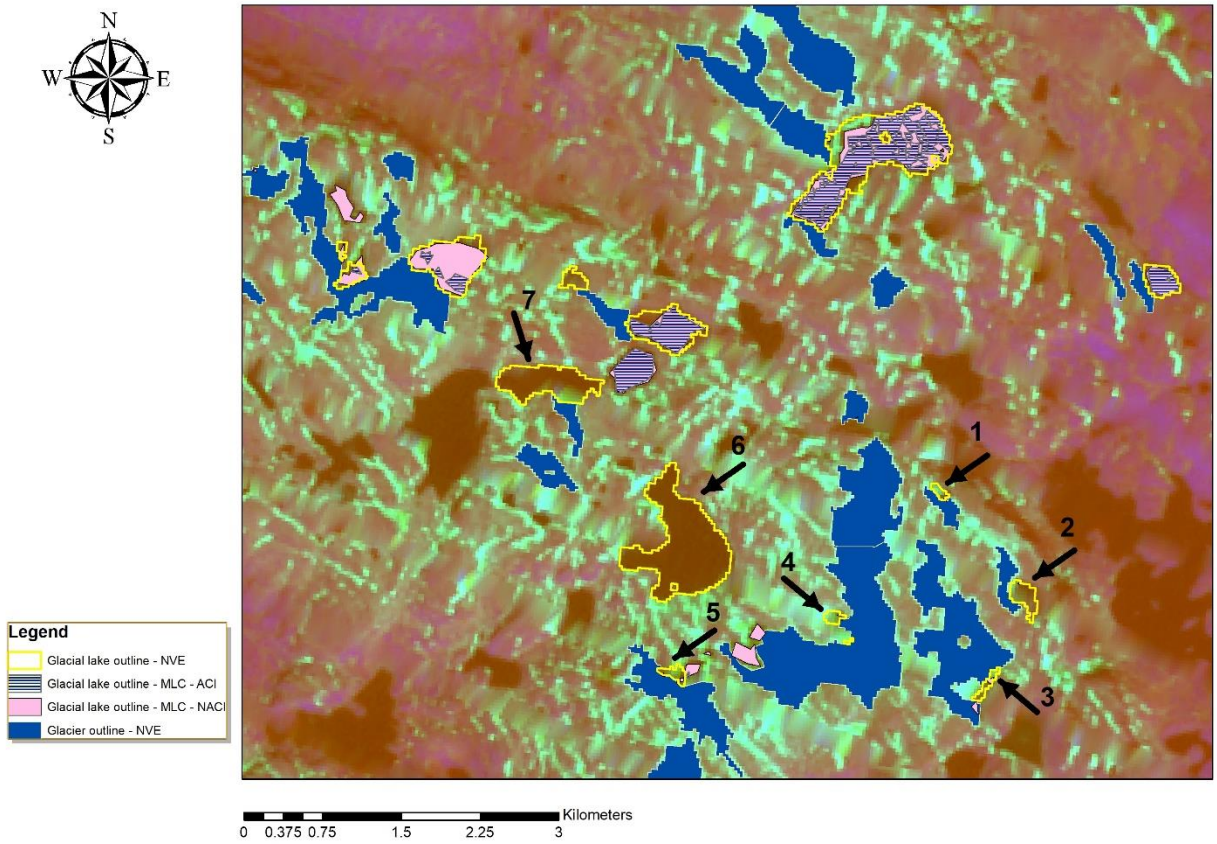

Figure 4.2 Comparison of glacial lake outlines based on MLC from ACIs and non-ACIs, and NVE's inventory from 1999-2006. The background is the composite image. Lakes with arrows numbered 1-5, and 7 are only included in NVE's inventory due to complete or partial coverage by snow and ice in the original image. Lake with arrow number 6 remained unrecognized by MLC due to lacking relative glacier outline for this study period.

Unfortunately, the correctness of glacial lake classification is considerably dependent on the quality of images. One of the initial steps in the pre-selection of high-quality satellite images is filtering out images with cloud cover above a certain threshold (in this study, 15%). Eliminating images with considerable snow and ice cover is another yet more time-consuming step that requires thorough visual inspection of each image before downloading. Despite having

performed these steps, some visually acceptable images can lead to undesirable results, such as the elimination of lakes in contact with glaciers illustrated in figure 4.2.

Another type of misclassification caused by the poor quality of the original satellite image is exemplified by the lake marked with arrow number 7 (figure 4.2). At the time of image retrieval, the glacier-proximal margin of the lake was still covered by ice. Therefore, the ice-free portions of the recognized lake happened to be outside the pre-defined 100-meter buffer and did not qualify for the adapted glacial lake definition. Similar reasons for misclassifications are illustrated in figures 3.14 (g), (i), (q) and (r), where partial coverage of lakes by ice and snow has led to their elimination from the final glacial lake dataset for one study period but not for the other two periods. This observation clearly demonstrates why the assessment of glacial lake evolution is currently limited by the lack of high-quality images from sequential periods. In some cases, such as exemplified by glacial lakes in figures 3.14 (g) and (q), it is only possible to identify the existence of a glacial lake, even though its complete outline has not been reproduced.

All NVE inventories were missing lake 1 in figure 3.14 (q), which was recognized by MLC during the period of 1988-1997, but by 1999-2006, it was no longer located within the glacier buffer that led to its exclusion from the glacial lake dataset. In the same figure, lake 4 in the 1999-2006 images was partially covered by snow and ice but was nevertheless partly recognized. This was enough to promote an idea of its existence during that period, although it was missing from the corresponding NVE's inventory. The only inventory that includes this lake is from 2018-2019; It can therefore be deduced that the glacial lake existed in 1999-2006 and had grown in size towards 2018-2019 when it was finally included in the NVE's inventory. The same is true for the glacial lake in figure 3.14 (g), where it was partially recognized by MLC for the periods of 1988-1997 and 1999-2006, while it was absent in the corresponding NVE's inventories. Close inspection of the composite and original satellite image indicated that the glacial lake was partially snow/ice-covered. Even though partially recognized glacial lakes could be used as an adequate lead to follow their existence, in this case, too, it was impossible to follow the glacial lake evolution through time.

Throughout the assessment of the classified glacial lake outlines, I observed some contradictions in the occurrence of lakes in the NVE's inventories. While some of the reasons for these

inconsistencies have already been discussed, other potential causes may be exemplified by lake number 6 in figure 4.2. This glacial lake was included in the NVE's inventory for 1999-2006 but could not be recognized as a glacial lake by the analyses in this study due to the lack of an adjacent glacier outline. Indeed, the water body class produced by MLC includes this lake (see figure 4.3). Should the glacier inventory be available, the lake would have been recognized as a glacial lake. Regrettably, the unavailability of complete glacier inventories for specific time spans can be a limiting factor since this information is mandatory for studies of glacial lake life cycles.

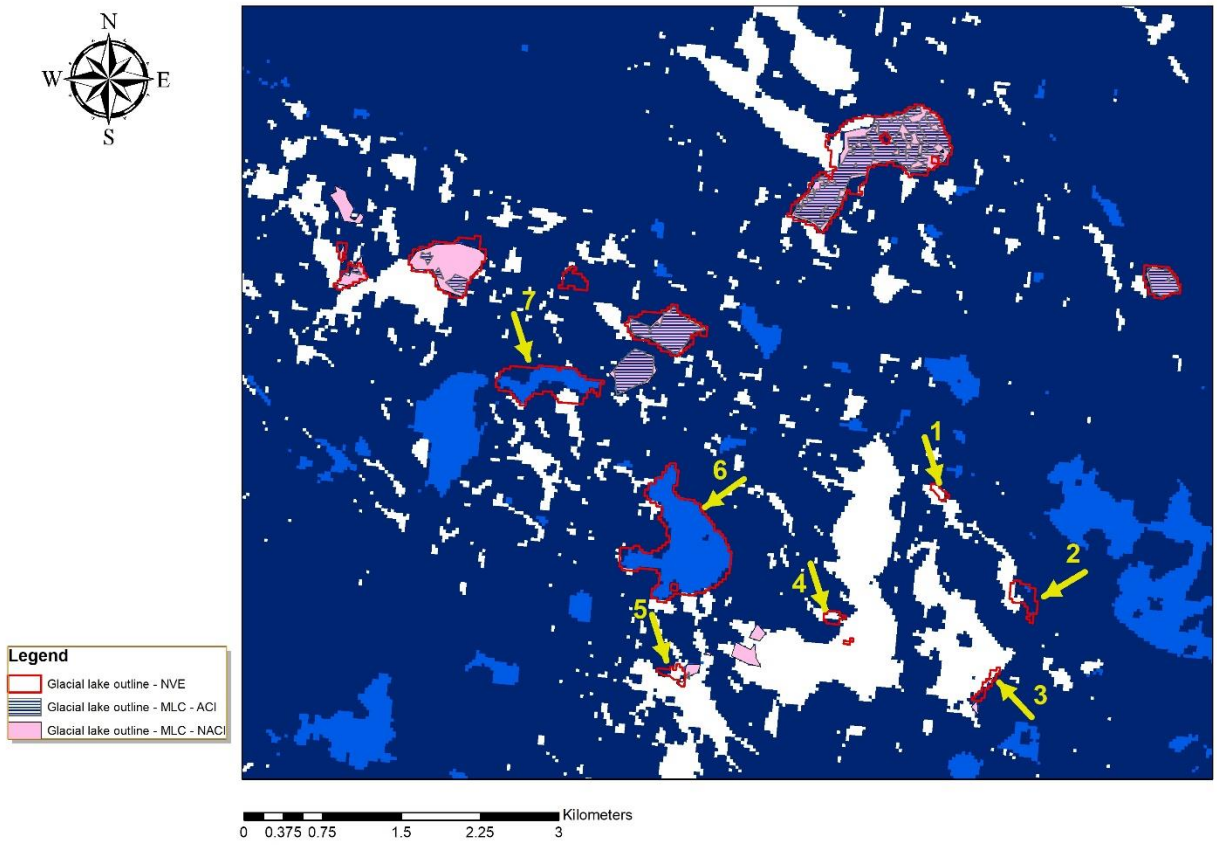

Figure 4.3 Comparison of glacial lake outlines based on MLC from ACIs and non-ACIs, and NVE's inventory from 1999-2006. The background image is the generated MLC image with white displaying ice, light blue, water body and dark blue, land classes. Lakes with arrows numbered 1-5, and 7 display complete or partial coverage by snow and ice in the MLC image, thus are not recognized as glacial lakes by MLC. Lake with arrow number 6, although recognized as water body by MLC, was not recognized a glacial lake due to lacking relative glacier outline for this study period.

Lakes (j) and (s) in figure 3.14 provide other instances where the identification of glacial lakes in one study period was impossible due to the absence of a relative glacier outline from the same period. In such cases, analyses of temporal changes in glacial lakes depend sensitively on the availability of subsequent glacier outlines. The same issue is emphasized in figure 4.4a, where the reconstruction of lake (1) outlines is incomplete due to its absence in the MLC-generated dataset for the period of 1988-1997. This is due to the fact that the glacier in the proximity of the lake was missing from the NVE's inventory. Although the lake was initially recognized by MLC, it was not selected as a glacial lake in the subsequent process due to absence of the glacier buffer.

4.1.3 Glacial lake change tracking by the Landsat series: a closer look

Furthermore, figure 4.4 compares temporal changes in two regulated lakes in the southern and northern domains of this study. Due to the absence of glacier outlines in the north for the most recent period (2018-2019), this comparison is limited to two older periods (1988-1997 versus 1999-2006). Both Stora Vargevatnet (south, figure 4.4a) and Storglomvatnet (north, figure 4.4b) have dams and are therefore not solely controlled by natural external factors.

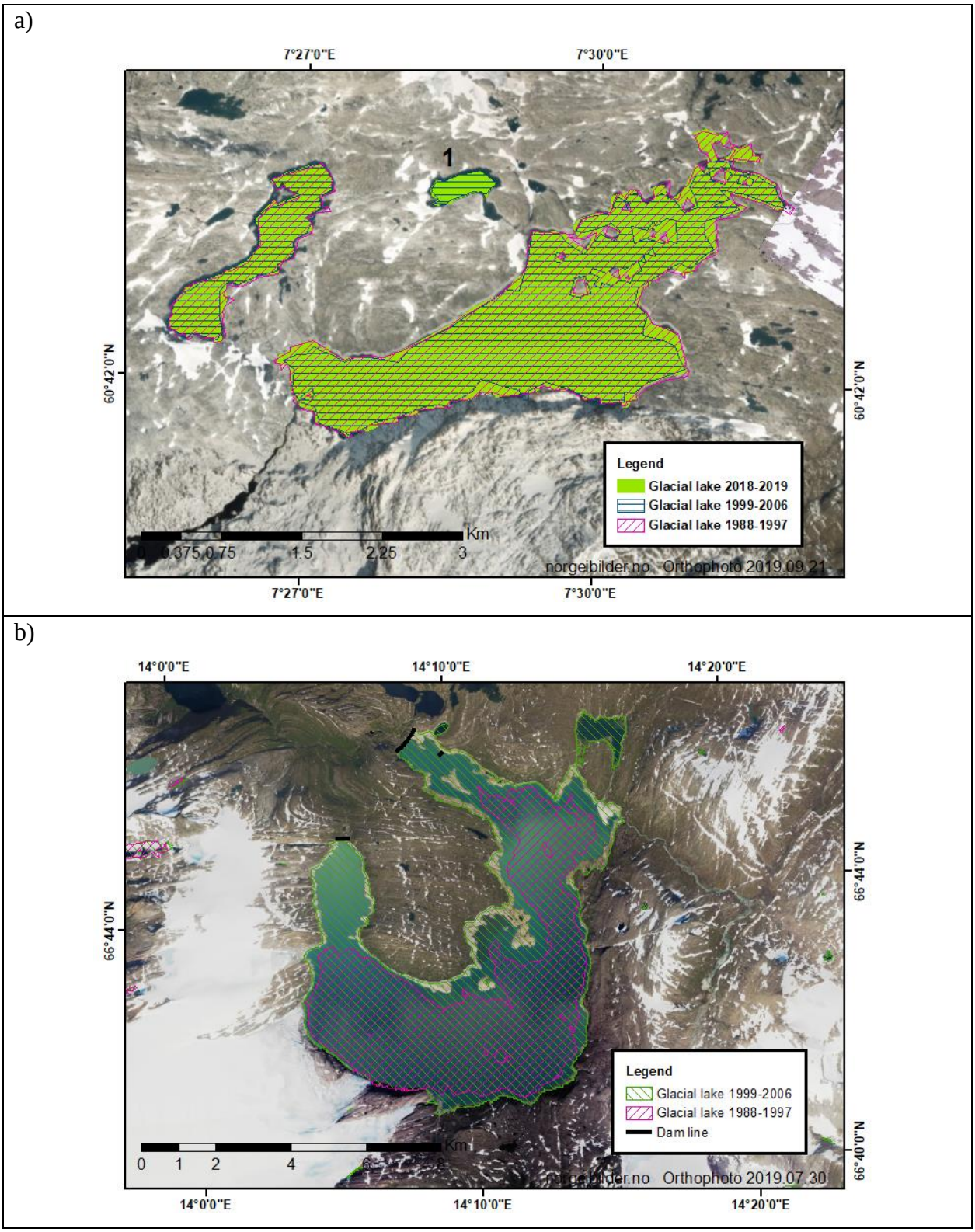

Figure 4.4 Glacial lake life cycle. a) Stora Vargevatnet (the larger lake) and Vetla Vargevatnet glacial lakes located in the north of Hardangerjøkulen, identified in all three time spans. b) Storglomvatnet in northern Norway, on the northeast edge of Svartisen glacier, unidentified in 2018-2019 due to missing relative glacier outline.

While MLC-based lake outlines indicate that Stora Vargevatnet had shrunk during this period, Storglomvatnet had shown significant growth. However, a more detailed inspection of the Stora Vargevatnet outlines in both NVE and MLC databases has revealed that it unlikely experienced any significant change through the documented periods since its outlines in the oldest and most recent periods (1988-1997 versus 2018-2019) were closely matched. It is, therefore, likely that the reduction in the glacial lake area between 1988 and 2006 is merely an artefact in the classification. This is further supported by the synchronized changes in the Stora Vargevatnet and its immediate neighbour to the east, Vetla Vargevatnet (figure 4.4a), where both lakes seem to have shrunk between 1988 and 2006 and then regrown to their original sizes towards 2018-2019. My interpretation is that both lakes in the image selected for the intermediate period (1999-2006) were affected by partial ice and snow coverage along the lake margins and thus were only partly recognized by MCL. In addition, the medium spatial resolution of Landsat images (30 meters) is a limitation to track small changes in the glacial lake areas once such change occurs within a few pixels of a satellite image. However, the observed close match between the lake margins of both Stora Vargevatnet and Vetla Vargevatnet during the oldest and most recent periods (1988-1997 versus 2018-2019) make a strong case against the insignificant resolution being a major driver of misclassification.

As for Storglomvatnet, it tells a completely different story. This regulated lake is located in northern Norway by Svartisen glacier and is used as a reservoir for Svartisen hydroelectric power station. The hydroelectric power station and the dams on both ends of the lake were established in 1993 and 1997, respectively, while the earlier outline of the glacial lake was produced by MLC on a Landsat scene from 1988, prior to the establishment of the power station and the dams. Hence, it can be deducted that the glacial lake outline from 1988 corresponds to the actual glacial lake area prior to the anthropogenic interference. Being a regulated lake, the surface area of Storglomvatnet can experience rapid changes through time, and MLC has proven to be efficient for the detection of such alterations, pointing out at significant impacts of human activities on these remote environments.

Figures 4.5 and 4.6 are other instances where significant changes in the surface areas and glacial lake outlines can be followed efficiently through decades using Landsat images. In these

instances, a detailed interpretation of historical changes has been enabled by the availability of complete glacier outlines and high-quality images. In figure 4.5, both glacial lakes are located within the southern domain - one by Ramnabergbreen glacier to the northwest of Hardangerjøkulen and another (Mosevatnet) to the south of Folgefonna. Here both glacial lakes had shown significant growth between 1988 and 2018-2019. Interestingly, both lakes had only expanded along one of their margins, suggesting that the lake growth was driven by the retreat of glaciers. While retreating, glaciers left a depression that kept receiving meltwater that gradually filled newly exposed areas. The glacier outlines from different period of the study closely correlate with corresponding changes in the glacial lake outlines, providing proof that glacier retreat was the cause of the lake area expansion.

a)

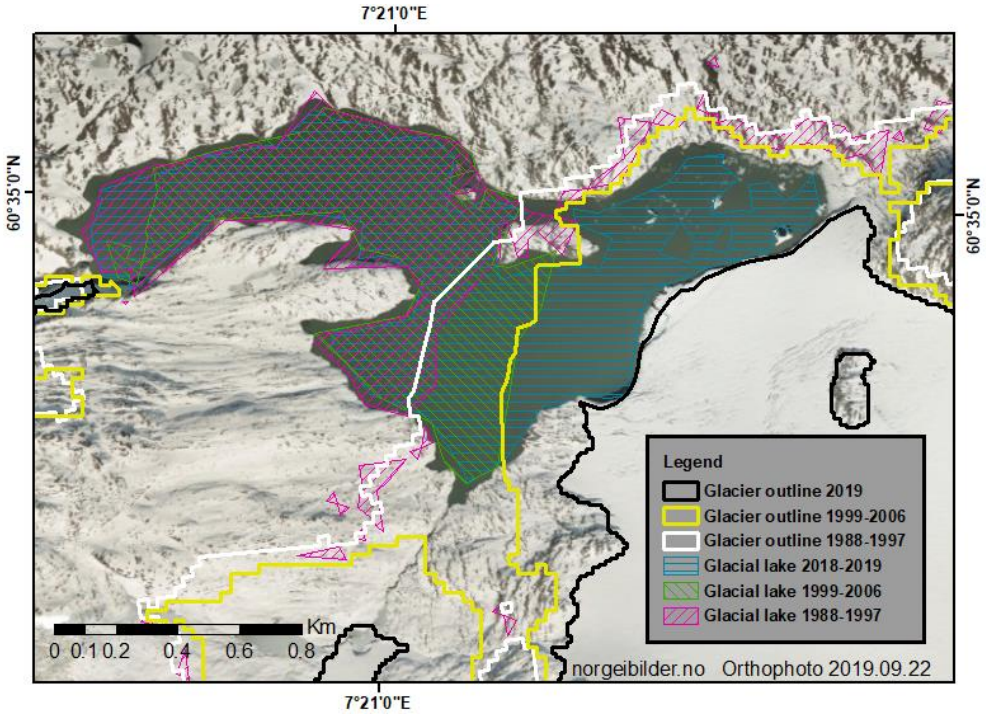

b)

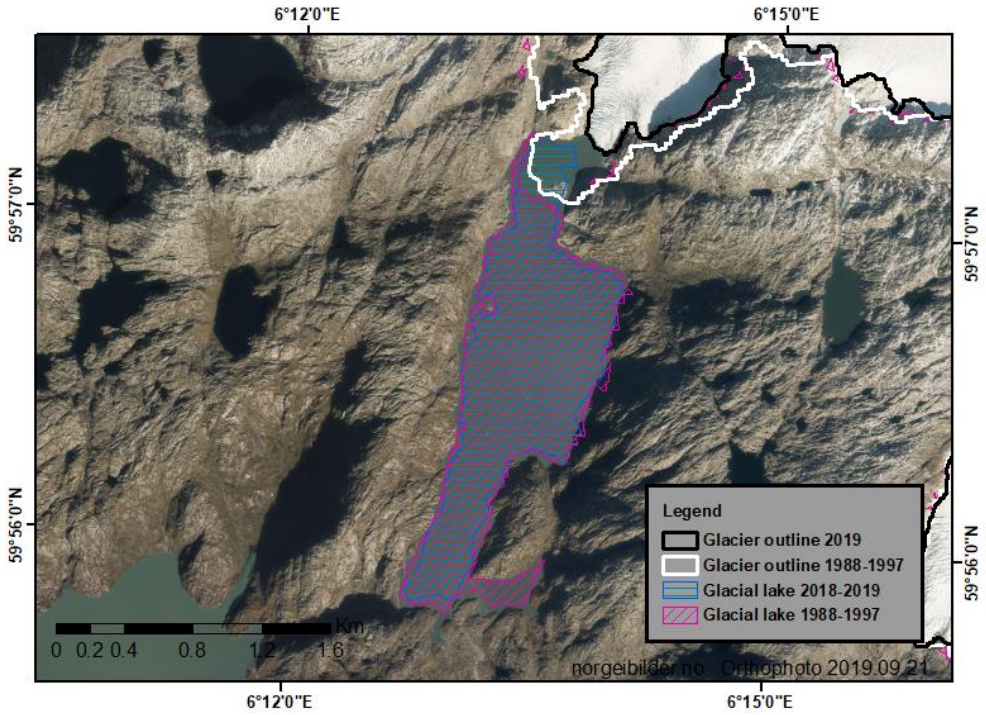

Figure 4.5 Glacial lake life cycle and development. a) The glacial lake located in the northwest of Hardangerjøkulen, by Ramnabergbreen glacier, identified in the three time spans. Relative glacier outlines match lake development

pattern. b) Insta Mosevatnet glacial lake, in south of Folgefonna, by Møsevassbrea glacier, identified in the oldest and most recent time span of study. Lake development follows glacier retreat pattern.

In the same area, MLC "failed" to recognize the lake Demmevatnet located at the margin of a glacier outlet of Hardangerjøkulen in southern Norway (figure 4.6). This seeming failure only affected the MLC recognition skill during the most recent period (2018-2019), potentially indicating some issues with the lake signature in the Landsat image retrieved on the 22nd of September 2019. As a curious incident, a more thorough investigation seemed necessary, especially in the light of the knowledge of jøkulhlaup background in this lake.

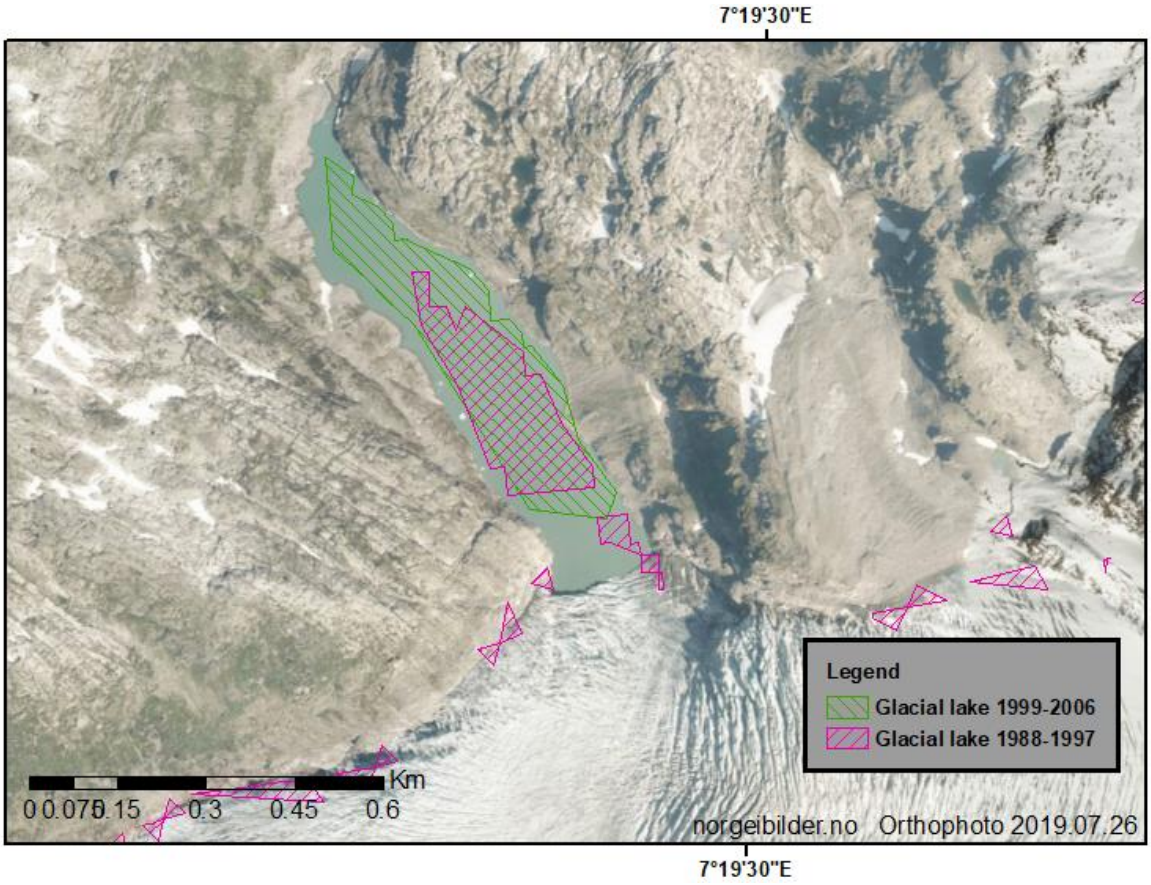

Figure 4.6 Glacial lake life cycle. Demmevatnet, located in the west of Hardangerjøkulen by Rembesdalskåka glacier, is a glacial lake with jøkulhlaup events. The glacial lake outline of 2018-2019 is missing due to a jøkulhlaup event prior to date of satellite image retrieval for MLC application.

The Icelandic term “jøkulhlaup” or glacial lake outburst flood (GLOF), is defined as a sudden burst of meltwater from a glacier leading to floods (sometimes megafloods) impacting the landscape downstream. They may originate from marginal or subglacial sources of meltwater that are discharged due to failure of glacial lake dams, including glacier ice or moraine dams (H. Bjornsson, 2003; H Bjornsson, 2009; Björnsson, 1974). In Norway, jøkulhlaups are common in both the northern and southern study domains and typically occur in the ice-dammed glacial lakes in late summer – early autumn (Jackson & Ragulina, 2014). All images used in this study were retrieved in summer and early autumn since these seasons present better options for glacial lake remote sensing in Norway due to low cloud and snow/ice coverage. As mentioned before, the date of retrieval for the image featuring Demmevatnet was the 22nd of September 2019. The satellite image and its composite of bands were visually inspected, revealing no snow, ice or cloud cover, and indeed the missing lake. Further investigation involved the NVE’s jøkulhlaup database that confirmed a jøkulhlaup event a month prior, on the 24th of August 2019, emptying the lake Demmevatnet (Kjøllmoen *et al.*, 2020; "NVE's GLOF database," 2021).

Although jøkulhlaups are sudden events, their duration ranges between 2-3 days to 2-3 weeks at the most (H. Bjornsson, 1992). Therefore, the Landsat images with 16-day acquisition intervals are not the best choice for recording them. Meanwhile, in a country such as Norway, where jøkulhlaups are among the most common glacier hazards (Jackson & Ragulina, 2014), familiarizing the remote sensing analyst with the distribution of lakes prone to jøkulhlaups is beneficial, as occasions where jøkulhlaups are caught on Landsat images remain rare but valuable. On the other hand, access to more frequent satellite images such as those provided by Sentinel increases the chances to identify more lakes with these characteristics in remote sensing studies (L. Andreassen *et al.*, 2021).

Following a consistent classification method based on a non-conflicting definition of glacial lakes is a necessary key to study the long-term evolution and life cycles of glacial lakes. However, the many cases discussed in this section emphasize the importance of keeping a record of previously known glacial lakes in order to identify any inconsistencies in the classification outcomes, whether these are related to the performance of classification methods, insufficient quality of satellite images or unexpected physical processes such as exemplified by the

jøkulhlaup at Demmevatnet. As an instance, the glacial lake featured in image 3.20 (k) is recognized by MLC in 1988-1997, whilst it is missing from NVE's inventory from the same period. Its MLC-generated outlines for the earlier historical periods (1988-1997 and 1999-2006) showed little change in the lake area. However, by 2018-2019 glacier retreat placed this lake outside the pre-defined glacier buffer and thus outside the glacial lake inventory. In such a case, a time travel to the earlier stages of the glacial lake evolution and the moment of its elimination from the inventory is now within reach, given that a record of the lake as a previously known glacial lake is kept for further assessment and planning.

4.2 Pleading the case of higher resolution images and missing thermal band: Sentinel vs Landsat

4.2.1 Pros and cons of Sentinel and Landsat images in glacial lake recognition tasks

The total area of glacial lakes recognized on Sentinel-2 images in southern Norway is significantly lower than from MLC application on Landsat-8 images (table 3.3). Naturally, analyses on Sentinel and Landsat images could not be replicated exactly due to differences in the image quality (snow/ice and cloud cover), dates of retrieval, and necessary adjustments to signature files with spectral characteristics specific to the two sets of satellite images. Partly due to these technical aspects, there are significant differences in the glacial lake areas recognized by MLC on Landsat-8 and Sentinel-2 images (figures 4.7-a and -b).

a)

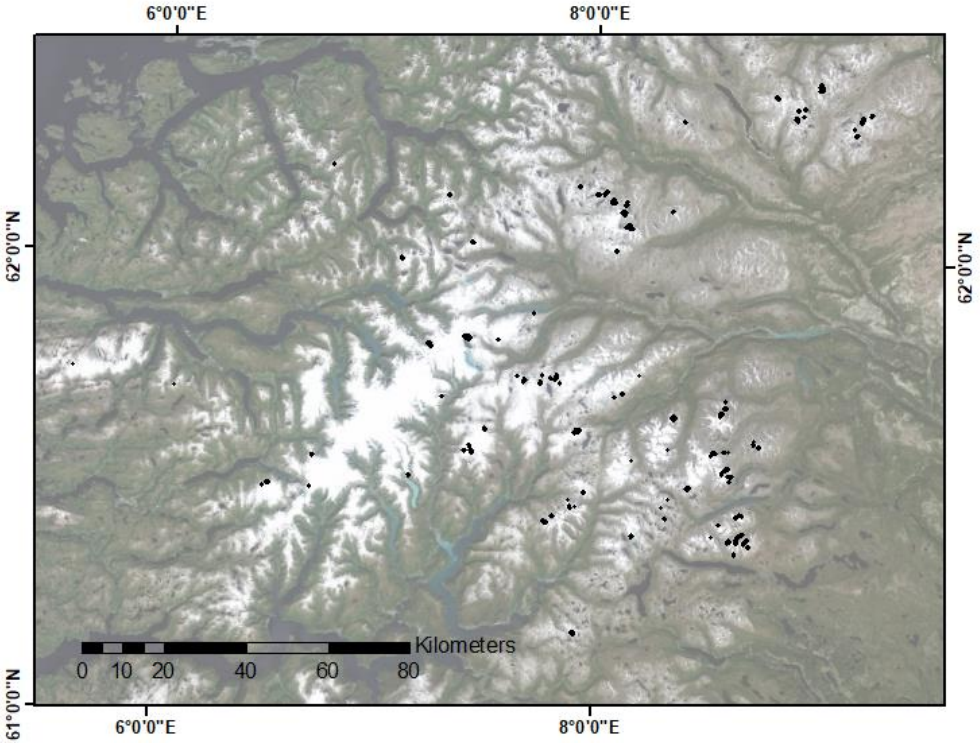
6°0'0"E
8°0'0"E
62°0'0"N
61°0'0"N
Kilometers
0 10 20 40 60 80

b)

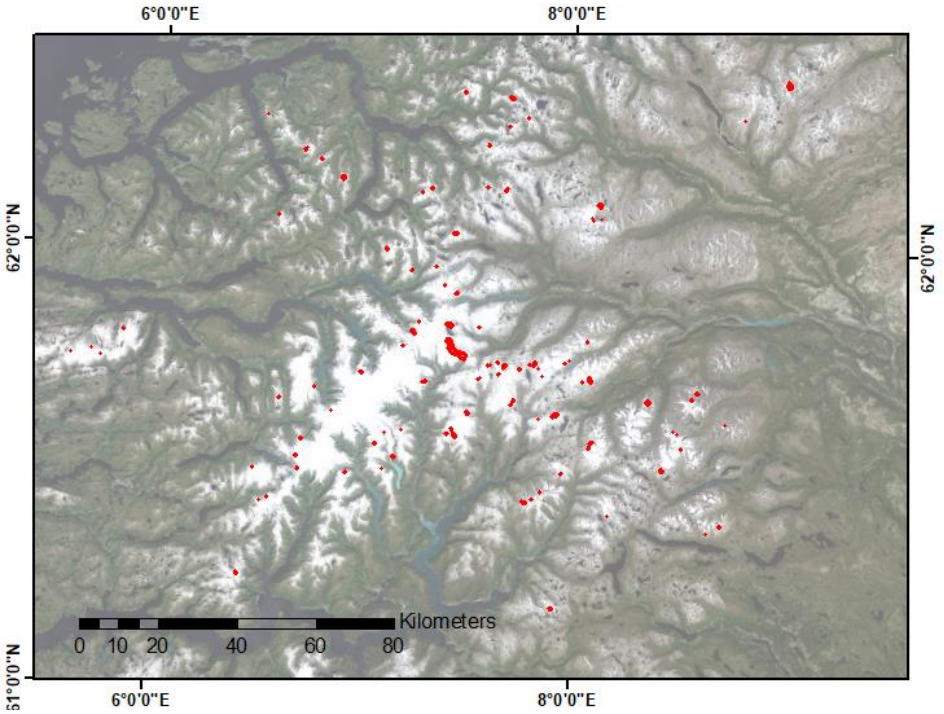
6°0'0"E
8°0'0"E
62°0'0"N
Kilometers
0 10 20 40 60 80

c)

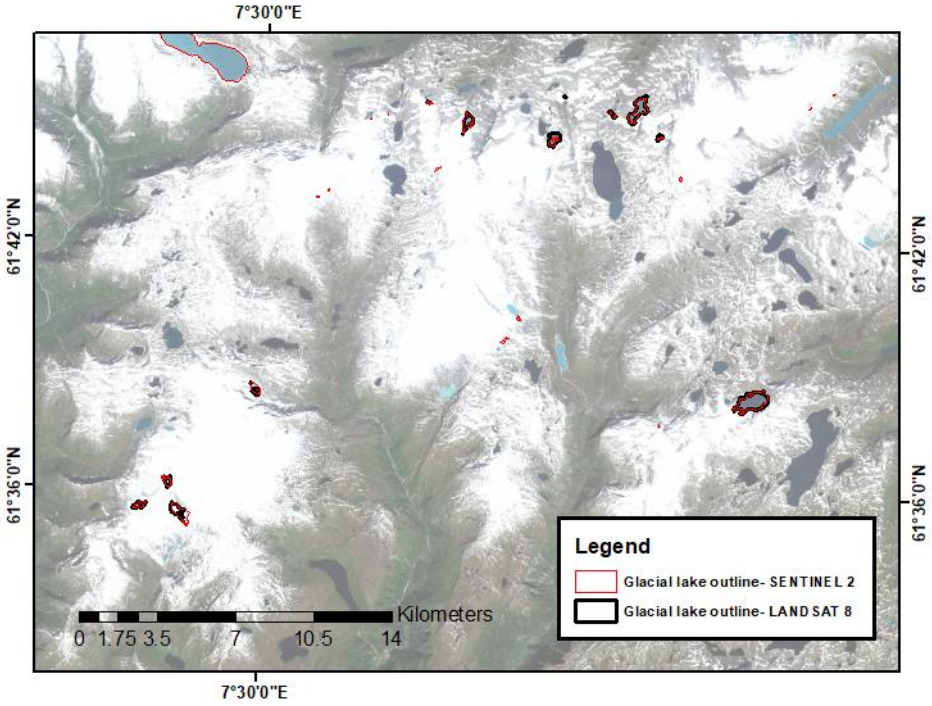

Figure 4.7 Comparison of glacial lakes outlined by using Landsat-8 and Sentinel-2 imagery in 2018-2019. a) Glacial lake outlines by using Landsat-8 images, b) Recognition of glacial lake outlines by using Sentinel-2 images in west and northwest of Jostedalsbreen as well as the eastern areas, c) Comparability of glacial lakes outlined in both sets of imagery.

In some areas, Landsat and Sentinel show good potential for a complementary use or even image fusion to enhance the glacial lake recognition skill of MLC. The areas for such complementary use are exemplified by figure 4.7, where glacial lakes west of Jostedalsbreen are visibly less recognized on Landsat-8 images (figure 4.7-a) as compared to Sentinel-2 images (figure 4.7-b). The latter enables a clearly enhanced recognition of glacial lakes in the areas both in the west and northwest of Jostedalsbreen. The 5-day revisit time of Sentinel-2 compared to the 16-day temporal resolution of Landsat-8 provided multiple images of some areas of interest to choose from. Therefore, the use of images with less cloud and snow/ice coverage contributed to the recognition of more glacial lake outlines in the western Jostedalsbreen area. However, MLC on Landsat-8 images depicted a visibly better performance in the eastern and north-eastern areas of Jostedalsbreen, heavily challenging the superiority of the Sentinel-2 images and their better temporal resolution.

On the one hand, Sentinel-2 lacks the thermal band that in MLC applications on Landsat-8 images featured as beneficial for lessening the adverse effects of shadows (see section 3.1.2). On the other hand, in areas where MLC recognized glacial lakes on both sets of images, the outlines were comparable (see figures 4.7-c and 3.15).

Glacial lakes dammed by the glacier Tystigbreen in the north of Jostedalsbreen can be mentioned as an instance for a mutually beneficial, complementary use of Sentinel and Landsat images to increase the classification precision (figure 4.8). The emergence and growth of four glacial lakes due to glacier retreat have caused recurrent jøkulhlaup events from two of them since 2014, albeit without adverse societal effects until now. The processes associated with these initial stages of the glacial lake cycle will likely increase in intensity, creating more dramatic impacts on the highly touristic areas downstream. It is therefore important to investigate the development and change of these lakes in the past and through the upcoming years. Although one of the four glacial lakes shown in figure 4.8 existed in the NVE's inventories for the periods of 1999-2006 and 2018-2019, MLC on the Landsat images missed it in both periods. However, it was recognized by the MLC application on the Sentinel-2 images, as visible in figure 4.8. On the contrary, Demmevatnet (figure 4.6) was only recognized by the application of MLC on Landsat images, while it was absent in the classification on Sentinel-2 images.

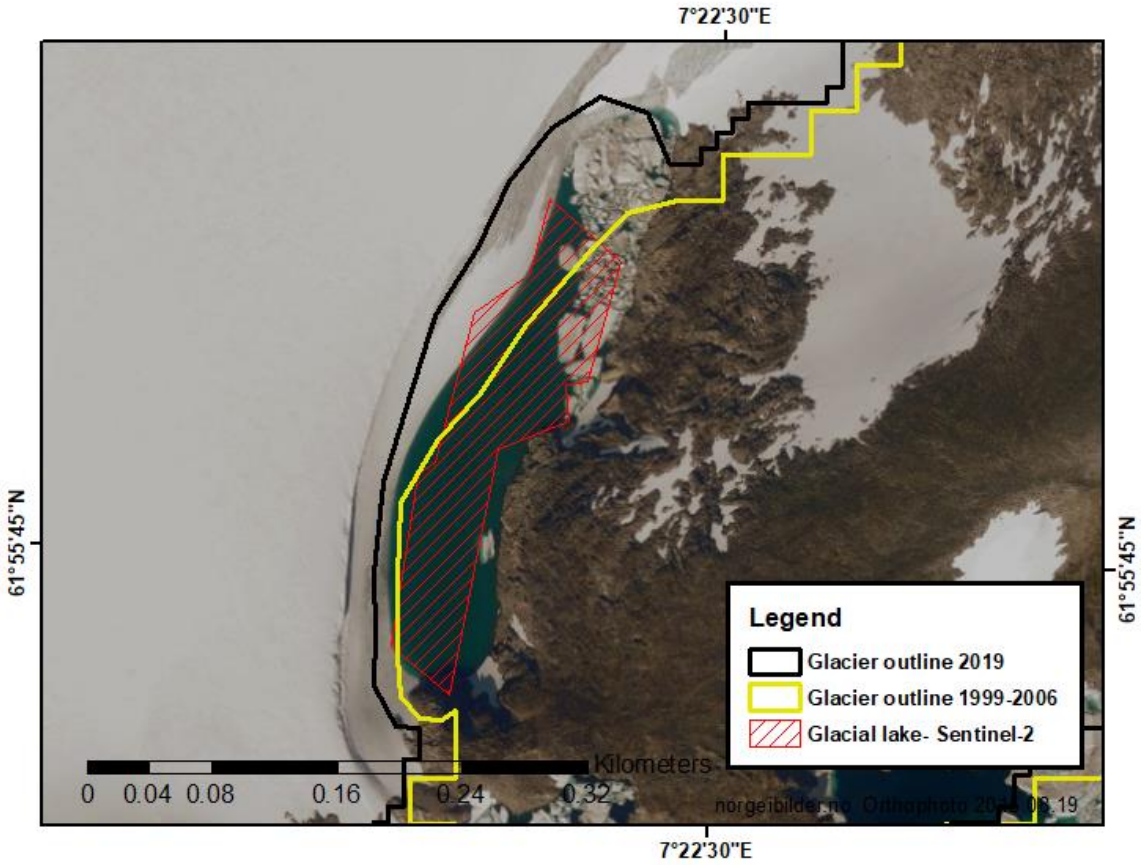

Figure 4.8 Recognition of glacial lake in Tystigbreen, north of Jostedalsbreen by application of MLC on Sentinel-2 images. Glacial lake growth due to glacier retreat.

In short, corresponding results from the classification on both Sentinel-2 and Landsat-8 have displayed the potential of the two sets of images to be used in an area of interest as complementary datasets. While Landsat imagery has the advantage of providing a long-term, uninterrupted record across nearly five decades, Sentinel increases the probability of capturing cloud, ice and snow free images due to its smaller revisit period. However, a 10-meter increase in spatial resolution in Sentinel-2 bands has not prompted a significant recognition potential improvement, contrary to my initial expectations.

4.2.2 Mitigation of shadow-related misclassifications: Thermal bands versus slope maps

Comparable lake outlines produced on Sentinel and Landsat images can serve as a proof that the application of Digital Elevation Maps (DEMs) and slope maps efficiently resolves the problem of shadow recognition, even without the involvement of thermal bands in the composite. Therefore, the absence of thermal bands in Sentinel-2 images cannot be acknowledged as a diminishing feature for the purpose of this study. This is an important observation that further reinforces conclusions of previous studies that slope maps can be used to eliminate one of the most persistent issues in classification of water bodies in high-relief environments – shadow-related misclassifications.

In this study, I have performed glacial lake classification on composites including bands blue, NIR, SWIR1 and SWIR2 from two satellite imagery sets (Sentinel and Landsat) and a thermal band from the Landsat imagery only. As described in chapter 3, an inclusion of the thermal band in classification on Landsat images has demonstrated a potential to partly resolve the problem of lake misclassification due to shadows. However, it did not fully eliminate this problem, as some shadowed pixels are still showing up as water bodies in the classified layers.

Bhardwij A. et al (2014) performed mapping of glacial facies using Landsat 8 OLI data combined with the thermal (TIRS) bands. Results of their work indicated an improvement when identifying crevasses located in the mountain shadows. They attributed this enhancement in the mapping quality to the inclusion of the thermal band. What differentiates their study from this work with respect to the elimination of the shadow effects is that they perform mapping based on band ratios instead of using composites, where a multiband image is generated from all the selected bands. Hence, the pixel values of all intersected bands in the composite are used as a reference for classification, while creating a signature file for the training samples representing each classified land type. This makes the classification more complex and due to Rayleigh scattering in the blue band, could cause a misclassification of some pixels as water bodies, while they are in fact corresponding to land located in the shadow (see section 3.1.2). In their study of

glacial lake outburst floods, Aggarwal *et al.*, 2016 mentioned the Rayleigh scattering effect as a restricting factor for outlining glacial lakes. Their use of the Normalized Difference Water Index (NDWI) method led to a severe misclassification of shadows as lakes and hence, an exaggeration of the lake areas. Figure 4.9 depicts the shadow effect on the MLC outcomes caused by reliefs surrounding the Storglomvatnet glacial lake in northern Norway. As opposed to other shadowed slopes that were correctly classified as land, the emphasized shadowed area next to the glacial lake in Figures 4.9-a, b was misclassified as a water body, and the lake was consequently extended further towards the glacier margin (Figure 4.9-c). Therefore, hinging on solely adding a thermal band to eliminate shadow-imposed misclassifications is unlikely to lead to an adequate improvement of the glacial lake recognition potential.

a) b) c)

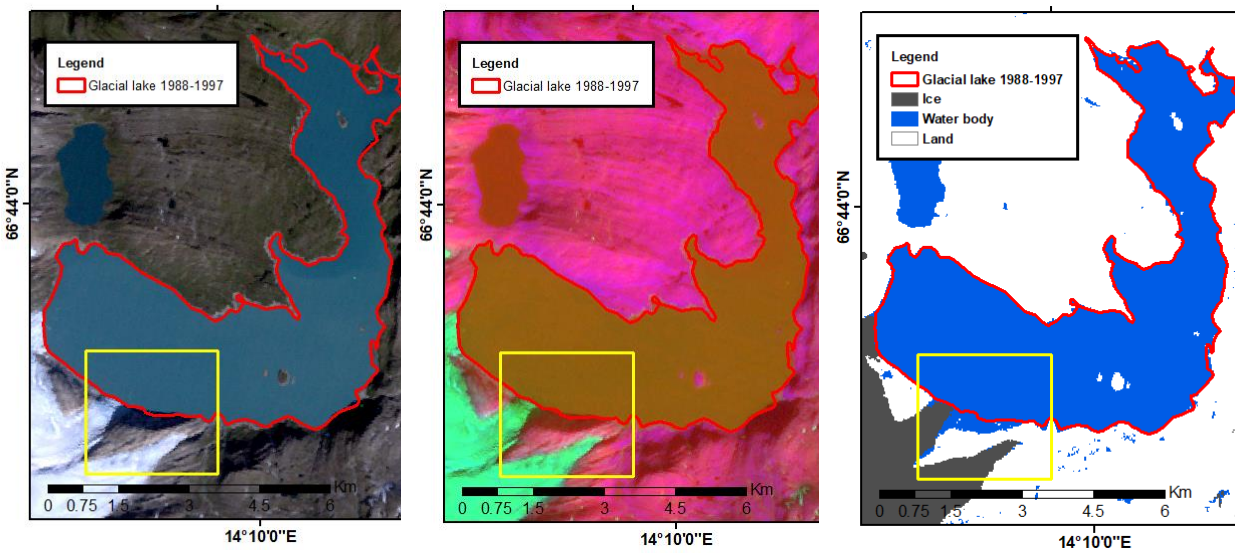

Figure 4.9 Shadow correction in Storglomvatnet glacial lake in northern Norway by using the thermal band in the Landsat-5 image from 1988.08.31. a) Natural colour image showing the area with cast shadow by the lake. b) False colour composite of the satellite image from bands blue, NIR, SWIR1, SWIR2 and thermal. c) Image produced by application of MLC and recognition of the shadow as water body class.

As an alternative solution, Li and Sheng, 2012 used a DEM to remove the shadow effects of mountains on glacial lake outlining in the Himalayas. In this study, I have followed their example by generating slope maps based on the DEMs as a supplementary method to adding a thermal band. An intersection between the slope maps and water bodies recognized by MLC and SVM allowed me to eliminate misclassified polygons (shadowed areas classified as water bodies) and thus resulted in a more precise delineation of glacial lakes. The final outline of the

glacial lake in figure 4.11 is a product of the image post-classification analysis where the misclassifications of the shadowed slopes were corrected using the generated slope maps.

In this study, I have tested both 10 and 50-meter DEMs to help separate the water bodies and misclassified shadows on slopes (see section 3.1.2). The DEM tiles covering whole Norway belong to several years, with the last tiles in the 10-m DEM updated in 2013 from available data at the time of production. In contrast, the dataset underpinning the 50-m DEM is much older and is based on the data collection completed in 2007 (Geonorge.no). My analyses revealed that some tiles in both datasets are older than their final collection dates, and there are many areas where the 10-m DEM has not been significantly modified compared to the 50-m DEM.

Glacial lakes located at the glacier termini or in the proximity of glaciers are often found in areas that were covered by glaciers during the time of the DEM data collection. Thus, the slope maps produced based on old DEMs are not a proper representation of the lakes themselves but often of the previously glaciated areas. Therefore, introducing a threshold for a separation of glacial lakes from shadowed slopes is a necessary step to eliminate the misclassified shadowed areas. Based on my analysis of the slope angles representative of glacial lake-covered areas, I have found that a threshold for surface slope angles as high as 14° is required to eliminate erroneously classified lake polygons. This threshold is higher than those suggested in other studies (Huggel *et al.*, 2002; Li & Sheng, 2012), clearly demonstrating the need for frequently updated DEMs that would allow for a more consistent editing of misclassifications across these rapidly changing environments.

4.3 On the superiority of the Support Vector Machine over Maximum Likelihood Classification

The second classification method, SVM, appeared to have superior recognition skills compared to MLC when it was tested on both Landsat-8 and Sentinel-2 images for a scene from 2018 (section 3.3). Indeed, the overall comparison of glacial lake outlines generated by MLC and SVM has revealed that the lake shapes from SVM are more comparable to the NVE's inventory. Given that both methods utilized the same training samples and a composite from the same satellite image, differences in their respective recognition skills have an origin in the methods' theoretical formulations leading to a cleaner division between classes. Jain *et al.*, 2015 tested SVM as a tool for automated recognition of glacial lakes and determination of their area in the Hindukush Himalaya and concluded that this method produced accurate results - the conclusion that is confirmed by this thesis.

In figure 4.9-a, the results from SVM and MLC for the Sveintjørni glacial lake showcase the relative strengths of SVM: first, it has recognized the complete lake rather than its part as opposed to MLC, and second, it displays a more precise outline of the glacial lake in comparison with MLC. Although MLC had recognized the second part of the lake as a water body in its initial classification (figure 4.9-b), it was not classified as a glacial lake due to the fact that MLC separated the two counterparts of the lake, with the second part falling out of the glacier buffer zone. In contrast, SVM recognized the glacial lake as one single segment (figure 4.9-c), which is due to a significantly more precise classification.

a)

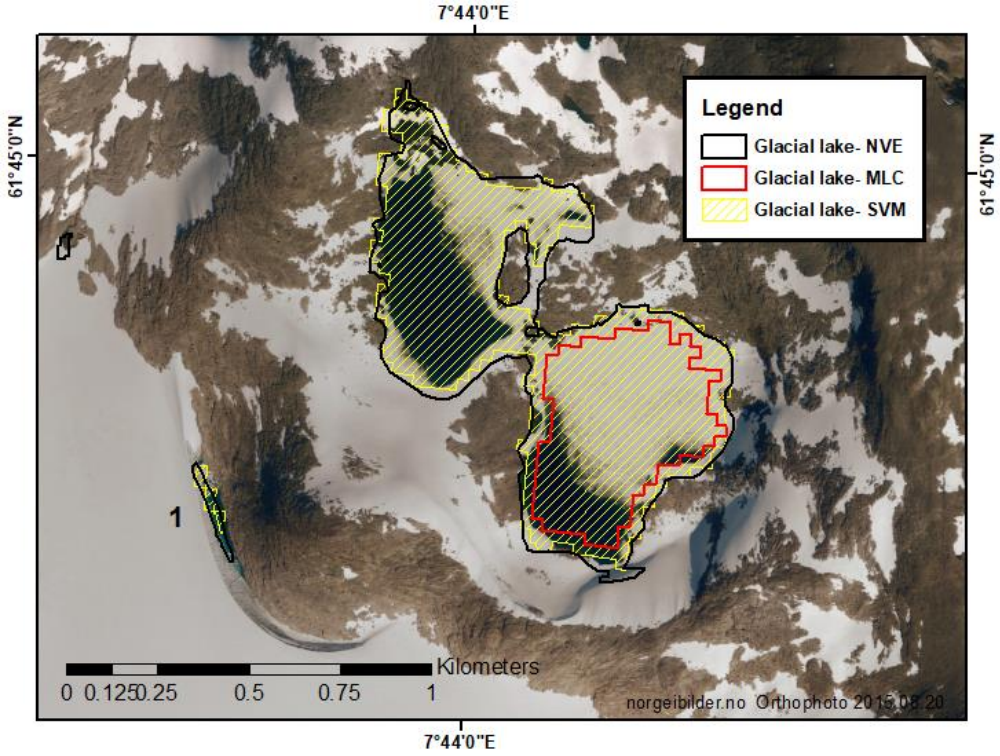

b)

c)

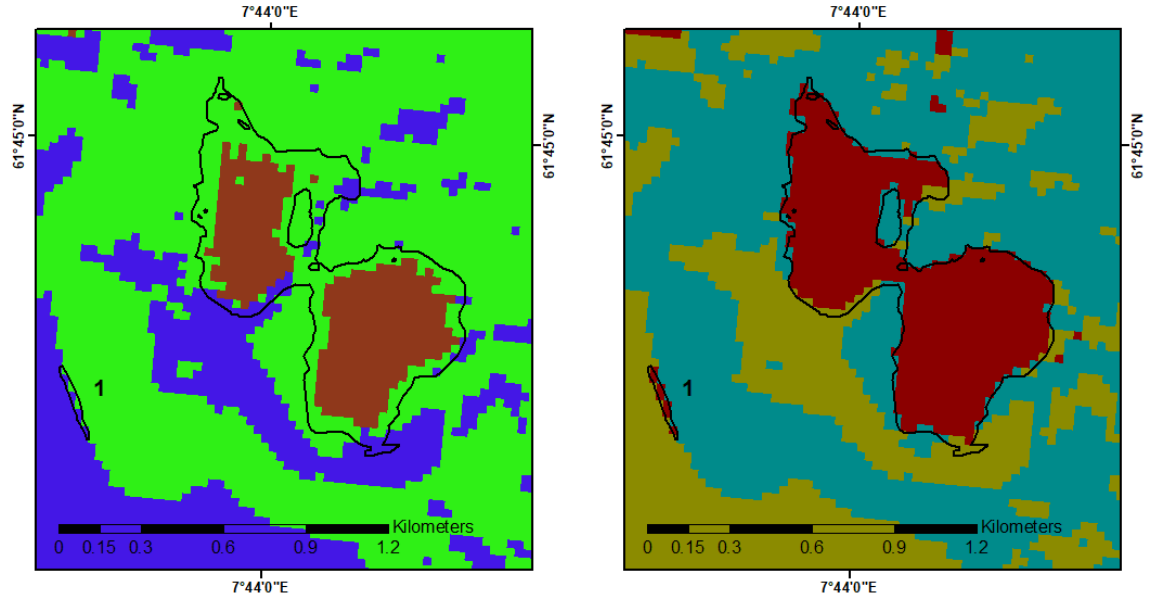

Figure 4.10 a) Glacial lake recognition in SVM, MLC and comparison with NVE's inventory of glacial lakes. Both methods were applied on a scene from Landsat-8, 2018.06.29. b) Classes of ice: blue, water body: brown, land: green, resulted from application of MLC. c) Classes of ice: dark yellow, water body: brown, land: blue, resulted from application of SVM.

In addition to Sveintjørni, figure 4.9 features glacial lake 1 located to the east of the glacier Fortundalsbreen in the Breheimen area. It is a small glacial lake with an area of 0.006 km^2 (T. Nagy & L. Andreassen, 2019), which was missing in the glacial lake dataset generated by MLC, while it was classified as a water body by SVM and then outlined as a glacial lake during the post-classification stage. This glacial lake is absent from the two older NVE's inventories and only exists in the most recent inventory for 2018-2019. While inspecting glacier outlines from older inventories, I noticed that the Fortundalsbreen glacier was covering the area that is currently occupied by this glacial lake. It has led me to the conclusion that the lake should be newly formed. In general, SVM has proven to be more precise in recognition of smaller lakes that makes it a better method for studying the formation and initial stages of development of new glacial lakes in proglacial environments.

Comparison of the glacial lake areas included in the NVE's inventory and those recognized by MLC and SVM clearly show that the SVM application has produced a closer match to the NVE's inventory for the scene in practice. This is a general observation illustrated in figure 3.18 that glacial lakes extracted by SVM display a better fit to the lake outlines from NVE's inventory. However, it is noteworthy to mention that the use of SVM as implemented in ENVI was associated with some limitations. Although the overall performance of SVM in glacial lake recognition tasks on a single image is deemed superior in comparison with MLC, SVM requires selection of separate sets of Regions of Interest (ROIs) in every single scene. This is a huge drawback when an automated classification is targeted over a large area as in this study, since it requires an enormous time investment, unlike the application of MLC in ArcGIS that uses the same signature file in all scenes of satellite images.

5 Conclusion

In this work, I have investigated the potential of applying machine learning algorithms in studies of glacial lakes and their life cycles in Norway. This research has been largely motivated by the frequent occurrence of glacier hazards associated with changes in glaciers and glacial lakes, in addition to their importance for national hydropower production. Outburst floods from ice-dammed glacial lakes (jøkulhlaups) are common in Norway, imposing a tangible threat to human lives and infrastructure. Identifying potential flood-generating glacial lakes can help mitigate their societal consequences and be beneficial for powerplant infrastructures.

The Norwegian water resources and energy directorate (NVE) administers Norway's water resources and power supplies in addition to managing glaciological investigations. To date, glacier and glacial lake inventories in Norway have been based on manual digitization or semiautomatic approaches. In terms of time efficiency, such approaches are not ideal since Norway is a large country with a high concentration of glaciers and glacial lake systems. To enable a more automated and consistent mapping of these environments, I have tested the applicability of classification methods based on supervised machine learning algorithms for the tasks involving mapping of glacial lake changes through time. The results demonstrate that automated classification on both Landsat and Sentinel satellite images can identify glacial lakes in the beginning stages of their formation, follow their evolution through years and even decades and occasionally capture the aftermath of jøkulhlaup events. These findings have been independently confirmed using two classification methods – Maximum Likelihood Classification (MLC) and Support Vector Machine (SVM) – and on satellite images with different spatial and temporal resolution – Landsat series and Sentinel-2.

The performance of MLC has been comprehensively evaluated during three time periods covered by the Landsat images (1988-1997, 1998-2006 and 2018-2019) and NVE's inventories. In addition, glacial lake recognition skills of both MLC and SVM have been compared and contrasted with respect to their relative performance on both Sentinel and Landsat images for the most recent period (2018-2019). Through this process, I have observed that achieving precise

glacial lake outlines is dependent on a variety of factors related to the specifics of each classification method and satellite dataset in use.

One of the most crucial factors to consider in supervised classifications is the selection of training samples. In this study, their selection has been performed for three classes - ice, water bodies and land, but the final focus of classification has been on the water body class. This process has revealed that training samples cannot be transferred between scenes from different days and especially seasons without undermining the classification outcomes. However, such transfer is possible between the two classification methods, MLC and SVM, used on the same scene.

Furthermore, the abundance of satellite images with heavy snow/ice and cloud coverage, which is typical for Norway, and the lack of consistent glacier inventories introduce significant limitations on how detailed time-evolved studies of glacial lakes can be and how many historical periods can be targeted by such studies. In those cases where glacial lakes in the satellite images are covered by snow/ice, or a glacier outline is missing for the period of study, it is neither possible to identify glacial lakes (or at least some of their counterparts) nor to follow their evolution through time. However, once high-quality images and glacier outlines are provided, classification methods have proven to be reliable for tracking glacial lake changes through time.

Applying atmospheric corrections on satellite images is a common pre-processing step preceding classification. However, my analyses have shown that such corrections lead to a great number of misclassifications due to distortion of the original images by no-pixel values that are recognized as water bodies. I conclude that such corrections are unnecessary and even harmful in the glacial lake classification studies. Due to different spectral specifications of the three defined classes (ice, water bodies, land), classification on uncorrected images has produced incomparably better results.

Finally, shadow-related misclassifications are among the most common limitations in glacial lake mapping, especially in high mountain areas where glacial lakes can be partially or completely located in shadow. To overcome this problem, I have utilized Digital Elevation Models (DEMs) to create slope maps. Based on a joint analysis of slope maps and glacial lake outlines from inventories, I have identified a threshold of 14° for surface slope angles that separates lakes from shadowed slopes misclassified as water bodies. Such a high threshold for a

lake-shadowed slope cutoff is explained by the unavailability of DEMs aligned with the periods of study. Nevertheless, shadow corrections resulted in an acceptable match between classified glacial lakes and their outlines from existing NVE's inventories for three historical periods covered in this thesis.

Areas and time periods for which it was possible to mitigate the unfavourable dataset-related factors described above provided deep insights into glacial lake changes through time. For example, it became possible to identify the impacts of glacier retreat on the growth and explanation of glacial lakes throughout the last three decades, both in the north and south of Norway. In the case of regulated glacial lakes used as reservoirs for hydropower production, it was even possible to observe the impacts of the established dams on the growing lake levels. This analysis has also identified some of the newly developing glacial lakes and shed light on the aftermath of a GLOF event that occurred in southern Norway and was captured by satellites. Although the higher spatial and temporal resolution of Sentinel-2 images should make them superior to the Landsat series, the absence of thermal bands has been regarded as a shortcoming since the inclusion of a thermal band in Landsat composites was originally assessed as beneficial for shadow reduction. However, the results of MLC on both sets of imagery for the period of 2018-2019 has revealed that glacial lake outlines from Sentinel-2 were comparable to the ones obtained with Landsat images. Therefore, I conclude that higher resolution of Sentinel images does not enhance their ability to recognize glacial lakes compared to Landsat images, except for very small lakes. It can also be deduced that the lack of thermal bands in Sentinel is not necessarily a large shortcoming in applications presented in this thesis since the DEM-based corrections of shadows are deemed more efficient compared to thermal bands. Finally, a comparative analysis of classification outcomes on Sentinel-2 and Landsat-8 images has shown that they have a good potential to be used as complementary datasets, especially in studies of jøkulhlaup-prone areas, which can benefit from more frequent glacial lake outlines enabled by Sentinel. Its shorter revisit time allows for more detailed observations of glacial lake changes, potentially contributing to new records of unreported jøkulhlaup events to help monitor, prepare, and facilitate mitigation efforts in national and local development plans.

To have a broader view on the performance of supervised machine learning algorithms (as a class) in glacial lake classification tasks, I have compared MLC to another supervised classification method, SVM, on representative scenes from both Landsat-8 OLI and Sentinel-2. In both scenes, SVM has shown a better recognition potential than MLC, even though both methods presented an acceptable accuracy rate of over 90% for classification. However, an automatization of SVM over a larger area appears to be problematic, at least in the form it is currently implemented in ENVI. Unlike MLC that enables using a signature file from one scene on other scenes with similar spectral characteristics, in SVM, training samples (regions of interest) need to be selected in every individual scene, making it extremely time consuming. However, a more accurate lake detection by SVM can help resolve changes in existing glacial lakes in a greater detail, including jøkulhlaup-prone areas, and increase the probability of detecting the formation of new glacial lakes.

In conclusion, this study has shown that both classification methods – MLC and SVM - produce comparable and occasionally superior results when compared with manual and Normalized Difference Water Index (NDWI) methods for outlining glacial lakes. Although the classification results depend sensitively on a number of limiting factors associated with the quality of observations and method's supervised learning, the efficient application and relatively precise results of automated classification methods justify their future adaptation by large-scale studies of glacial lake evolution.

REFERENCE

Adler-Golden, S., Berk, A., Bernstein, L., Richtsmeier, S., Acharya, P., Matthew, M., Anderson, G., Allred, C., Jeong, L., & Chetwynd, J. (1998). *FLAASH, a MODTRAN4 atmospheric correction package for hyperspectral data retrievals and simulations.* Paper presented at the Summaries of the seventh JPL airborne earth science workshop.

Adler-Golden, S. M., Matthew, M. W., Bernstein, L. S., Levine, R. Y., Berk, A., Richtsmeier, S. C., Acharya, P. K., Anderson, G. P., Felde, J. W., & Gardner, J. (1999). *Atmospheric correction for shortwave spectral imagery based on MODTRAN4.* Paper presented at the Imaging Spectrometry V.

Aggarwal, A., Jain, S. K., Lohani, A. K., & Jain, N. (2016). Glacial lake outburst flood risk assessment using combined approaches of remote sensing, GIS and dam break modelling. *Geomatics, Natural Hazards and Risk, 7*(1), 18-36.

Allen, S., Frey, H., Huggel, C., Krautblatter, M., Haeberli, W., Chiarle, M., & Geertsema, M. (2018). *A Technical Guidance Document for the Assessment of Glacier and Permafrost Hazards in Mountain Regions.* Paper presented at the EGU General Assembly Conference Abstracts.

Andreassen, L., Moholdt, G., Kääb, A., Messerli, A., Nagy, T., & winsvold, S. H. (2021). *Monitoring glaciers in mainland Norway and Svalbard using Sentinel.* (NVE Rapport 3-2021). Retrieved from

Andreassen, L. M., Paul, F., & Hausberg, J. E. (2014). Norway. 427-437. doi:10.1007/978-3-540-79818-7_19

Andreassen, L. M., & Winsvold, S. (2013). Algorithm Theoretical Basis Document (ATBD) for the GAO and GLO products.

Andreassen, L. M., Winsvold, S. H., Paul, F., & Hausberg, J. E. (2012). *Inventory of Norwegian glaciers* (8241008260). Retrieved from

Andreassen, L. M., Winsvold, S. H., Paul, F., & Hausberg, J. E. (2012). *Inventory of Norwegian glaciers*: Norwegian Water Resources and Energy Directorate.

Andrefouet, S., Bindschadler, R., Brown de Colstoun, E., Choate, M., Chomentowski, W., Christopherson, J., Doorn, B., Hall, D., Holifield, C., & Howard, S. (2003). Preliminary Assessment of the Value of Landsat-7 ETM+ Data Following Scan Line Corrector Malfunction. *US Geological Survey, EROS Data Center: Sioux Falls, SD, USA*.

ArcGIS, E. ArcMap Spatial Analyst Toolbox (Version 10.3). Retrieved from https://desktop.arcgis.com/en/arcmap/10.3/tools/spatial-analyst-toolbox/how-maximum-likelihood-classification-works.htm

Asmaa Sadiq, A. J., Ghazali, S., & Loay Edwar, G. (2014). SURVEY ON GAP FILLING ALGORITHMS IN LANDSAT 7 ETM+ IMAGES. *Journal of Theoretical & Applied Information Technology, 63*(1).

Bajracharya, S., Maharjan, S., Shrestha, F., Sherpa, T., Wagle, N., & Shrestha, A. (2020). *Inventory of glacial lakes and identification of potentially dangerous glacial lakes in the Koshi, Gandaki, and Karnali River Basins of Nepal, the Tibet Autonomous Region of China* (929115699X). Retrieved from

Bajracharya, S. R., & Mool, P. (2017). Glaciers, glacial lakes and glacial lake outburst floods in the Mount Everest region, Nepal. *Annals of glaciology, 50*(53), 81-86. doi:10.3189/172756410790595895

Barandela, R., & Gasca, E. (2000). *Decontamination of Training Samples for Supervised Pattern Recognition Methods*, Berlin, Heidelberg.

Barbieux, K., Charitsi, A., & Merminod, B. (2018). Icy lakes extraction and water-ice classification using Landsat 8 OLI multispectral data. *International journal of remote sensing, 39*(11), 3646-3678. doi:10.1080/01431161.2018.1447165

Beniston, M., Farinotti, D., Stoffel, M., Andreassen, L. M., Coppola, E., Eckert, N., Fantini, A., Giacona, F., Hauck, C., & Huss, M. (2018). The European mountain cryosphere: a review of its current state, trends, and future challenges. *The Cryosphere, 12*(2), 759-794.

Benn, D. I., Warren, C. R., & Mottram, R. H. (2007). Calving processes and the dynamics of calving glaciers. *Earth-Science Reviews, 82*(3-4), 143-179.

Bhardwaj, A., Joshi, P. K., Snehmani, Sam, L., Singh, M. K., Singh, S., & Kumar, R. (2015). Applicability of Landsat 8 data for characterizing glacier facies and supraglacial debris. *International journal of applied earth observation and geoinformation, 38*, 51. doi:10.1016/j.jag.2014.12.011

Bhardwaj, A., Singh, M. K., Joshi, P. K., Snehmani, Singh, S., Sam, L., Gupta, R. D., & Kumar, R. (2015). A lake detection algorithm using Landsat 8 data: A comparative approach in glacial environment. *International journal of applied earth observation and geoinformation, 38*, 150. doi:10.1016/j.jag.2015.01.004

Bjornsson, H. (1992). Jokulhlaups in Iceland - Prediction, Characteristics and Simulation. *Annals of Glaciology, Vol 16, 1992, 16*, 95-106.

Bjornsson, H. (2003). Subglacial lakes and jokulhlaups in Iceland. *Global and Planetary Change, 35*(3-4), 255-271. doi:Pii S0921-8181(02)00130-3

Doi 10.1016/S0921-8181(02)00130-3

Bjornsson, H. (2009). Jokulhlaups in Iceland: sources, release and drainage. *Megaflooding on Earth and Mars. Cambridge University Press, Cambridge*, 50-64.

Björnsson, H. (1974). *Explanations of jökulhlaups from Grímsvötn, Vatnajökull, Iceland*.

Boloorani, A. D., Erasmi, S., & Kappas, M. (2008). Multi-source remotely sensed data combination: Projection transformation gap-fill procedure. *Sensors, 8*(7), 4429-4440.

Bolstad, P., & Lillesand, T. (1991). Rapid maximum likelihood classification. *Photogrammetric engineering and remote sensing, 57*(1), 67-74.

Cao, X., Liu, Z., & Li, W. (2016). Glacial lake mapping and analysis of the potentially dangerous glacial lakes before Nepal 4 25 Earthquake in 2015. *Journal of Glaciology and Geocryology, 38*(3), 573-583.

Carrivick, J. L., & Quincey, D. J. (2014). Progressive increase in number and volume of ice-marginal lakes on the western margin of the Greenland Ice Sheet. *Global and Planetary Change, 116*, 156-163. doi:10.1016/j.gloplacha.2014.02.009

Carrivick, J. L., & Tweed, F. S. (2016). A global assessment of the societal impacts of glacier outburst floods. *Global and Planetary Change, 144*, 1-16. doi:10.1016/j.gloplacha.2016.07.001

Cenderelli, D. A., & Wohl, E. E. (2003). Flow hydraulics and geomorphic effects of glacial-lake outburst floods in the Mount Everest region, Nepal. *Earth surface processes and landforms, 28*(4), 385-407. doi:10.1002/esp.448

Chavez, P. S. (1996). Image-based atmospheric corrections-revisited and improved. *Photogrammetric engineering and remote sensing, 62*(9), 1025-1035.

Chen, F., Zhao, X., Ye, H., & Karakehayov, Z. (2012). Making use of the Landsat 7 SLC-off ETM+ image through different recovering approaches. *Data Acquisition Applications*.

Cortes, C., & Vapnik, V. (1995). Support-vector networks. *Machine learning, 20*(3), 273-297.

Denton, G. H., Heusser, C. J., Lowel, T. V., Moreno, P. I., Andersen, B. G., Heusser, L. E., Schluhter, C., & Marchant, D. R. (1999). Interhemispheric Linkage of Paleoclimate During the Last Glaciation. *Geografiska annaler. Series A, Physical geography, 81*(2), 107-153. doi:10.1111/j.0435-3676.1999.00055.x

DiStasio Jr, R. J., & Resmini, R. G. (2010). *Atmospheric compensation of thermal infrared hyperspectral imagery with the emissive empirical line method and the in-scene atmospheric compensation*

algorithms: a comparison. Paper presented at the Algorithms and Technologies for Multispectral, Hyperspectral, and Ultraspectral Imagery XVI.
Emmer, A., Merkl, S., & Mergili, M. (2015). Spatiotemporal patterns of high-mountain lakes and related hazards in western Austria. *Geomorphology (Amsterdam, Netherlands), 246*, 602-616. doi:10.1016/j.geomorph.2015.06.032
Engeset, R. V., Schuler, T. V., & Jackson, M. (2005). Analysis of the first jökulhlaup at Blåmannsisen, northern Norway, and implications for future events. *Annals of glaciology, 42*, 35-41.
ESA. (2015). Sentinel-s User Handbook.
FLAASH, U. s. G. (2009). Atmospheric Correction Module: QUAC and Flaash User Guide v. 4.7. *ITT Visual Information Solutions Inc.: Boulder, CO, USA*.
Florinsky, I. (2011). *Digital Terrain Analysis in Soil Science and Geology*. San Diego: San Diego: Elsevier Science & Technology.
Gagliardini, O., Gillet-Chaulet, F., Durand, G., Vincent, C., & Duval, P. (2011). Estimating the risk of glacier cavity collapse during artificial drainage: The case of Tête Rousse Glacier. *Geophysical research letters, 38*(10), n/a. doi:10.1029/2011GL047536
García-Borroto, M., García-Borroto, M., Martínez-Trinidad, J. F., Martínez-Trinidad, J. F., Carrasco-Ochoa, J. A., & Carrasco-Ochoa, J. A. (2014). A survey of emerging patterns for supervised classification. *Artificial Intelligence Review, 42*(4), 705-721. doi:10.1007/s10462-012-9355-x
Geonorge.no. Kartkatalogen DTM 10 Retrieved October 2020, from Kartverket https://kartkatalog.geonorge.no/Metadata/dtm-10-terrengmodell-utm33/dddbb667-1303-4ac5-8640-7ec04c0e3918
Geonorge.no. Kartkatalogen DTM 50. Retrieved October 2020, from Kartverket https://kartkatalog.geonorge.no/metadata/dtm-50/e25d0104-0858-4d06-bba8-d154514c11d2
Geospatial, L. H. (2010). Help Articles. Retrieved from https://www.l3harrisgeospatial.com/Support/Self-Help-Tools/Help-Articles
Gerace, A., & Montanaro, M. (2017). Derivation and validation of the stray light correction algorithm for the thermal infrared sensor onboard Landsat 8. *Remote Sensing of Environment, 191*, 246-257. doi:10.1016/j.rse.2017.01.029
Goslee, S. C. (2011). Analyzing remote sensing data in R: the landsat package. *Journal of Statistical Software, 43*(4), 1-25.
Guo, Y., & Zeng, F. (2012). Atmospheric correction comparison of SPOT-5 image based on model FLAASH and model QUAC. *International Archives of the Photogrammetry, Remote Sensing and Spatial Information Sciences, 39*(7), 21-23.
Hans, K., Guy, S., Marcus, B., Martin, G., & Pradeep, M. (1984). Mapping of Mountain Hazards and Slope Stability. *Mountain research and development, 4*(3), 247-266. doi:10.2307/3673145
Hsu, C.-W., Chang, C.-C., & Lin, C.-J. (2010). A practical guide to support vector classification. Department of Computer Science, National Taiwan University. In: Taipei. Tech. Rep.
Huggel, C., Kääb, A., Haeberli, W., Teysseire, P., & Paul, F. (2002). Remote sensing based assessment of hazards from glacier lake outbursts: a case study in the Swiss Alps. *Canadian Geotechnical Journal, 39*(2), 316-330.
Jackson, M. (2018). Glacier Floods and Hydropower-curse or blessing? *EGUGA*, 18871.
Jackson, M., & Ragulina, G. (2014). Inventory of glacier-related hazardous events in Norway. *Norges vassdrags-og energidirektorat (NVE)/Norwegian Water Resources and Energy Directorate, Report, 83*, 213.
Jain, S. K., Sinha, R. K., Chaudhary, A., & Shukla, S. (2015). Expansion of a glacial lake, Tsho Chubda, Chamkhar Chu Basin, Hindukush Himalaya, Bhutan. *Natural Hazards, 75*(2), 1451-1464.

Jha, L. K., Jha, L. K., Khare, D., & Khare, D. (2017). Detection and delineation of glacial lakes and identification of potentially dangerous lakes of Dhauliganga basin in the Himalaya by remote sensing techniques. *Natural Hazards, 85*(1), 301-327. doi:10.1007/s11069-016-2565-9

Kaufman, Y. J., Wald, A. E., Remer, L. A., Bo-Cai, G., Rong-Rong, L., & Flynn, L. (1997). The MODIS 2.1-µm channel-correlation with visible reflectance for use in remote sensing of aerosol. *IEEE transactions on geoscience and remote sensing, 35*(5), 1286-1298. doi:10.1109/36.628795

Ke, Y., Im, J., Lee, J., Gong, H., & Ryu, Y. (2015). Characteristics of Landsat 8 OLI-derived NDVI by comparison with multiple satellite sensors and in-situ observations. *Remote Sensing of Environment, 164*, 298-313.

Kjøllmoen, B. e., Andreassen, L. M., Elvehøy, H., & Jackson, M. (2020). *Glaciological investigations in Norway 2019.* (NVE Rapport 34-2020). Retrieved from

König, M., Hieronymi, M., & Oppelt, N. (2019). Application of Sentinel-2 MSI in Arctic research: evaluating the performance of atmospheric correction approaches over Arctic sea ice. *Frontiers in Earth Science, 7*, 22.

Landsat 7, N. Science Data Users Handbook. In.

Li, J., & Sheng, Y. (2012). An automated scheme for glacial lake dynamics mapping using Landsat imagery and digital elevation models: A case study in the Himalayas. *International journal of remote sensing, 33*(16), 5194-5213.

Liestøl, O. (1956). Glacier dammed lakes in Norway.

Lillesand, T. M., R. W. Kiefer. (2000). *Remote sensing and image interpretation.* (4th ed.). New York: John Wiley and Sons.

Loyola, D. G., & Coldewey-Egbers, M. (2012). Multi-sensor data merging with stacked neural networks for the creation of satellite long-term climate data records. *EURASIP Journal on Advances in Signal Processing, 2012*(1), 1-10.

Mallet, C., & David, N. (2016). Digital terrain models derived from airborne lidar data. In *Optical Remote Sensing of Land Surface* (pp. 299-319): Elsevier.

Masek, J. G., Vermote, E. F., Saleous, N. E., Wolfe, R., Hall, F. G., Huemmrich, K. F., Gao, F., Kutler, J., & Lim, T.-K. (2006). A Landsat surface reflectance dataset for North America, 1990-2000. *IEEE Geoscience and Remote Sensing Letters, 3*(1), 68-72.

Mather, P. M., & Koch, M. (2011). *Computer processing of remotely-sensed images: an introduction*: John Wiley & Sons.

Matthew, M. W., Adler-Golden, S. M., Berk, A., Felde, G., Anderson, G. P., Gorodetzky, D., Paswaters, S., & Shippert, M. (2002). *Atmospheric correction of spectral imagery: evaluation of the FLAASH algorithm with AVIRIS data.* Paper presented at the Applied Imagery Pattern Recognition Workshop, 2002. Proceedings.

McFeeters, S. K. (1996). The use of the Normalized Difference Water Index (NDWI) in the delineation of open water features. *International journal of remote sensing, 17*(7), 1425-1432.

Mohri, M., Rostamizadeh, A., & Talwalkar, A. (2018). *Foundations of machine learning*: MIT press.

Mondal, A., Kundu, S., Chandniha, S. K., Shukla, R., & Mishra, P. (2012). Comparison of support vector machine and maximum likelihood classification technique using satellite imagery. *International Journal of Remote Sensing and GIS, 1*(2), 116-123.

Myung, I. J. (2003). Tutorial on maximum likelihood estimation. *Journal of mathematical psychology, 47*(1), 90-100. doi:10.1016/s0022-2496(02)00028-7

Nagy, T., & Andreassen, L. (2019). Glacier lake mapping with Sentinel-2 imagery in Norway. *NVE Rapport*, 40-2019.

Nagy, T., & Andreassen, L. M. (2019). *Glacier surface velocity mapping with Sentinel-2 imagery in Norway*. Retrieved from

NVE's GLOF database. (2021). Retrieved from http://glacier.nve.no/Glacier/viewer/GLOF/en/nve/GlacierFloods/2968

NVE. Norges Vassdrags- og energidirektorat. Retrieved from https://www.nve.no/

Østrem, G., Haakensen, N., & Melander, O. (1973). *Atlas over breer i Nord-Skandinavia*.

Østrem, G., & Ziegler, T. (1969). *Atlas over breer i Sør-Norge = Atlas of glaciers in South Norway* (Vol. nr 20). Oslo: Norges vassdrags- og elektrisitetsvesen. Hydrologisk avdeling.

Paul, F., Kääb, A., & Haeberli, W. (2007). Recent glacier changes in the Alps observed by satellite: Consequences for future monitoring strategies. *Global and Planetary Change, 56*(1), 111-122. doi:10.1016/j.gloplacha.2006.07.007

Paul, F., Rastner, P., Azzoni, R. S., Diolaiuti, G., Fugazza, D., Le Bris, R., Nemec, J., Rabatel, A., Ramusovic, M., & Schwaizer, G. (2020). Glacier shrinkage in the Alps continues unabated as revealed by a new glacier inventory from Sentinel-2. *Earth System Science Data, 12*(3), 1805-1821.

Paul, F., Winsvold, S. H., Kääb, A., Nagler, T., & Schwaizer, G. (2016). Glacier remote sensing using Sentinel-2. Part II: Mapping glacier extents and surface facies, and comparison to Landsat 8. *Remote Sensing, 8*(7), 575.

Pringle, M., Schmidt, M., & Muir, J. (2009). Geostatistical interpolation of SLC-off Landsat ETM+ images. *ISPRS journal of photogrammetry and remote sensing, 64*(6), 654-664.

Pu, Y., Nace, T., Meyers, P. A., Zhang, H., Wang, Y., Zhang, C. L., & Shao, X. (2013). Paleoclimate changes of the last 1000yr on the eastern Qinghai–Tibetan Plateau recorded by elemental, isotopic, and molecular organic matter proxies in sediment from glacial Lake Ximencuo. *Palaeogeography, palaeoclimatology, palaeoecology, 379-380*, 39-53. doi:10.1016/j.palaeo.2013.03.023

Rasmussen, K. (1987). Floyd F. Sabins: Remote sensing: principles and interpretation. 2. ed. *Geografisk Tidsskrift*.

Ray, T. W. (1994). A FAQ on vegetation in remote sensing. *California: Div. of Geological and Planetary Sciences California Institute of Technology*.

Richards, J. A., & Richards, J. (1999). *Remote sensing digital image analysis* (Vol. 3): Springer.

Robert, P. d. E., & Larry, W. T. (1987). Interpreting Meteorological Satellite Images Using a Color-Composite Technique. *Bulletin of the American Meteorological Society, 68*(7), 762-768. doi:10.1175/1520-0477(1987)068<0762:IMSIUA>2.0.CO

2

Sadler, R. (1891). ON THE FLOW OF WATER IN EARTHEN CHANNELS. (INCLUDING PLATE AT BACK OF VOLUME). *Minutes of proceedings of the Institution of Civil Engineers, 103*(1891), 273-277. doi:10.1680/imotp.1891.20563

Senese, A., Maragno, D., Fugazza, D., Soncini, A., D'Agata, C., Azzoni, R. S., Minora, U., Ul-Hassan, R., Vuillermoz, E., Asif Khan, M., Shafiq Rana, A., Rasul, G., Smiraglia, C., & Diolaiuti, G. A. (2018). Inventory of glaciers and glacial lakes of the Central Karakoram National Park (CKNP – Pakistan). *Journal of maps, 14*(2), 189-198. doi:10.1080/17445647.2018.1445561

Shlien, S., & Smith, A. (1975). A rapid method to generate spectral theme classification of Landsat imagery. *Remote Sensing of Environment, 4*, 67-77.

Smith, M. J., & Clark, C. D. (2005). Methods for the visualization of digital elevation models for landform mapping. *Earth surface processes and landforms, 30*(7), 885-900. doi:10.1002/esp.1210

Song, C., Huang, B., & Ke, L. (2014). Inter-annual changes of alpine inland lake water storage on the Tibetan Plateau: Detection and analysis by integrating satellite altimetry and optical imagery. *Hydrological processes, 28*(4), 2411-2418. doi:10.1002/hyp.9798

Song, C., Huang, B., Ke, L., & Richards, K. S. (2014). Remote sensing of alpine lake water environment changes on the Tibetan Plateau and surroundings: A review. *ISPRS journal of photogrammetry and remote sensing, 92*, 26-37. doi:10.1016/j.isprsjprs.2014.03.001

Sun, J., Yang, J., Zhang, C., Yun, W., & Qu, J. (2013). Automatic remotely sensed image classification in a grid environment based on the maximum likelihood method. *Mathematical and Computer Modelling, 58*(3-4), 573-581.

Truffer, M., & Motyka, R. J. (2016). Where glaciers meet water: Subaqueous melt and its relevance to glaciers in various settings. *Reviews of Geophysics, 54*(1), 220-239.

Tweed, F. S., & Carrivick, J. L. (2015). Deglaciation and proglacial lakes. *Geology today, 31*(3), 96-102. doi:10.1111/gto.12094

UNESCO. (1971). A Contribution to to the International Hydrological Decade. Scientific framework of world water balance*., 7*.

USGS. (2013). Landsat 8: U.S. Geological Survey Fact Sheet 2013. *U.S.Geological Survey*.

USGS, L. Landsat 7. Retrieved from https://www.usgs.gov/core-science-systems/nli/landsat/landsat-7?qt-science_support_page_related_con=0#qt-science_support_page_related_con

USGS.gov. Retrieved from https://www.usgs.gov

Vermote, E., Justice, C., Claverie, M., & Franch, B. (2016). Preliminary analysis of the performance of the Landsat 8/OLI land surface reflectance product. *Remote Sensing of Environment, 185*, 46-56.

Viani, C., Machguth, H., Huggel, C., Godio, A., Franco, D., Perotti, L., & Giardino, M. (2020). Potential future lakes from continued glacier shrinkage in the Aosta Valley Region (Western Alps, Italy). *Geomorphology (Amsterdam, Netherlands), 355*, 107068. doi:10.1016/j.geomorph.2020.107068

Wang, Q., Shi, W., Li, Z., & Atkinson, P. M. (2016). Fusion of Sentinel-2 images. *Remote Sensing of Environment, 187*, 241-252. doi:10.1016/j.rse.2016.10.030

Wang, X., Ding, Y., Liu, S., Jiang, L., Wu, K., Jiang, Z., & Guo, W. (2013). Changes of glacial lakes and implications in Tian Shan, central Asia, based on remote sensing data from 1990 to 2010. *Environmental research letters, 8*(4), 044052. doi:10.1088/1748-9326/8/4/044052

Winsvold, S. H., Andreassen, L. M., & Kienholz, C. (2014). Glacier area and length changes in Norway from repeat inventories. *The Cryosphere, 8*(5), 1885-1903.

Yao, X., Liu, S., Han, L., Sun, M., & Zhao, L. (2018). Definition and classification system of glacial lake for inventory and hazards study. *Journal of geographical sciences, 28*(2), 193-205. doi:10.1007/s11442-018-1467-z

Yin, G., Mariethoz, G., & McCabe, M. F. (2017). Gap-filling of landsat 7 imagery using the direct sampling method. *Remote Sensing, 9*(1), 12.

Young, S. J., Johnson, B. R., & Hackwell, J. A. (2002). An in-scene method for atmospheric compensation of thermal hyperspectral data. *Journal of Geophysical Research: Atmospheres, 107*(D24), ACH 14-11-ACH 14-20.

Zhang, G., Bolch, T., Allen, S., Linsbauer, A., Chen, W., & Wang, W. (2019). Glacial lake evolution and glacier–lake interactions in the Poiqu River basin, central Himalaya, 1964–2017. *Journal of glaciology, 65*(251), 347-365.

Zhang, G., Yao, T., Xie, H., Wang, W., & Yang, W. (2015). An inventory of glacial lakes in the Third Pole region and their changes in response to global warming. *Global and Planetary Change, 131*, 148-157. doi:10.1016/j.gloplacha.2015.05.013

Zhang, M.-m., Chen, F., & Tian, B.-s. (2018). An automated method for glacial lake mapping in High Mountain Asia using Landsat 8 imagery. *Journal of Mountain Science, 15*(1), 13-24.

Ghazal Moghaddam

Life cycles of glacial lakes in Norway

NTNU
Norwegian University of
Science and Technology